DURBAN UNIVERSITY OF TECHNOLOGY

INYUVESI YASETHEKWINI YEZOBUCHWEPHESHE

DEVELOPMENT OF ELECTROCHEMICAL SENSORS FOR THE DETECTION OF MYCOTOXINS IN FOOD MATRICES USING FUNCTIONALISED NANOCOMPOSITES

By

Lyndon Naidoo

(Reg. No: 21353659)

Submitted in fulfilment of the requirements of the degree of Doctor of Philosophy in Chemistry in the Faculty of Applied Sciences at the Durban University of Technology

November 2023

DECLARATION

I, **Lyndon Naidoo,** declare that the thesis submitted for the degree of Doctor of Philosophy in Chemistry (DPCMS1) at the Durban University of Technology is the result of my own investigation and has not already been accepted in substance for any degree, and is not being concurrently submitted for any other degree. All the work was done by the author.

Student Name: Mr L Naidoo

Signature: Date: 27 / 11 / 2023

Supervisor Name: Prof Krishna Bisetty

Signature: Date: 27 / 11 / 2023

Co-Supervisor Name: Dr Florian Meier

Signature: Date: 27 / 11 / 2023

Co-Supervisor Name: Dr Gloria Ebube Uwaya

Signature: Date: 27 / 11 / 2023

ACKNOWLEDGEMENTS

It is by no means possible that I would have made it this far without the following set of inspirational people in my life. However, I would first like to thank God for guiding and helping me realize my dreams, and placing me in a position to work towards success from this moment and beyond.

I would like to start by thanking my supervisors, Prof Krishna Bisetty, Dr Florian Meier and Dr Gloria Uwaya for shepherding me through the trials and tribulations of research and academia. Their continuous input and guidance have proven invaluable since day one.

I would also like to extend my gratitude to my CMBAC (Computational Modelling and Bio-Analytical Chemistry) research group members, namely Phathisanani Hloma, Matshidiso Lephalala, Khethiwe Mthiyane and Calvin Harilal, for the countless moments of support and encouragement. Special mentions go out to Mrs NM Xhakaza, Ms N P Cele and Mrs D Naicker for their unwavering assistance in the lab.

My gratitude also extends to the number of special international experts that have contributed to the project, namely Mr Roland Drexel, Mr Achim Schmottlach, Mr Tys van der Merwe and Prof Albena Lederer. I am truly grateful for their exciting insights and influence on my work.

Acknowledgements also go out to the National Research Foundation (NRF) of South Africa, Durban University of Technology, Postnova Analytics and the Centre for High Performance Computing (an initiative supported by the Department of Science and Technology in South Africa) for access to cutting-edge resources and providing financial support.

Finally, I would like to thank my family and friends who have persisted in sticking by my side throughout this journey. It would not have been possible without you all.

ABSTRACT

The analysis of pathogens in foods is of critical importance to ensure consumer safety and quality assurance, as contaminants pose serious risks to public health. Mycotoxins are naturally occurring carcinogenic toxins that arise from specific strains of fungi as they contaminate food. They are found in a wide variety of grains, cereals, and dairy products, causing cancer in both humans and animals. Thus, there is a growing demand for simple, sensitive and inexpensive sensors for mycotoxin detection in lieu of conventionally employed large-scale instrumentation. In this study, the development of electrochemical sensors for the detection of aflatoxin B1 (AFB1), zearalenone (ZEN) and ochratoxin A (OTA) in foods was investigated and presented as three case studies, respectively.

In the first case study, an ultrasensitive aptasensor was developed for the indirect detection of AFB1 in the presence of a ferri/ferrocyanide ($[Fe(CN)_6]^{3-/4-}$) redox probe solution. The sensor was constructed by immobilizing an anti-AFB1 aptamer (Apt) to a carboxylated multiwalled carbon nanotube (cMWCNT) and iron oxide (Fe_3O_4) nanoparticle (NP) composite using a glassy carbon electrode (GCE). This resulted in the development of the GCE/cMWCNTs-Fe_3O_4 NP/Apt sensor. An electrochemical response was exhibited from AFB1 applying cyclic voltammetry (CV), electrochemical impedance spectroscopy (EIS), and differential pulse voltammetry (DPV), respectively, utilizing a $[Fe(CN)_6]^{3-/4-}$ redox probe prepared in phosphate-buffered saline (PBS) solution with reference to the Ag/AgCl reference electrode under optimized conditions. DPV findings reported very low limits of detection (LOD) and quantification (LOQ) of 0.43 fg mL^{-1} and 1.44 fg mL^{-1} respectively in comparison to current literature, over a calibration range of 0.50 fg mL^{-1} to 5.00 fg mL^{-1}. For real sample analysis, excellent spike recoveries from 95% to 105% were obtained for corn and rice flour. Density functional theory (DFT) was used to propose a reaction scheme by ascertaining the electronic properties of the redox-active functional groups of AFB1. This supported the experimental anodic response findings of DPV.

The second case study focused on how PEGylated Fe_3O_4 NPs and cMWCNTs fabricated on a GCE could be used for the design of an electrochemical sensor for ZEN analysis. The qualitative and quantitative analyses of ZEN were completed using CV, EIS and DPV, respectively, under optimized conditions in a sodium phosphate buffer solution. The developed sensor reported significantly low LODs and LOQs of 0.34 fg mL^{-1} and 1.12 fg mL^{-1}

respectively, over a calibration range of 1.00 fg mL^{-1} to 10.00 fg mL^{-1} by DPV. Excellent spike recoveries ranging from 92% to 106% were obtained for rice and corn flour. The Monte Carlo (MC) adsorption simulation studies predicted the strong interaction of ZEN with the constructed sensor.

In the final case study, an OTA electrochemical sensor was designed using a nickel metal-organic framework (Ni-MOF) and carboxylated reduced graphene oxide (cRGO) on a GCE. The detection of OTA was achieved under optimized conditions in PBS solution with the developed GCE/Ni-MOF/cRGO electrode, employing CV, EIS and DPV as electrochemical tools. Applying DPV, the sensor reported very low LODs and LOQs of 3.29 fg mL^{-1} and 10.97 fg mL^{-1} respectively, over a calibration range of 10.00 fg mL^{-1} to 90.00 fg mL^{-1}. Regarding real sample analysis, excellent spike recoveries from 95% to 105% were obtained for corn and rice flour. Molecular dynamics (MD) studies predicted that the Ni-MOF exhibited a strong electrostatic interaction with the OTA analyte, in agreement with the experimental findings.

The synthesized nanomaterials (cMWCNTs-Fe_3O_4 NP, PEG-Fe_3O_4 NPs/cMWCNTs, and Ni-MOF/cRGO) utilized in this study were characterized by an array of techniques, including single particle inductively coupled plasma-mass spectrometry (spICP-MS), transmission electron microscopy (TEM), X-ray diffraction (XRD), energy-dispersive X-ray spectroscopy (EDS), scanning electron microscopy (SEM), multidetector asymmetrical flow field-flow fractionation (AF4), and Fourier transform infrared spectroscopy (FTIR).

Finally, computational modelling studies were undertaken to establish a synergy with the experimental approaches employed in each case study. These methodologies included DFT, docking studies, MC adsorption and MD simulations, which were aimed at predicting and assessing the atomic and molecular interactions between the mycotoxins and their respective electrode systems.

Keywords: Aflatoxin B1, zearalenone, ochratoxin A, cyclic voltammetry, electrochemical impedance spectroscopy, differential pulse voltammetry, density functional theory, docking studies, Monte Carlo adsorption, molecular dynamics

LIST OF PUBLICATIONS

Naidoo, L., Uwaya, G. E., Meier, F. and Bisetty, K. 2023. A novel MB-tagged aptasensor for Aflatoxin B1 detection in food using Fe_3O_4 nanoparticles substantiated with *in silico* modelling. *Biosensors and Bioelectronics: X*, 15: 100416-100443. (https://doi.org/10.1016/j.biosx.2023.100416)

Naidoo, L., Uwaya, G. E., Meier, F. and Bisetty, K. 2023. A novel electrochemical sensor for the detection of zearalenone in food matrices using PEGylated Fe_3O_4 nanoparticles supported by *in-silico* and multidetector AF4. *Journal of Electroanalytical Chemistry*, 935: 117363-117372. (https://doi.org/10.1016/j.jelechem.2023.117363)

LIST OF CONFERENCE OUTPUTS

Oral Presentation

Lyndon Naidoo. “A novel electrochemical sensor for the detection of zearalenone in food matrices using PEGylated Fe_3O_4 nanoparticles supported by multidetector AF4 and in-silico studies”. 34th International Symposium on Polymer Analysis and Characterization held at Wallenberg Centre @ STIAS, Stellenbosch, South Africa. 24th to 26th April 2023.

Poster Presentation

Lyndon Naidoo. “A novel electrochemical sensor for the detection of zearalenone in food matrices using PEGylated Fe_3O_4 nanoparticles supported by multidetector AF4 and in-silico studies”. 34th International Symposium on Polymer Analysis and Characterization held at Wallenberg Centre @ STIAS, Stellenbosch, South Africa. 24th to 26th April 2023.

TABLE OF CONTENTS

DECLARATION ..... **i**

ACKNOWLEDGEMENTS ..... **ii**

ABSTRACT ..... **iii**

LIST OF PUBLICATIONS ..... **v**

LIST OF CONFERENCE OUTPUTS ..... **vi**

TABLE OF CONTENTS ..... **vii**

LIST OF FIGURES ..... **xiii**

LIST OF TABLES ..... **xviii**

LIST OF ACRONYMS AND SYMBOLS ..... **xix**

CHAPTER 1 - INTRODUCTION **1**

1.1) Background and problem statement 1

1.2) Aim and objectives 3

1.3) Thesis outline 4

CHAPTER 2 - LITERATURE REVIEW **6**

2.1) Mycotoxins in foods 6

2.2) Mycotoxin detection strategies 6

2.2.1) Chromatography 6

2.2.2) Enzyme-linked immunosorbent assay 7

2.2.3) Electrochemical sensors 7

2.3) Aflatoxin B1 8

2.4) Zearalenone 10

2.5) Ochratoxin A 12

2.6) Electrochemical methods 14

2.6.1) CV 15

2.6.2) EIS 17

2.6.3) DPV 18

2.7) Nanomaterials 19

2.7.1) Magnetic nanoparticles 20

2.7.2) Metal-organic frameworks 20

2.7.3) Carbon-based nanomaterials 20

2.7.4) Synthesis of nanomaterials 21

2.8) Characterization methods 21

2.8.1) AF4 21

2.8.2) SpICP-MS 23

2.8.3) XRD 24

2.8.4) SEM, TEM and EDS 25

2.8.5) FTIR 26

2.9) Computational methods 26

2.9.1) DFT 26

2.9.2) Molecular docking 27

2.9.3) MC simulation 27

2.9.4) MD simulation 27

CHAPTER 3 – MATERIALS AND METHODS 28

3.1) Experimental methods 28

3.1.1) Chemicals and materials 28

3.1.2) Instrumentation 29

3.1.3) Synthesis of Fe_3O_4 NPs 30

3.1.4) PEGylation of Fe_3O_4 NPs 30

3.1.5) Synthesis of Ni-MOF 30

3.1.6) Preparation of working solutions 30

3.1.6.1) Preparation of phosphate-buffered saline solution 30

3.1.6.2) Preparation of sodium phosphate buffer solution 31

3.1.6.3) Preparation of $[Fe(CN)_6]^{-3/-4}$ redox probe solution 31

3.1.7) Preparation of aptamer binding buffer 31

3.1.8) Aptamer immobilization on modified electrode 31

3.1.9) Preparation of electrode and modification by nanocomposites 31

3.1.10) Electrochemical analyses 32

3.1.11) Preparation of real samples 33

3.2) Computational methods 33

3.2.1) DFT 33

3.2.2) Molecular docking 33

3.2.3) MC simulation 34

3.2.4) MD simulation 34

CHAPTER 4 – RESULTS AND DISCUSSION 35

4.1) Case Study I: A novel MB-tagged aptasensor for aflatoxin B1 detection in food using Fe_3O_4 NPs substantiated with *in-silico* modelling 35

4.1.1) Characterization 35

4.1.1.1) SpICP-MS 35

4.1.1.2) XRD 36

4.1.1.3) EDS and SEM 37

4.1.2) Electrochemical analyses 38

4.1.2.1) Electrochemical properties of bare and modified electrodes 38

4.1.2.2) Scan rate variation of developed aptasensor 40

4.1.2.3) Optimization of experimental conditions 41

4.1.2.4) Evaluation of AFB1 analytical performance of developed aptasensor 43

4.1.2.5) Real sample analysis 44

4.1.2.6) Reproducibility, repeatability, storage stability and interference studies ... 44

4.1.3) Computational analyses 45

4.1.3.1) DFT 45

4.1.3.2) Molecular docking 47

4.1.4) Conclusion 48

4.2) Case Study II – A novel electrochemical sensor for the detection of zearalenone in food matrices using PEGylated Fe_3O_4 NPs supported by multidetector AF4 and *in-silico* studies 49

4.2.1) Characterization 49

4.2.1.1) Multidetector AF4 49

4.2.1.2) FTIR 50

4.2.1.3) EDS and SEM 50

4.2.2) Electrochemical analyses 52

4.2.2.1) Electrode characterization using redox probe 52

4.2.2.2) Optimization of experimental conditions 55

4.2.2.3) Evaluation of electrode performance towards ZEN 57

4.2.2.4) Evaluation of ZEN analytical performance on developed electrode 59

4.2.2.5) Real sample analysis 60

4.2.2.6) Repeatability, reproducibility, storage stability and interference studies ... 60

4.2.3) Computational analyses 61

4.2.3.1) MC simulation 61

4.2.4) Conclusion 63

4.3) Case Study III – A nickel MOF-based electrochemical sensor for ochratoxin A detection in food supported by *in-silico* studies 64

4.3.1) Characterization 64

4.3.1.1) FTIR 64

4.3.1.2) EDS and SEM 65

4.3.2) Electrochemical analyses 67

4.3.2.1) Electrochemical properties of bare and modified electrodes 67

4.3.2.2) Optimization of experimental conditions 69

4.3.2.3) Evaluation of electrode performance towards OTA 70

4.3.2.4) Evaluation of OTA analytical performance on developed electrode 72

4.3.2.5) Real sample analysis 73

4.3.2.6) Reproducibility, repeatability, storage stability and interference studies ... 73

4.3.3) Computational analyses 74

4.3.3.1) MD simulation 74

4.4) Conclusion 76

CHAPTER 5 – SUMMARY, CONCLUSIONS AND FUTURE RECOMMENDATIONS 77

5.1) Summary 77

5.2) Conclusions 78

5.3) Future recommendations 78

REFERENCES 80

APPENDICES 108

LIST OF FIGURES

Figure 1.1. Schematic representation of aptasensor employed for AFB1 detection in this study. 4

Figure 1.2. Schematic representation for ZEN detection employed in this study. 5

Figure 1.3. Schematic representation of OTA sensing employed in this study. 5

Figure 2.1. A 3D representation of AFB1 computed at B3LYP/6-31G** level of theory. 8

Figure 2.2. A 3D representation of ZEN computed at B3LYP/6-31G** level of theory. 11

Figure 2.3. A 3D representation of OTA computed at B3LYP/6-31G** level of theory 13

Figure 2.4. Schematics of three-electrode system used in electrochemical measurements. 15

Figure 2.5. A typical cyclic voltammogram depicted in CV analysis. 16

Figure 2.6. (a) Randles equivalent circuit and **(b)** typical Nyquist EIS plot. 18

Figure 2.7. A typical differential pulse voltammogram depicted in DPV analysis. 19

Figure 2.8. Working principle of AF4 separation, adapted from Postnova Analytics GmbH, Germany (Postnova 2017). 23

Figure 2.9. Light scattering principle of MALS detector, adapted from Postnova Analytics GmbH, Germany (Postnova 2017). 23

Figure 4.1. (a) SpICP-MS PSD and **(b)** TEM image of synthesized Fe_3O_4 NPs. 36

Figure 4.2. (a) XRD **(b)** EDS and SEM **(c, d** and **e)** for Fe_3O_4 NP, cMWCNTs and cMWCNTs-Fe_3O_4 NP. 38

Figure 4.3. Overlay of layer-by-layer electrode characterization by **(a)** CV at 0.025 V s^{-1} and **(b)** EIS from 100 kHz to 0.1 Hz using 1 mM $[Fe(CN)_6]^{3-/4-}$ solution. Randles equivalent circuits of **(c)** GCE and GCE/Fe_3O_4 NP *[R([RW]Q)]* **(d)** GCE/cMWCNTs, GCE/cMWCNTs-Fe_3O_4 NP and GCE/cMWCNTs-Fe_3O_4 NP/Apt *[R(R[QC])]*. 40

Figure 4.4. (a) Cyclic voltammogram overlay **(b)** i_p vs $\upsilon 1/2$ **(c)** $log\ _{ip}$ vs $log\ \upsilon$ **(d)** E_p vs $log\ \upsilon$ of scan rate optimization (0.01 V s^{-1} to 0.10 V s^{-1}) of GCE/cMWCNTs-Fe_3O_4 NP/Apt electrode in 1 mM $[Fe(CN)_6]^{3-/4-}$ solution. 41

Figure 4.5. Cyclic voltammograms of concentration optimization (0.10 fg mL^{-1} to 0.10 ng mL^{-1}) of AFB1 using GCE/cMWCNTs-Fe_3O_4 NP/Apt electrode in 1 mM $[Fe(CN)_6]^{3-/4-}$ solution. 42

Figure 4.6. Line graphs of **(a)** deposition voltage optimization and **(b)** deposition time optimization for DPV of 0.10 fg mL^{-1} AFB1 using GCE/cMWCNTs-Fe_3O_4 NP/Apt electrode in 1 mM $[Fe(CN)_6]^{3-/4-}$ solution. 42

Figure 4.7. (a) DPVs (n = 3) of GCE/cMWCNTs-Fe_3O_4 NP/Apt electrode with increasing concentrations of AFB1 (0.50 fg mL^{-1} to 5.00 fg mL^{-1}) prepared in 1 mM $[Fe(CN)_6]^{3-/4-}$ solution and **(b)** calibration curve of corresponding oxidation peak currents plotted against AFB1 concentrations. 43

Figure 4.8. (a) Bar graph of reproducibility study **(n = 3)** for DPV of 0.10 fg mL^{-1} AFB1 prepared 1 mM $[Fe(CN)_6]^{3-/4-}$ solution with different **(1-5)** GCE/cMWCNTs-Fe_3O_4 NP/Apt electrodes **(b)** Bar graph of DPV interference study **(n = 3)** of AFB1 in the presence of ZEN and OTA of the same concentration (0.10 fg mL^{-1}). 45

Figure 4.9. HOMO-LUMO depictions of AFB1 in **(a)** acetonitrile and **(b)** gaseous media as determined using DFT (B3LYP/6-31G**). 46

Figure 4.10. Proposed redox reaction scheme of AFB1 in acetonitrile with aptamer for DPV sensing. 47

Figure 4.11. A 3D **(a)** and 2D **(b)** representation of the binding of AFB1-aptamer interactions. 48

Figure 4.12. AF4-MALS fractogram over MALS 90° for PEG-Fe_3O_4 NP suspension. The red dots display the calculated radius of gyration (r_g) distribution across the eluting peak. 50

Figure 4.13. (a) FTIR **(b)** EDS and SEM **(c, d** and **e)** for PEG-Fe_3O_4 NP, cMWCNTs and PEG-Fe_3O_4 NP/cMWCNTs.....51

Figure 4.14. Overlay of layer-by-layer electrode characterization by **(a)** CV and **(b)** EIS using 1 mM $[Fe(CN)_6]^{3-/4-}$ solution. Randles equivalent circuits of **(c)** GCE and GCE/PEG-Fe_3O_4 NP *[R([RW]Q)]* **(d)** GCE/cMWCNTs and GCE/PEG-Fe_3O_4 NP/cMWCNTs *[R(R[QC])]*.....54

Figure 4.15. (a) Cyclic voltammogram overlay and **(b)** i_p vs $\upsilon 1/2$ of scan rate optimization (0.01 V s^{-1} to 0.10 V s^{-1}) of GCE/PEG-Fe_3O_4 NP/cMWCNTs electrode using a 1 mM $[Fe(CN)_6]^{3-/4-}$ solution.....55

Figure 4.16. Cyclic voltammograms of **(a)** concentration optimization (0.50 ng mL^{-1} to 5.00 ng mL^{-1}) and **(b)** buffer optimization (0.50 ng mL^{-1}) of ZEN using GCE/PEG-Fe_3O_4 NP/cMWCNTs electrode.....56

Figure 4.17. Cyclic voltammogram of pH optimization of 0.50 ng mL^{-1} ZEN prepared in sodium phosphate buffer with GCE/PEG-Fe_3O_4 NP/cMWCNTs electrode. 56

Figure 4.18. Line graphs of **(a)** deposition voltage optimization and **(b)** deposition time optimization for DPV of 0.50 ng mL^{-1} ZEN prepared in sodium phosphate buffer with GCE/PEG-Fe_3O_4 NP/cMWCNTs electrode. 57

Figure 4.19. Overlay of **(a)** CV and **(b)** EIS for layer-by-layer electrode study of 0.50 ng mL^{-1} ZEN prepared in sodium phosphate buffer. Randles equivalent circuit of **(c)** GCE, GCE/PEG-Fe_3O_4 NP, GCE/cMWCNTs and GCE/PEG-Fe_3O_4 NP/cMWCNTs *[R(R[QC])]*. 58

Figure 4.20. (a) DPVs (n = 3) at GCE/PEG-Fe_3O_4 NP/cMWCNTs electrode with increasing concentrations of ZEN (1.00 fg mL^{-1} to 10.00 fg mL^{-1}) prepared in sodium phosphate buffer and **(b)** calibration curve of corresponding reduction peak currents plotted against ZEN concentrations.....59

Figure 4.21. (a) Bar graph of reproducibility study (n = 3) for DPV of 0.50 ng mL^{-1} ZEN prepared in sodium phosphate buffer with different **(1-5)** GCE/PEG-Fe_3O_4 NP/cMWCNTs

electrodes **(b)** Bar graph of DPV interference study (n = 3) of ZEN in the presence of OTA and AFB1 of the same concentration (0.50 ng mL^{-1}).....61

Figure 4.22. Monte Carlo simulation of ZEN (shown in yellow) interacting with GCE/PEG-Fe_3O_4 NP/cMWCNTs electrode scheme. 62

Figure 4.23. FTIR for Ni-MOF, cRGO and Ni-MOF/cRGO. 65

Figure 4.24. (a) EDS and SEM **(b, c** and **d)** for Ni-MOF, cRGO and Ni-MOF/cRGO. 66

Figure 4.25. Overlay of layer-by-layer electrode characterization by **(a)** CV and **(b)** EIS using 1 mM $[Fe(CN)_6]^{3-/4-}$ solution. Randles equivalent circuits of **(c)** GCE and GCE/Ni-MOF *[R([RW]Q)]* **(d)** GCE/cRGO and GCE/Ni-MOF/cRGO *[R(R[QC])]*. 68

Figure 4.26. (a) Cyclic voltammogram overlay and **(b)** i_p vs $\upsilon 1/2$ of scan rate optimization (0.01 V s^{-1} to 0.10 V s^{-1}) of GCE/Ni-MOF/cRGO electrode using 1 mM $[Fe(CN)_6]^{3-/4-}$ solution. 69

Figure 4.27. Cyclic voltammograms of **(a)** concentration optimization (10.00 fg mL^{-1} to 0.10 ng mL^{-1}) **(b)** pH optimization (pH 4-9, 10.00 fg mL^{-1}) of OTA prepared in PBS solution using GCE/Ni-MOF/cRGO electrode. 70

Figure 4.28. Line graphs of **(a)** deposition time optimization and **(b)** deposition voltage optimization for DPV of 10.00 fg mL^{-1} OTA prepared in PBS solution using GCE/Ni-MOF/cRGO electrode. 70

Figure 4.29. Overlay of **(a)** CV and **(b)** EIS for layer-by-layer electrode study of 10.00 fg mL^{-1} OTA prepared in PBS solution. Randles equivalent circuit of **(c)** GCE, GCE/Ni-MOF, GCE/cRGO and GCE/Ni-MOF/cRGO *[R([RW]Q)]*.....71

Figure 4.30. (a) DPVs (n = 3) at GCE/Ni-MOF/cRGO electrode with increasing concentrations of OTA (10.00 fg mL^{-1} to 90.00 fg mL^{-1}) prepared in PBS solution and **(b)** calibration curve of corresponding oxidation peak currents plotted against OTA concentrations.....72

Figure 4.31. (a) Bar graph of reproducibility study (n = 3) for DPV of 10.00 fg mL^{-1} OTA prepared in PBS solution with different **(1-5)** GCE/Ni-MOF/cRGO electrodes **(b)** Bar graph of DPV interference study (n = 3) of OTA in the presence of ZEN and AFB1 of the same concentration (10.00 fg mL^{-1} prepared in PBS). 74

Figure 4.32. MD simulation of 10 OTA molecules (shown in yellow) interacting with Ni-MOF. 75

Figure 4.33. Total energy distribution for MD simulation of Ni-MOF-OTA complex.....75

LIST OF TABLES

Table 2.1. Current electrochemical sensors for AFB1 detection in foods. 10

Table 2.2. Current electrochemical sensors for ZEN detection in foods. 12

Table 2.3. Current electrochemical sensors for OTA detection in foods. 14

Table 4.1. EIS equivalent circuit data of GCE/cMWCNTs-Fe_3O_4 NP/Apt electrode using 1 mM $[Fe(CN)_6]^{3-/4-}$ solution. 40

Table 4.2. Comparison of the analytical performance of developed sensor with other aptasensors for AFB1 detection. 44

Table 4.3. Recoveries of AFB1 in real samples using developed aptasensor (n = 3). 44

Table 4.4. EIS equivalent circuit data of GCE/PEG-Fe_3O_4 NP/cMWCNTs electrode using a 1 mM $[Fe(CN)_6]^{3-/4-}$ solution. 54

Table 4.5. EIS equivalent circuit data of GCE/PEG-Fe_3O_4 NP/cMWCNTs electrode using 0.50 ng mL^{-1} ZEN prepared in sodium phosphate buffer. 59

Table 4.6. Comparison of the analytical performance of developed sensor with other analytical techniques for ZEN detection. 60

Table 4.7. Recoveries of ZEN in real samples using modified electrode (n = 3). 60

Table 4.8. Energy distribution (kcal mol^{-1}) of ZEN on the layer-by-layer scheme of the GCE/PEG-Fe_3O_4 NP/cMWCNTs electrode. 63

Table 4.9. EIS equivalent circuit data of GCE/Ni-MOF/cRGO electrode using a 1 mM $[Fe(CN)_6]^{3-/4-}$ solution. 68

Table 4.10. EIS equivalent circuit data of GCE/Ni-MOF/cRGO electrode using 10.00 fg mL^{-1} OTA prepared in PBS solution. 72

Table 4.11. Comparison of the analytical performance of developed sensor with other analytical techniques for OTA detection. 73

Table 4.12. Recoveries of OTA in real samples using developed sensor (n = 3). 73

LIST OF ACRONYMS AND SYMBOLS

AL	Adsorption Locator
AF4	Asymmetrical Flow Field-Flow Fractionation
AFB1	Aflatoxin B1
B3LYP	Becke's three-parameter exchange functional combined with the Lee-Yang-Parr correlation functional
cMWCNTs	Carboxylated multiwalled carbon nanotubes
CPE	Constant phase element
cRGO	Carboxylated reduced graphene oxide
CV	Cyclic voltammetry
DFT	Density functional theory
DPV	Differential pulse voltammetry
DT	Deposition time
DV	Deposition voltage
EDS	Energy-Dispersive X-ray Spectroscopy
ELISA	Enzyme-linked immunosorbent assay
FTIR	Fourier Transform Infrared Spectroscopy
GCE	Glassy carbon electrode
GO	Graphene oxide
IARC	International Agency for Research and Cancer
ICP-MS	Inductively Coupled Plasma – Mass Spectrometry
LOD	Limit of detection
LOQ	Limit of quantification
MALS	Multi-Angle Light Scattering

MB	Methylene blue
MC	Monte Carlo
MD	Molecular Dynamics
MOF	Metal-organic framework
MS	Material Studio
MWCNTs	Multi-walled carbon nanotubes
NM	Nanomaterial
NP	Nanoparticle
OTA	Ochratoxin A
PEG	Poly(ethylene glycol)
PSD	Particle size distribution
SEM	Scanning Electron Microscopy
SpICP-MS	Single particle ICP-MS
TEM	Transmission Electron Microscopy
UFF	Universal Force Field
XRD	X-Ray Diffraction
ZEN	Zearalenone

CHAPTER 1 - INTRODUCTION

This chapter provides a background of the study regarding mycotoxin analysis. Correspondingly, the current analytical approaches regarding the detection of mycotoxins in foods are discussed. This is followed by the aim, objectives, and a brief outline of the thesis.

1.1) Background and problem statement

Aflatoxin B1 (AFB1), zearalenone (ZEN) and ochratoxin A (OTA) are mycotoxins widely found in maize, rice, wheat and other agricultural products (Giannioti *et al.* 2023). They are known to exhibit severe carcinogenic effects in both humans and animals (Oufensou *et al.* 2023). Consequently, several analytical techniques have been evaluated for mycotoxin quantification regarding food safety and quality control. Current methods include thin-layer chromatography (TLC) (Salisu *et al.* 2021), gas chromatography-mass spectrometry (GC-MS) (Na *et al.* 2022), high-performance liquid chromatography (HPLC) (Singh and Mehta 2020) and immunoassay analyses (Yadav *et al.* 2021). Although these techniques are very useful, each has notable drawbacks, such as being costly to operate, time-consuming, and requiring high-level expertise (Fan *et al.* 2023). Hence, the introduction of electrochemical sensors can be seen as a way to overcome these challenges.

The recent rise in the application of electrochemical sensors has attracted interest due to their advantages, such as simplicity, low cost, wide linear range, and good sensitivity and selectivity (Otero and Magner 2020). The two most common methods are cyclic voltammetry (CV) and differential pulse voltammetry (DPV). Based on a redox transformation, they measure how a target analyte and its recognition element react to a redox change (Cesewski and Johnson 2020). In addition, the frequent employment of aptamers and nanomaterials, including nanoparticles (NPs), polymers, metal-organic frameworks (MOFs), and carbon materials such as multiwalled carbon nanotubes (MWCNTs) and graphene oxide (GO), has gained momentum in recent years regarding pathogen and toxin analyses in sensor construction (Cheng *et al.* 2021). Consequently, these materials have been employed to modify working electrodes for signal amplification to improve the conductivity, catalytic response, and detection performance of electrochemical sensors (Yang *et al.* 2022; Rahimizadeh *et al.* 2023).

Aptamers are short, single-stranded DNA or RNA oligonucleotides that can form stable complexes with specific target molecules. They exhibit advantages such as having a wide target range (from metal ions to cells), low toxicity, simple modification and synthesis, and stability under diverse environmental conditions (Sun *et al.* 2023a). Magnetic Fe_3O_4 NPs have been known to play a key role in electrochemical sensor development due to their high surface area, superparamagnetic property, ease of preparation, high adsorption ability, biocompatibility, and high electrical conductivity (Socas-Rodríguez *et al.* 2020; Shalali, Cheraghi and Taher 2022). On the other hand, poly(ethylene glycol) (PEG) has been employed to successfully quell agglomeration states in Fe_3O_4 NPs as capping agents and promote biocompatibility for sensor applications (Sarkar *et al.* 2016; Vallabani and Singh 2018; Antarnusa *et al.* 2022). Further, the functionalization of MWCNTs using carboxyl groups is well-known to have properties that exhibit outstanding conductivity and enhanced electrode electrocatalytic activity (Sun *et al.* 2022a). This process also results in the cMWCNTs having improved solubility and dispersity as opposed to pristine MWCNTs, and coupled with the intercalation of NPs, further increases their applicability for use in electrochemical sensor development (Hloma, Uwaya and Bisetty 2022). Further, metal-organic frameworks (MOFs) have been utilized in sensor development owing to their unique properties such as high porosity, active functional sites, and attractive morphologies (Mohan *et al.* 2023). It has also been reported that the combination of MOFs with carbon-based materials, like GO, is likely to improve analyte sensitivity by enhancing electrical properties and thus facilitating good electron transfer (Mokhtar *et al.* 2022).

Finally, state-of-the-art *in-silico* techniques such as Monte Carlo (MC) adsorption, molecular docking, molecular dynamics (MD) and density functional theory (DFT) calculations have been employed for the exploration and validation of experimentally observed behaviour that may otherwise not be possible through traditional analytical techniques. Computer simulations allow for theoretical principles to propose areas of interest to which experimental techniques may be applied, including the potential to support sensing studies (Arodola *et al.* 2020; Lephalala *et al.* 2020; Naidoo *et al.* 2020; Naidoo *et al.* 2021; Hloma, Uwaya and Bisetty 2022).

This research was conducted as case studies to contribute to the development of electrochemical sensors for AFB1, ZEN and OTA, respectively.

1.2) Aim and objectives

Aim

To develop highly selective and sensitive electrochemical sensors for the detection of AFB1, ZEN and OTA in real food samples.

Objectives

- To synthesize Fe_3O_4 NPs, PEGylated Fe_3O_4 NPs and Ni-MOF, as well as construct their composites (cMWCNTs-Fe_3O_4 NP, PEG-Fe_3O_4 NP/cMWCNTs and Ni-MOF/cRGO) for mycotoxin sensor development.
- To perform characterization studies on the synthesized NPs, MOF and their developed composites using single particle inductively coupled plasma-mass spectrometry (spICP-MS), X-ray diffraction (XRD), energy-dispersive X-ray spectroscopy (EDS), scanning electron microscopy (SEM), multidetector asymmetrical flow field-flow fractionation (AF4), and Fourier transform infrared spectroscopy (FTIR).
- To develop an aptasensor for AFB1 detection by immobilizing the selective aptamer onto the surface of a glassy carbon electrode (GCE) modified with the developed cMWCNTs-Fe_3O_4 NP nanocomposite.
- To develop electrochemical sensors for ZEN and OTA detection by immobilizing PEG-Fe_3O_4 NP/cMWCNTs and Ni-MOF/cRGO nanocomposites onto GCE, respectively.
- To optimize and measure the performance of the designed sensors toward AFB1, ZEN and OTA detection, respectively, by performing standard (CV and electrochemical impedance spectroscopy (EIS)) and real sample analyses (DPV).
- To identify the redox reactive sites, predict adsorption phenomena, and assess the intermolecular interactions of the analytes with the fabricated electrode surfaces using computer experiments involving DFT, molecular docking, MC and MD simulations, respectively.

1.3) Thesis outline

This thesis is divided into five chapters. Following the introduction, further chapters are divided as follows:

Chapter 2 - Literature Review

The chapter describes the literature survey of the project regarding the ubiquity and toxicological concerns posed by the AFB1, ZEN and OTA mycotoxins, respectively. Also, the current analytical approaches to deal with mycotoxin detection are discussed.

Chapter 3 – Materials and Methods

This chapter entails a description of the materials and methods employed in both the experimental and computational studies of this work.

Chapter 4 – Results and Discussion

This chapter details the results and discussion of the work in a case-study format as follows:

- Case Study I – A novel MB-tagged aptasensor for aflatoxin B1 detection in food using Fe_3O_4 NPs substantiated with *in-silico* modelling (**Figure 1.1**)

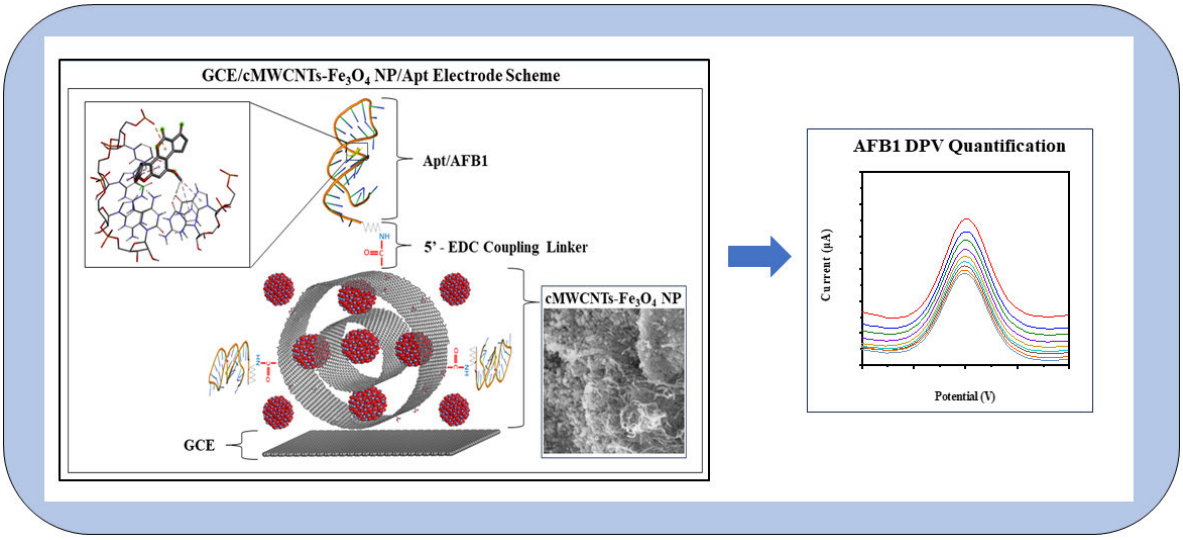

Figure 1.1. Schematic representation of aptasensor employed for AFB1 detection in this study.

- Case Study II – A novel electrochemical sensor for the detection of zearalenone in food matrices using PEGylated Fe_3O_4 NPs supported by multidetector AF4 and *in-silico* studies (**Figure 1.2**)

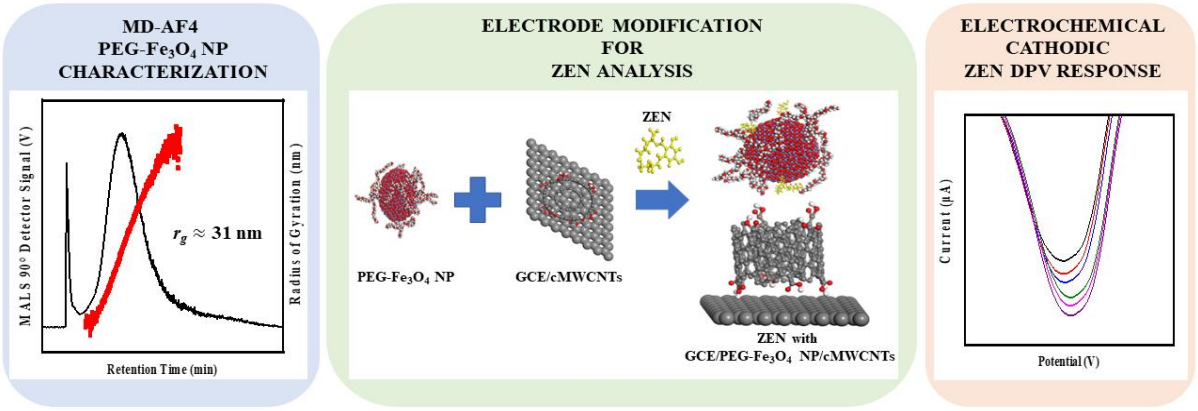

Figure 1.2. Schematic representation for ZEN detection employed in this study.

- Case Study III – A nickel MOF-based electrochemical sensor for ochratoxin A detection in food supported by *in-silico* studies (**Figure 1.3**)

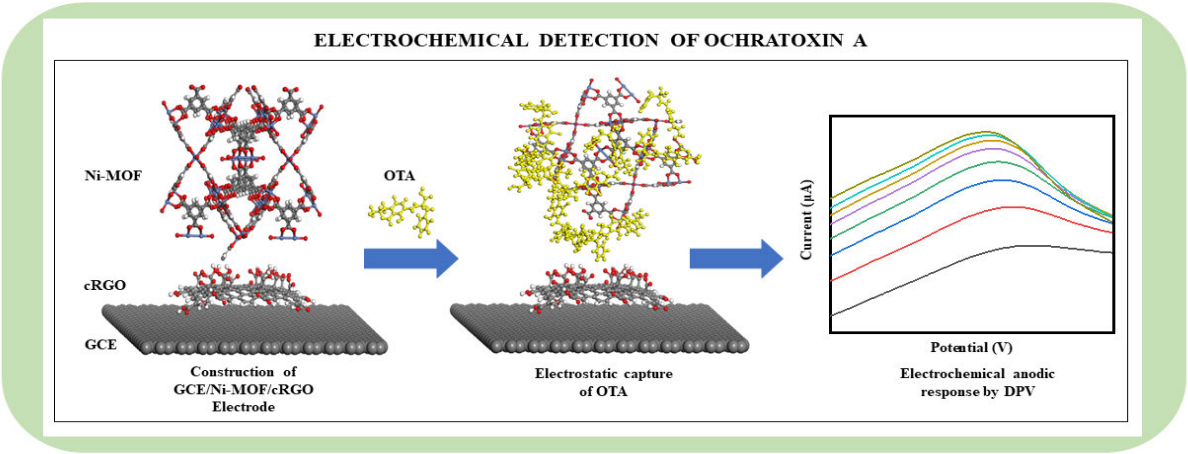

Figure 1.3. Schematic representation of OTA sensing employed in this study.

Chapter 5 – Summary, Conclusions and Recommendations

This chapter entails the summary, conclusions and future recommendations of this work.

References

A list of references cited throughout the thesis.

CHAPTER 2 - LITERATURE REVIEW

The purpose of this chapter is to provide an overview of the prevalence of AFB1, ZEN and OTA mycotoxins in foods. It is also discussed how they may impact the health of humans and animals. Finally, advances made regarding current analytical approaches suited to the analysis of the aforementioned mycotoxins are discussed.

2.1) Mycotoxins in foods

Mycotoxins are naturally occurring secondary metabolites produced by toxigenic microfungi, which include the *Aspergillus*, *Fusarium*, *Penicillium*, and *Stachybotrys* species (Malir *et al.* 2023). These fungi are known to grow in and contaminate various food sources such as bread, vegetables, cereals, nuts, fruits, and liqueur (Jafarzadeh *et al.* 2023). They possess thermal and chemical stability across various food processing stages, ranging from pre-harvest to storage (Hamad *et al.* 2023). An estimated US$932 million in worldwide annual financial losses in agricultural products have been reported due to mycotoxin exposure (Neuenfeldt *et al.* 2023). Mycotoxins afflict severe pathological disorders in human and animal health, exhibiting effects such as carcinogenicity, hepatotoxicity, neurotoxicity, nephrotoxicity, and immunotoxicity (El-Sayed *et al.* 2022). To date, over 400 types of mycotoxins have been identified, with aflatoxin B1, zearalenone, and ochratoxin A recognized as among the most common and potent affecting agriculture, economics and public health on a global scale (Yang *et al.* 2022). As per these concerns, several analytical approaches have been evaluated for the highly sensitive and selective detection of mycotoxins to monitor and ensure food quality and safety.

2.2) Mycotoxin detection strategies

2.2.1) Chromatography

Chromatography is a family of analytical techniques characterized by the separation of components carried by a mobile phase through a stationary phase for qualitative and quantitative analyses (Coskun 2016). Most methods employed for mycotoxin detection include chromatographic techniques such as thin-layer chromatography (Teixeira *et al.* 2011; Pradhan and Ananthanarayan 2020), high-performance liquid chromatography (Öncü Kaya *et al.* 2019; Saini and Abdel-Rehim 2020; Koch, Mauch and Riedel 2022), gas chromatography-mass spectrometry (Pack *et al.* 2020), and liquid chromatography-mass spectrometry (Lv *et al.* 2021). While these techniques are accurate, reproducible and sensitive, they have drawbacks

such as complicated sample preparation procedures, inhibition of on-site detection, and long analysis times (Harpaz *et al.* 2022).

2.2.2) Enzyme-linked immunosorbent assay

ELISA is a biochemical method used to screen and quantify analytes by enzymatic interactions of washed species for subsequent colorimetric measurements (Zhang and Vrient 2020). The technique boasts significant advantages over chromatographic methods, such as simpler sample preparation and requiring lower volumes (Maggira *et al.* 2022), and as such has been widely employed in mycotoxin analyses (Kononenko *et al.* 2022; Tian *et al.* 2022; Chavez *et al.* 2023; Feng *et al.* 2023; Yoshinari *et al.* 2023). Although ELISA is promising, it still holds considerable disadvantages, such as the requirement of highly skilled personnel, expensive equipment and differing measurement uncertainties (Rayappa *et al.* 2021).

Thus, recently, interest has surged towards the development of methodologies to address the limitations of these conventional techniques for the sensitive detection of mycotoxins.

2.2.3) Electrochemical sensors

An electrochemical sensor can be defined as a detection device that transduces electrochemical responses from an analyte into electrical signals for qualitative and quantitative analyses based on voltammetric, conductometric, potentiometric and impedance methods (Dhinakaran *et al.* 2020; Qian *et al.* 2021). At present, many varied types of sensors are applied for mycotoxin analysis, including electrochemical aptasensors, magnetic nanoparticle-based sensors and metal-organic framework-based sensors.

Electrochemical aptasensors employ aptamers, which are short, single-stranded DNA or RNA oligonucleotides that show specific binding affinities for targets such as amino acids, proteins, drugs and other molecules. They are viewed as more efficient alternatives to antibodies as they exhibit advantages such as superior shelf life, simple production and straightforward chemical modification protocols (Hasanzadeh *et al.* 2018; Odeh *et al.* 2020). Nanoparticles play critical roles in sensors regarding participation in detection reactions, catalysis, improved electron transfer, labelling and receiver stabilization (Huang, Zhu and Kianfar 2021). MOFs exhibit unique inherent properties such as good thermal stability, a large surface area, adjustable chemical functionalities and tuneable surface properties (Kajal *et al.* 2022). Polymers feature powerful characteristics for sensor design, such as strong adherence to electrode surfaces, the

ability to form stable physical and chemical coatings, and high electrical capacitance (Ramanavicius *et al.* 2022). Carbon-based materials have shown high potential due to their strong electrical conductivity, low cost and ability to act as excellent electrode-supporting platforms (Liu *et al.* 2022c).

Thus, these approaches can be investigated further regarding AFB1, ZEN and OTA, the focus of this work.

2.3) Aflatoxin B1

Aflatoxin B1 (**Figure 2.1**) is a secondary metabolite mycotoxin produced by the *Aspergillus flavus* and *Aspergillus parasiticus* fungi species widely found in agricultural products such as rice, maize, nuts, and wheat (Wang *et al.* 2022d). Its affinity towards humid environments and resistance against crop treatment, which result in widespread food contamination through worldwide distribution, raise concerns about animal and human exposure to AFB1 on a global scale (He *et al.* 2023). The conversion of AFB1 to its AFB1-exo isomer 8,9-epoxide metabolite, which occurs after ingestion in the liver of humans by cytochrome P450 enzymes, has been reported to induce DNA damage with genotoxic characteristics; the 8th carbon atom of the epoxide binds covalently with the 7th nitrogen atom of DNA guanine to form the toxic AFB1-N7-Gua adduct, exhibiting correlating mutagenesis with AFB1 exposure (Fan, Xie and Ma 2021). This consequently leads to severe health implications such as carcinogenicity and teratogenicity, and as such, AFB1 has been categorized as a group I carcinogen by the International Agency for Research and Cancer (Wu *et al.* 2022).

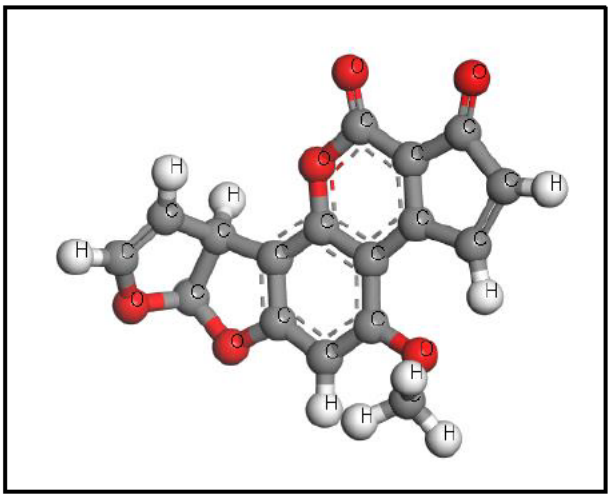

Figure 2.1. A 3D representation of AFB1 computed at B3LYP/6-31G** level of theory.

Current analytical techniques employed for AFB1 detection include thin-layer chromatography (Pradhan and Ananthanarayan 2020), high-performance liquid chromatography (Saini and Abdel-Rehim 2020), and immunochemical analyses (Yadav *et al.* 2021). Even though these techniques are very useful, electrochemical sensors have recently seen a rise in popularity due to their numerous benefits, including ease of use, low cost, fast response, high selectivity and sensitivity, portability, and the potential for on-site monitoring (Beitollahi *et al.* 2020) (**Table 2.1**). In addition, the use of aptamers has surged in various therapeutic, diagnostic, and analytical applications since they were first described in 1990 (Qian *et al.* 2022a). Electrochemical aptasensors combine the advantages of electrochemical sensing with those of aptamer technology. Different types of AFB1 aptasensors have been reported in the literature; Abnous *et al.* (2017) employed a gold electrode coated with complementary DNA strands based on a π-shaped structure; a macroporous MoS_2-AuNPs film was used as a support for tetrahedral DNA structures by Peng *et al.* (2018); and Wang *et al.* (2021) developed an aptasensor based on iron porphyrin organic porous material loaded with gold nano-bipyramids. While the unique multi-strand structural arrangements of these studies provide advantages such as mechanical rigidity and structural stability through DNA hybridization of complementary base pairs between the aptamer and support strands, the overall electrode construction protocols employed involve expensive chemical entities and therefore can be seen as costly and difficult to replicate for on-site monitoring. On the other hand, the employment of solely single-stranded DNA with affordable electrode signal enhancers, such as carbon-based nanomaterials may provide an efficient and cost-effective alternative protocol. Further, methylene blue is a commonly used redox tag to facilitate electron transfer between MB and a given electrode, with the efficiency being dependent on the selected aptamer (Chen and Wang 2020; Wang and Zhao 2020).

Table 2.1. Current electrochemical sensors for AFB1 detection in foods.

	Sample	LOD	%Recovery	Reference
Aptasensor	Corn, rice, chilli powder	4.56 ng mL^{-1}	91-110	Vijitvarasan, Cheunkar and Oaew (2022)
	Nuts, corn, soybeans	0.01 nM	88-95	Ong *et al.* (2023)
	Corn, wheat, oats	0.02 ng mL^{-1}	95-107	Pan *et al.* (2022)
	Peanuts, peanut butter, peanut oil	0.33 pg mL^{-1}	98-106	Lv *et al.* (2023)
	Peanuts, walnuts, almonds	0.45 pg mL^{-1}	95-110	He *et al.* (2023)
Magnetic NP-based sensor	Beer, barley	6.12 μg L^{-1}	94-97	Pezeshkpur, Tadayon and Sohrabi (2023)
	Corn, wheat	0.05 μg kg^{-1}	70-91	Lin *et al.* (2023a)
	Animal feed	0.45 pg mL^{-1}	92-101	Hong *et al.* (2021)
	Peanuts	0.90 pg mL^{-1}	96-120	Becheva *et al.* (2019)
	Peanut oil	0.40 pg mL^{-1}	97-115	He *et al.* (2020)
MOF-based sensor	Wheat flour	8.30×10^{-4} ng mL^{-1}	98-106	Jahangiri–Dehaghani, Zare and Shekari (2022)
	Walnuts	5.39 fg mL^{-1}	88-106	Lv *et al.* (2022)
	Beer	6.70×10^{-7} ng mL^{-1}	96-103	Wang *et al.* (2019)
	Milk, corn, rice	0.35 ng mL^{-1}	90-104	Jia *et al.* (2020)
	Rice, corn flour	31.0 ng L^{-1}	96-104	Meng, Gan and Tian (2022)

2.4) Zearalenone

Zearalenone (**Figure 2.2**) is a non-steroidal estrogenic mycotoxin produced by the *Fusarium* fungi species widely found in mouldy maize, wheat, and rice, as well as other cereal and dairy products (Yan *et al.* 2022b). Its resistance to environmental changes and heat treatments during food storage and processing raises health concerns regarding ZEN exposure (Han *et al.* 2022). The rapid conversion of ZEN to its zearalenol metabolites in the gastrointestinal tract occurs shortly after ingestion in animals (Rogowska *et al.* 2022). Constituting a phenol ring in its structure similar to that of the 17β-estradiol hormone, competition occurs with these endogenous hormones for estrogen receptor binding sites, which in turn affect the function of

estrogen-responsive genes; this consequently results in reproductive dysfunctions such as infertility, abortion and stillbirth (Zhou *et al.* 2022). In addition, ZEN has been reported to exhibit immunosuppressive, hepatotoxic, genotoxic, and neurotoxic effects and has consequently been recognized as a type III carcinogen by IARC (Hao *et al.* 2022).

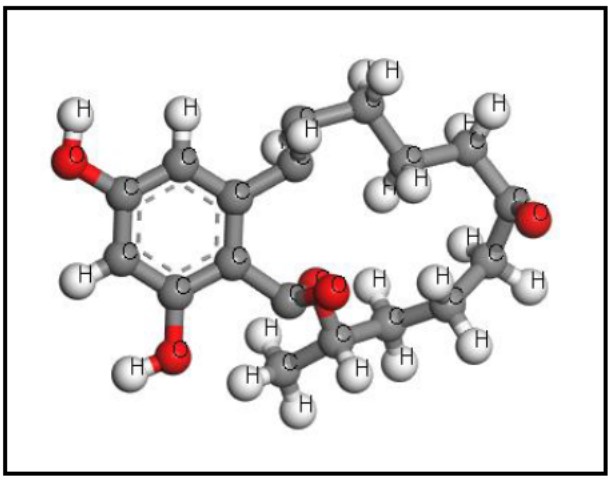

Figure 2.2. A 3D representation of ZEN computed at B3LYP/6-31G** level of theory.

Most analytical approaches employed for the detection of ZEN include techniques such as high-performance liquid chromatography (Koch, Mauch and Riedel 2022), gas chromatography-mass spectrometry (Pack *et al.* 2020), liquid chromatography-mass spectrometry (Lv *et al.* 2021), and immunochemical analyses (Liu *et al.* 2022a). Recently, however, much attention has been gained regarding electrochemical sensors due to their potential for on-site monitoring, low cost, simplicity, fast response, high sensitivity, and high specificity (Moro *et al.* 2020; De Rycke *et al.* 2021; Caglayan, Şahin and Üstündağ 2022; Duan *et al.* 2022; Niazi *et al.* 2022; Sohrabi *et al.* 2022a; Yan *et al.* 2022a) (**Table 2.2**). In terms of current ZEN sensing applications, Jiang *et al.* (2019) employed Pt NPs for the enhancement of a MoS_2-thionin-based sensor; a monoclonal antibody was applied on an Au NP modified sensing platform by Shang *et al.* (2022); and He and Yan (2020) utilized a nicking enzyme in a $CoSe_2$/Au nanorod composite decorated on a gold electrode. While these approaches are highly sensitive, these methodologies tend to involve expensive chemical entities and electrode materials. As such, it is noted that the incorporation of polymers such as PEG can be viewed as cheaper alternative materials while maintaining analyte sensitivity in electrochemical sensor construction (Abbasi *et al.* 2022; Qian *et al.* 2022b; Rahim and Mahmoud 2022; Mohammadpour *et al.* 2023; Swiech, Majdecki and Bilewicz 2023).

Table 2.2. Current electrochemical sensors for ZEN detection in foods.

	Sample	LOD	%Recovery	Reference
Aptasensor	Corn oil	0.21 pg mL^{-1}	94-106	Yao *et al.* (2022)
	Corn flour	29.3 ng kg^{-1}	N/A	Zhao *et al.* (2022a)
	Corn flour	0.39 pg mL^{-1}	93-105	Chen *et al.* (2022d)
	Corn	0.0064 ng mL^{-1}	95-119	Guo *et al.* (2023c)
	Corn powder	3.10×10^{-12} mol L^{-1}	83-98	Liao *et al.* (2023)
Magnetic NP-based sensor	Maize, wheat	0.06 μg kg^{-1}	82-118	Hua *et al.* (2022)
	Beer, wine	0.001 ng mL^{-1}	96-111	Chen *et al.* (2021)
	Corn, beer	0.98 ng mL^{-1}	99-102	Liu *et al.* (2020a)
	Corn, rice, oats	0.22 pg mL^{-1}	95-105	Jiang *et al.* (2021)
	Wheat flour	0.38 μg kg^{-1}	82-120	Lin *et al.* (2023b)
MOF-based sensor	Maize	1.37 fg mL^{-1}	94-103	He and Yan (2020)
	Maize, wheat	0.36 pg mL^{-1}	95-109	Sun *et al.* (2022b)
	Almonds	7.44 nM	92-110	Zhang *et al.* (2023)
	Beer, corn, peanut	3.50 fg mL^{-1}	96-106	Duan *et al.* (2022)
	Corn flour, corn oil, oat flour	0.0035 ng mL^{-1}	85-101	Li *et al.* (2023)

2.5) Ochratoxin A

Ochratoxin A (**Figure 2.3**) is a common mycotoxin produced by the *Aspergillus* and *Penicillium* fungi species widely found in food commodities such as wheat, maize, nuts, coffee, beer, and cocoa (Wang *et al.* 2022c). It exhibits robust stability in conditions that are humid and ambient in temperature, presenting challenges regarding grain harvesting, storage, processing and transportation (Liu *et al.* 2022d). The nephrotoxic nature of OTA has been characterized by cellular damage due to oxidative stress, apoptosis, and DNA fragmentation based on its affinity toward proximal tubule epithelial cells in humans and animals (Khoi *et al.* 2021). In addition, it has also been reported that OTA exhibits carcinogenic, teratogenic, hepatoxic and immunosuppressive effects, leading it to be classified as a group 2B carcinogen by the IARC (Chen *et al.* 2022b).

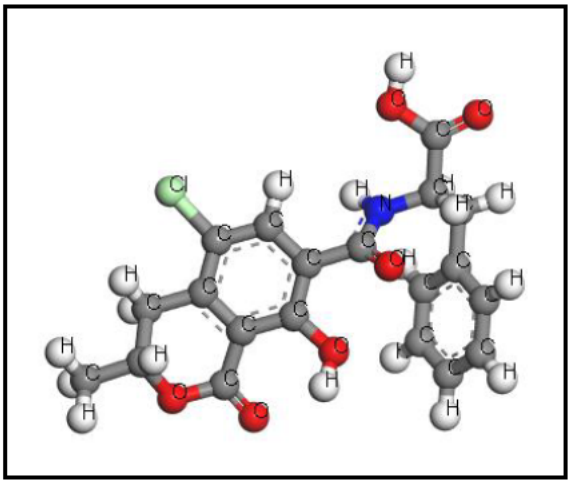

Figure 2.3. A 3D representation of OTA computed at B3LYP/6-31G** level of theory.

Most traditional methods used for OTA analyses include thin-layer chromatography (Teixeira *et al.* 2011), mass spectrometry (Huang *et al.* 2014), high-performance liquid chromatography (Öncü Kaya *et al.* 2019), and immunochemical analyses (Karachaliou *et al.* 2022). While these techniques are established, recent interest in electrochemical sensors has surged due to their significant advantages, such as high sensitivity, low cost and experimental simplicity (Khataee *et al.* 2021) (**Table 2.3**). In addition, the use of metal-organic frameworks has surged regarding applications in sensors (Palakollu *et al.* 2022). With regard to current MOF-based OTA detection applications, Qiao *et al.* (2021) incorporated 2D Cu-TCPP nanosheets with a DNA walker machine and Ag NPs; Jahangiri–Dehaghani, Zare and Shekari (2023) developed a Cu HKUST-1 MOF-based sensor with Au NPs decorated on carbon nanodots; and an electrochemical sensor based on a PCN-223-Fe MOF supported with AgPt bimetallic NPs was constructed by Zhang, Xu and Qiang (2020). While these are dedicated methods, it can be argued that the complexity and specialized availability of the electrode schemes and materials, respectively, may prove difficult and costly to replicate for on-site testing. As such, the advent of relatively affordable carbon materials, such as graphene oxide, utilized with MOFs has gained momentum in recent years, with multiple applications reported regarding sensor development (Rezvani Jalal *et al.* 2020; Wachholz Junior, Deroco and Kubota 2022; Wang *et al.* 2022f; Zhao *et al.* 2022b; Sun *et al.* 2023b).

Table 2.3. Current electrochemical sensors for OTA detection in foods.

	Sample	LOD	%Recovery	Reference
Aptasensor	Malt	1.00 pg mL^{-1}	90-96	Hou *et al.* (2023)
	Wine, grape juice, wheat	0.05 ng mL^{-1}	95-107	Guo *et al.* (2022a)
	Corn, wheat, rice	3.40 pg mL^{-1}	98-105	Guo *et al.* (2023a)
	Grape juice	0.40 pg mL^{-1}	98-108	Wang *et al.* (2023b)
	Soybeans, grapes, milk	30.0 pM	83-101	Wang *et al.* (2022a)
Magnetic NP-based sensor	Cornmeal	N/A	91-99	Wang *et al.* (2020)
	Wine, beer	14.0 nM	97-109	Hu *et al.* (2022)
	Wine	0.42 pg mL^{-1}	99-104	Gao *et al.* (2022)
	Wheat, corn, wine	0.13 ng mL^{-1}	85-108	Wu *et al.* (2023)
	Coffee	0.10 ng mL^{-1}	93-99	Kunene *et al.* (2020)
MOF-based sensor	Wine	10.0 pg mL^{-1}	91-105	Li *et al.* (2018b)
	Corn, orange juice	0.29 pg mL^{-1}	92-97	Huang *et al.* (2023)
	Wheat, corn	0.28 ng mL^{-1}	82-112	Wei *et al.* (2023)
	Wine, corn	14.0 fg mL^{-1}	96-104	Zhang, Xu and Qiang (2020)
	Corn flour	4.30×10^{-3} ng mL^{-1}	96-110	Jahangiri–Dehaghani, Zare and Shekari (2023)

Further, an understanding of the electrochemical methods underlying the employed sensors is required regarding the qualitative and quantitative analyses of this work.

2.6) Electrochemical methods

Electrochemical methods are based on probing an electrochemical reaction between the target analyte and its recognition element (Cesewski and Johnson 2020). The instrumentation is based on a three-electrode system (**Figure 2.4**) that constitutes a working electrode, an auxiliary electrode and a reference electrode that facilitates the varying of an applied potential to detect and evaluate a current response from an electroactive species dissolved in an electrolyte solution (Gosser 1993). Recently, much attention has been gained due to their potential for on-

site monitoring, low cost, simplicity, fast response, high sensitivity, and high specificity (Moro *et al.* 2020; De Rycke *et al.* 2021; Caglayan, Şahin and Üstündağ 2022; Duan *et al.* 2022; Niazi *et al.* 2022; Sohrabi *et al.* 2022a; Yan *et al.* 2022a). Of these methods, voltammetric and impedimetric measurements are the most commonly employed in mycotoxin sensing (Evtugyn and Hianik 2019). As such, the methods employed in this study include cyclic voltammetry, electrical impedance spectroscopy, and differential pulse voltammetry.

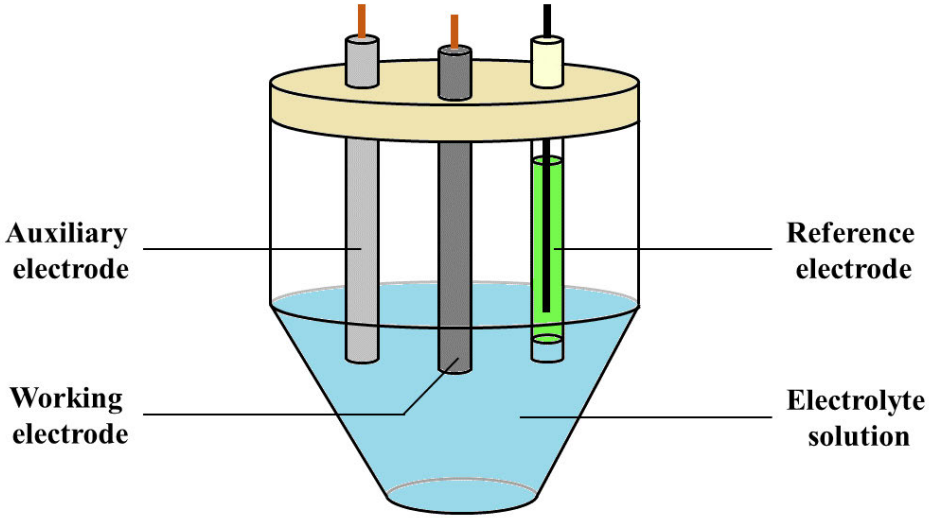

Figure 2.4. Schematics of three-electrode system used in electrochemical measurements.

2.6.1) CV

CV is a widely applied electrochemical technique that provides experimental insights into the kinetic properties of a given chemical system by investigating its oxidation and reduction processes (Marken, Neudeck and Bond 2010). It holds a plethora of applications in a diversity of fields such as chemistry, neuroscience, electrical engineering, materials science, cell biology, condensed-phase physics and photonics (Espinoza *et al.* 2019; Chavan *et al.* 2022; Hattori, Matsuda and Seki 2022; Ratautaite *et al.* 2022; Shinoda, Takase and Shimizu 2023).

In a typical CV analysis (**Figure 2.5**), if an initial applied potential (first switching potential) is scanned in a positive direction of increasing voltages, it is said to induce a cathodic current peak response from the electroactive species being investigated (Kissinger and Heineman 1983). This phenomenon occurs as a result of the working electrode reaching a potential negative enough for it to act as a strong reductant, causing the analyte to gain an electron from it (reduction). This process continues until the concentration of the reduced species near the

surface of the electrode diminishes, resulting in a gradual decay of the current peak. At this point (second switching potential), the potential scan is now reversed, scanning in the negative direction of decreasing voltages back to the first switching potential, resulting in an anodic current peak response. This happens due to the electrode holding a potential positive enough to be a strong oxidant, resulting in the analyte losing an electron to it (oxidation). Finally, the current peak is subsequently observed to be depressed due to the decrease in concentration of the oxidized electroactive species at the electrode surface.

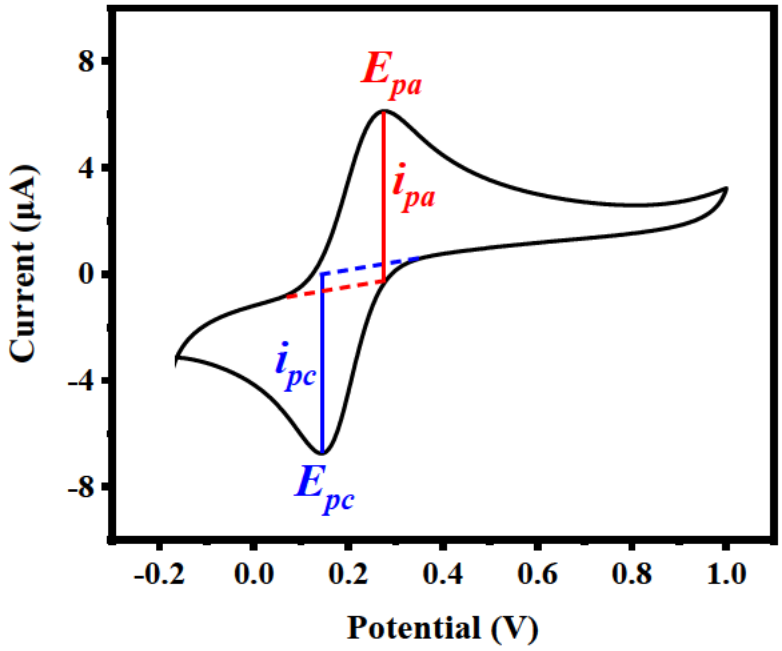

Figure 2.5. A typical cyclic voltammogram depicted in CV analysis.

For a reversible system, the quantity $E^{0\prime}$ lies centred between E_{pa} and E_{pc} in a given voltammogram, as expressed by:

$$E^{0\prime} = \frac{E_{pa} + E_{pc}}{2} \tag{2.1}$$

where $E^{0\prime}$ is the formal reduction potential (V), and E_{pa} and E_{pc} stand for the anodic and cathodic peak potentials (V), respectively (Kissinger and Heineman 1983).

E_{pa} and E_{pc} may also be represented by the following equations:

$$E_{pa} = \mathrm{a} + \frac{2.303RT}{(1-\alpha)nF}\log \upsilon \tag{2.2}$$

$$E_{pc} = \mathrm{b} - \frac{2.303RT}{\alpha nF}\log \upsilon \tag{2.3}$$

where *n* is the number of electrons transferred, α the transport coefficient, *R* the universal gas constant (J K^{-1} mol^{-1}), T the temperature (K), and *F* the Faraday's constant (C mol^{-1}) (Thomas *et al.* 2015).

Finally, the peak current is described by the Randles-Sevcik equation for a reversible system:

$$i_p = (2.69 \times 10^5) n^{3/2} A C D^{1/2} \upsilon^{1/2} \tag{2.4}$$

where i_p is the peak current (A), A the active electrode surface area (cm^2), C the concentration (mol cm^{-3}), *D* the diffusion coefficient (cm^2 s^{-1}) and υ the scan rate (V s^{-1}).

2.6.2) EIS

Electrochemical impedance spectroscopy is a powerful technique capable of characterizing the interfacial electrical properties between materials and conducting electrodes, such as in heterogeneous cells (Macdonald and Johnson 2018). Consequently, EIS is critical in understanding the processes behind sensor recognition events typical of varying components, including nucleic acids, metal oxide nanoparticles, polymers and carbon-based nanomaterials (Magar, Hassan and Mulchandani 2021). In addition to sensors, it is commonly employed in applications dealing with power source evaluations and corrosion analysis (Braz *et al.* 2022; Brett 2022; Wei *et al.* 2022).

The technique is based on applying a small electrical stimulus to the electrode interface of the electrochemical system, such as a single-frequency voltage, and measuring the response of the corresponding current (Macdonald and Johnson 2018). Mathematical Fourier transformation treatment of the resulting sinusoidal alternating current response is then applied, reducing the complicated time-based equations into a form analogous to Ohm's law for direct current. Integrating the complex number plane, the impedance is calculated from the current and voltage emanating from the phase shift (real number component) and amplitude (imaginary number component) of the resulting current waveform at the applied frequency.

The Randles equivalent circuit (**Figure 2.6a**) is applied regarding the fitting of data for the Nyquist plot (**Figure 2.6b**). The circuit elements represent specific properties pertaining to the electrochemical system; solution resistance (R_s), electron transfer resistance (R_{ct}), reflected by the semicircle arc depicting kinetic control, double layer capacitance (C_{dl}), and Warburg impedance (W), which is exhibited by a straight line emanating at the end of the semicircle at a 45° angle, indicating diffusion control (Macdonald and Johnson 2018).

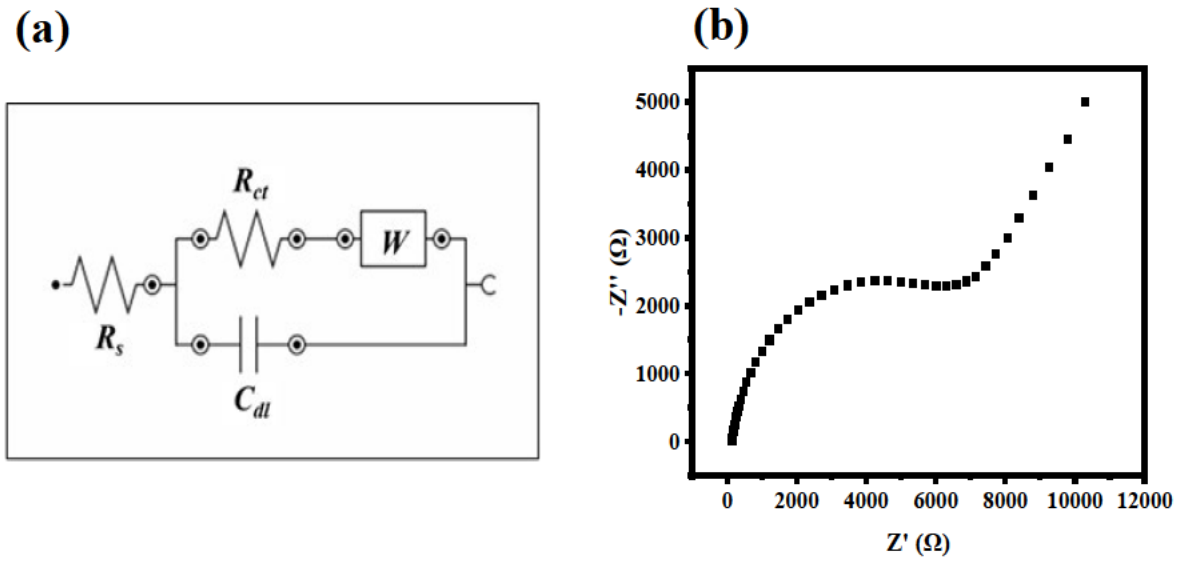

Figure 2.6. (a) Randles equivalent circuit and **(b)** typical Nyquist EIS plot.

2.6.3) DPV

Differential pulse voltammetry is an important technique with significant sensitivity advantages over CV, contributing to the preference for DPV in quantitative analyses (Hussain and Silvester 2018). This is attributed to the comparatively minimal interference of the background current against small changes in the applied potential (Kashyap and Kumar 2022). Consequently, DPV holds applications in many fields, such as sensors, medical studies, environmental monitoring, and the food and pharmaceutical industries (Li, Chen and Chen 2022; Modarresi *et al.* 2022; Ramkumar *et al.* 2022; Senthil Kumar *et al.* 2022; Manh *et al.* 2023).

The technique is based on the step-functional change of applied potential in the form of continuous pulses at fixed time intervals (Aoki, Tokuda and Matsuda 1984). The sensitivity of

the corresponding analyte current response is optimized upon variation of derived experimental parameters pertaining to the electrode reaction rate constant, transfer coefficient, and potential-time waveform. Consequently, for one-half of a reversible redox reaction, the peak current at the corresponding potential is ascertained for quantitative analysis (**Figure 2.7**).

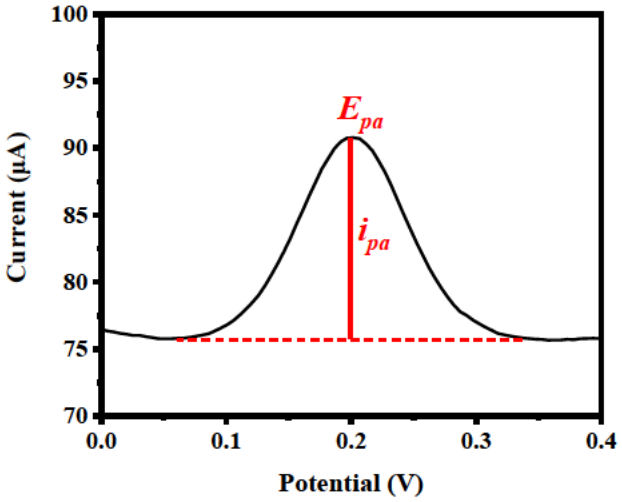

Figure 2.7. A typical differential pulse voltammogram depicted in DPV analysis.

Consequently, an investigation into materials employed for the enhancement of these methods for sensor development is required regarding mycotoxin detection.

2.7) Nanomaterials

Nanomaterials are defined as materials exhibiting at least one size dimension in the range of 1-100 nm (Baig, Kammakakam and Falath 2021). They can be broadly classified into five groups, namely biomolecule-derived, metallic, polymeric, ceramic-based, and carbon-based NMs (Sajid 2022). In addition, they denote superior physical and chemical properties over larger materials of the same composition, including size, surface area and distribution, shape, stability and structure (Ahmed *et al.* 2022). NMs are applied in a diversity of sectors such as biotechnology, cosmetics, aerospace, health, environment, and energy applications (Adegoke and Maxakato 2022; Gupta *et al.* 2022; Pathak and Dhakate 2022; Shahcheraghi *et al.* 2022; Chen, Zhang and Huang 2023; Tong *et al.* 2023). Further, interest has surged regarding the employment of NMs and their composites in the construction of electrochemical sensors due to their promising electrical, optical and structural characteristics (Ghalkhani *et al.* 2022; Kant *et al.* 2022; Karimi-Maleh *et al.* 2022; Kaya *et al.* 2022; Niazi *et al.* 2022).

2.7.1) Magnetic nanoparticles

Magnetic nanoparticles commonly consist of magnetic elements such as iron, cobalt and nickel and their chemical compounds (Ganapathe *et al.* 2020). They are widely used in separation technology, protein immobilization, catalysis, medical and environmental sciences, and the food industry (Liu *et al.* 2020b; Chubarov 2022; Mohamed Noor *et al.* 2022; Patil and Rathod 2022; Verma *et al.* 2022; Wang *et al.* 2022e; Yilmaz *et al.* 2022). The polymorphs include magnetite (Fe_3O_4), which is black, maghemite (γ-Fe_2O_3), which is yellow, and hematite (α-Fe_2O_3), which is red, depending on the crystalline structure (Voss *et al.* 2020). In particular, Fe_3O_4 NPs are increasingly attracting interest as they exhibit low toxicity, facile functionalization and high biocompatibility (Wang *et al.* 2023a). Moreover, Fe_3O_4 NPs exhibit significant characteristics such as high electrical conductivity, high magnetic susceptibility and superparamagnetism, which favours their employment as key components in sensing applications (Socas-Rodríguez *et al.* 2020).

2.7.2) Metal-organic frameworks

MOFs are regarded as highly porous crystalline materials constituting metal ions or clusters interconnected with organic linkers (Marimuthu *et al.* 2022). They have remarkable intrinsic properties such as thermal and chemical stability, tunable pore size and high surface area (Mallakpour, Nikkhoo and Hussain 2022). As such, the use of MOFs has surged in a diversity of applications such as drug delivery, gas storage, solar cells, batteries, and sensors (Chu, Sun and Cui 2022; Demir Duman *et al.* 2022; Guo *et al.* 2022b; Sohrabi *et al.* 2022b; Uğur, Gencer Imer and Gülcan 2022). In particular, Ni-MOF with trimesic acid linkage has been found to exhibit strong optical, structural and electrical properties well suited for sensor development (Murad *et al.* 2022).

2.7.3) Carbon-based nanomaterials

Recent interest has surged regarding the application of carbon-based NMs due to their numerous properties, such as high electrical and thermal conductivity, large surface area, unique optical and mechanical properties, and small size (Díez-Pascual 2021). Hence, they boast several applications in fields such as solar energy storage, catalysis, pollutant elimination, gas storage and sensors (Azara, Belbessai and Abatzoglou 2022; İnada, Arman and Safaei 2022; Liu *et al.* 2022b; Singhal *et al.* 2022; Cai *et al.* 2023). They can be divided

into specific types depending on their spatial dimensions, such as fullerenes, carbon nanotubes and graphene (Pan *et al.* 2019). In addition, the carboxylation of multi-walled carbon nanotubes and reduced graphene oxide allows for significant improvement regarding solvent dispersibility, which promotes the homogenous mixing of electrode materials for enhanced sensor performance (Kobets *et al.* 2019; Wang *et al.* 2022g).

2.7.4) Synthesis of nanomaterials

The selected nanomaterial synthesis approach is critical for controlling desired properties such as morphologies, surface charges, dimensions and physicochemical attributes for sensor construction (Qian *et al.* 2021). The synthesis of NMs is classified into two main approaches, namely the top-down and bottom-up methods (Indiarto *et al.* 2022). The former is defined by the transformation of bulk material into nano-sized dimensions, while the latter involves building material from the smallest dimensions and coalescing into larger forms from the atom up (Saleh 2021). Of these approaches, bottom-up synthesis is preferred owing to the disadvantages denoted by the top-down method, such as difficulties in obtaining proper particle shape and size (Abid *et al.* 2022). Among the bottom-up methods, the co-precipitation process is preferred over the chemical deposition method owing to advantages such as achieving more frequency in obtaining fine and uniform particle sizes, and better homogeneity of the species distribution (Hachem *et al.* 2022). In addition, this method holds advantages over green synthesis, which tends to exhibit low yield and poor chemical stability (Dikshit *et al.* 2021). Thus, the application of the co-precipitation method is found to control the dimensions of NMs to occur in the nano-size range of 1-100 nm, the properties of which are reported to enhance the conductivity and overall performance of sensors (Elahi and Rizwan 2021).

2.8) Characterization methods

2.8.1) AF4

Asymmetrical Flow Field-Flow Fractionation is an elution-based method most popular for the fractionation and characterization of NPs by hydrodynamic size (Contado 2017). The technique is characterized by the separation of an analyte induced by an external flow field applied perpendicular to the direction of the sample flow through a thin channel (Wahlund and Giddings 1987). AF4 is employed in a plethora of fields such as biotechnology, environmental

chemistry, pharmaceutics and polymer technology (Shakiba *et al.* 2022; Bai *et al.* 2023; Guo *et al.* 2023b; Qu *et al.* 2023; Ventouri *et al.* 2023).

The separation takes place in the channel consisting of non-porous and porous plates with a thin spacer in between clamped together (Wahlund and Giddings 1987; Cölfen and Antonietti 2000) (**Figure 2.8**). The porous plate is made up of a membrane that is supported by a frit, together called the accumulation wall. The sample, carried by a laminar flow of solvent, enters through the tip of the channel (tip flow). This stream exhibits a parabolic flow profile and the resulting perpendicular crossflow. The latter is induced by the tip flow channelling through the permeable accumulation wall. Against the longitudinal channel flow, a counterflow of solvent (focus flow) is introduced independently to focus the sample, promoting an increase in signal resolution and a reduction of peak band broadening; this is due to the subsequent equilibration of the diffusional and Brownian forces (relaxation or focus step). Simultaneously, the sample particles are pushed by the crossflow toward the accumulation wall, at which point diffusion and crossflow strength partition the particles. Subsequently, the focus flow is turned off, and the separated sample species proceed through the channel. The laminar profile of the channel flow ensures that smaller particles are carried away by the central parabolic high-velocity streamlines and are eluted first, followed by the larger particles forced slowly along by the low-velocity streamlines at the accumulation wall. Ultimately, the sample particles are separated by hydrodynamic diameter and are ascendingly eluted.

Subsequently, the separated particles flow to the multi-angle light scattering detector. The principle of MALS entails the use of an incident laser to illuminate the centres of the sample particles, at which point the scattered light intensities are measured by multiple surrounding detectors situated at different angles for the determination of particle size and molar mass (**Figure 2.9**) (Lohrke, Briel and Mäder 2008). As such, for a monodispersed suspension of spherical particles, it is observed that the intensity of scattered light varies smoothly with the angle of scattering. This trend tends to occur in the variation of angles in the range between 0° and 180° (Zimm 1948; Cowie and Arrighi 2007). The calculated particle size limitations include below 10 nm and above 200 nm depending on the wavelength of the incident laser, shape-factor fit approximations and optical properties of the particles (Korgel, van Zanten and Monbouquette 1998; Podzimek 2011). Essentially, the scattered light intensity is determined as a response by the Rayleigh-Gans approximation (Wyatt 2014) to elucidate the radius of gyration of a given sample for particle size distribution analysis.

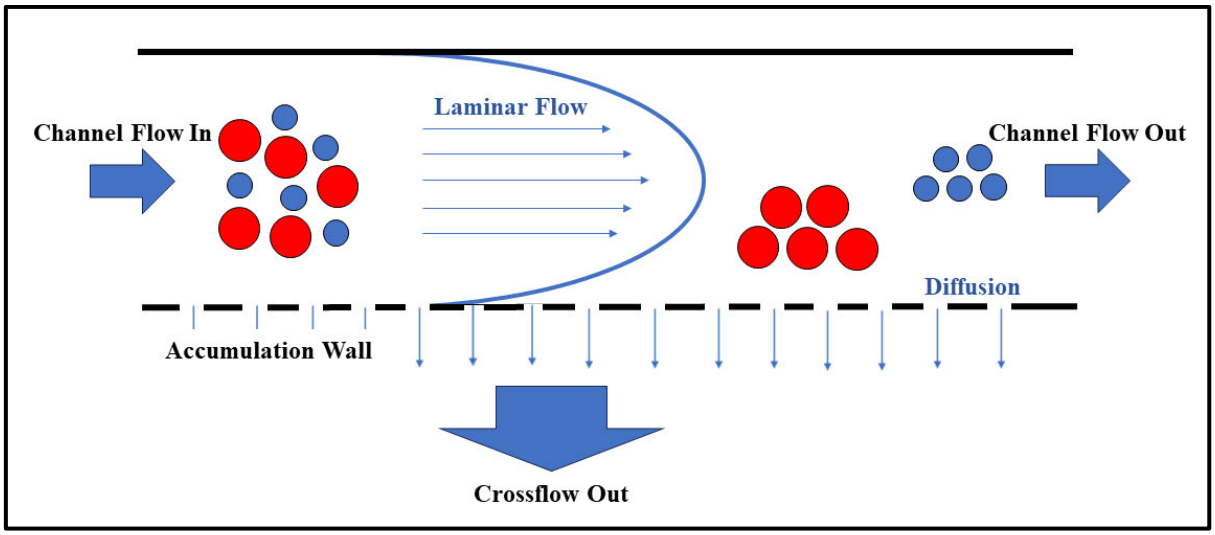

Figure 2.8. Working principle of AF4 separation, adapted from Postnova Analytics GmbH, Germany (Postnova 2017).

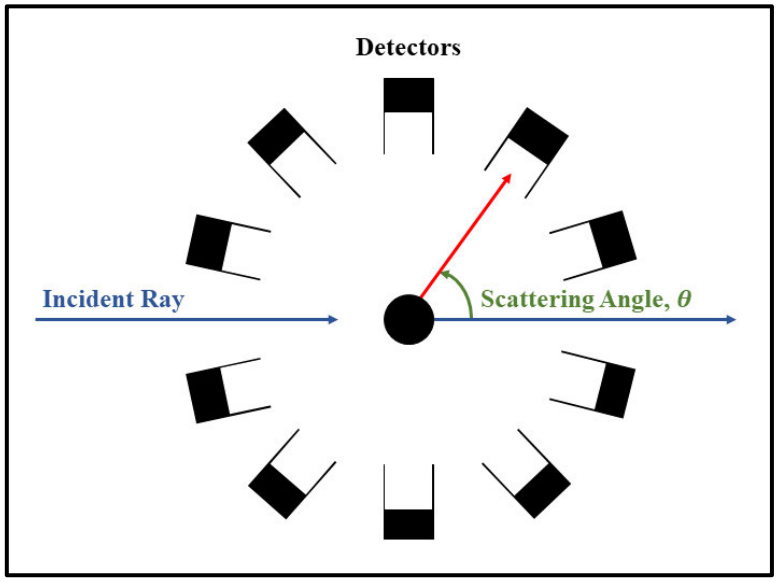

Figure 2.9. Light scattering principle of MALS detector, adapted from Postnova Analytics GmbH, Germany (Postnova 2017).

2.8.2) SpICP-MS

Conventionally, inductively coupled plasma-mass spectrometry in batch mode has been employed in a plethora of fields such as food, environmental and life sciences, forensics and pharmaceutics, which perform trace element measurements at very low concentrations (Olesik 1991; Wilschefski and Baxter 2019; Balaram, Rahaman and Roy 2022; Nawrocka *et al.* 2022; da Silva and Arruda 2023; Ruffolo *et al.* 2023). On the other hand, recently, interest in

applications of single particle ICP-MS has surged, where it is employed for the detection and size characterization of nanomaterials in aqueous dispersions (Montaño *et al.* 2016).

The sample is introduced in dispersion form, following which the analyte is subsequently nebulized, desolvated, atomized, and ionized in contact with the argon-based high-temperature plasma (Montaño *et al.* 2016). Thereafter, the target ions are extracted from the plasma interface and then separated under vacuum by the mass spectrometer using the particles' mass-to-charge ratio (m/z). Consequently, the instrument detects charges of particles equivalent to one; thus, m/z is taken as identical to the atomic mass of the particle. In spICP-MS, this is considered a signal pulse event. Finally, an electron multiplier detector counts the ions, after which results are obtained and interpreted in the data management software.

The mass-based diameter, *d*, of a spherical particle is represented by:

$$d = \left(\frac{6q_{col}t_{dt}\eta_{neb}c_{Ti}}{0.5994\pi\rho}\right)^{1/3} \tag{2.5}$$

where q_{col} is the nanoparticular colloidal sample flow rate, t_{dt} the dwell time, η_{neb} the nebulizer transport efficiency and ρ is the particle density (Dan *et al.* 2015).

2.8.3) XRD

X-ray diffraction is an analytical approach used to provide crystalline information about the structure of materials at an atomistic level (Vydrina *et al.* 2023). Its wide range of analysis includes material science applications in cement, plastics, clays and minerals, and carbon-based materials, metals, and alloys (Khan *et al.* 2020). Recently, the characterization of electrode materials using XRD has gained prominence in the field of electrochemical sensor development (Bölükbaşı *et al.* 2022; Chen *et al.* 2022c; Ghalkhani and Sohouli 2022; Rezvani Jalal *et al.* 2022; Ali *et al.* 2023).

The premise of the technique is based on the interaction of the sample atoms with an incident X-ray laser (Elton and Jackson 1966; Bunaciu, Udriştioiu and Aboul-Enein 2015). Upon contact with the electromagnetic radiation of the X-ray beam, the electrons of the sample atom are forced into a receptive vibration, at which point the atom emits radiation of the same frequency. An arbitrary angle of scattered radiation is selected for measurement, where each element exhibits a characteristic XRD spectrum response.

The experiment follows the satisfaction of the conditions for Bragg's law (Elton and Jackson 1966; Bunaciu, Udriştioiu and Aboul-Enein 2015):

$$n\lambda = 2d \sin\theta \tag{2.6}$$

where n is an integer, λ the wavelength of the X-ray, d the interplanar spacing exhibiting the diffraction, and θ the diffraction angle.

Finally, the crystalline sizes of a given material can be calculated from their XRD peaks of maximum intensity using the Debye-Scherrer equation:

$$D = \frac{k\lambda}{\beta \cos\theta} \tag{2.7}$$

where D is the crystalline size, k the shape factor, λ the X-ray wavelength and β the full width at half maximum intensity (Sivagami and Asharani 2022).

2.8.4) SEM, TEM and EDS

Scanning and transmission electron microscopy are primary techniques used to pictorially determine the morphological characteristics of samples from a plethora of fields ranging from biological media and environmental contaminants to energy storage and conversion materials (Li *et al.* 2022; Parker *et al.* 2022; Zachman *et al.* 2023). On the other hand, energy-dispersive X-ray spectroscopy, utilized for qualitative elemental analysis, is often used in tandem with the aforementioned microscopy techniques for a similarly diverse application range (Bahmani and Mostofinejad 2022; Mashtalyar *et al.* 2022; Mo *et al.* 2022; Patel *et al.* 2022; Zhang *et al.* 2022b).

The basic principle of electron microscopy is exhibited by the irradiation of a given sample by highly focused electron beams under vacuum conditions (Inkson 2016). From this point, response signals emitted from the sample are collected by detectors in correlation with the electron beam incident location, forming a corresponding image. In addition, the key differences between SEM and TEM are more related to the energy expended by the designated instrument, with the former focused on surface imagery while the latter provides more penetrative intrinsic structural information. In fact, the X-rays released due to the transition of energy levels of electrons from bombarded sample atoms are observed to denote specific

energy responses characteristic of individual elements; this information is subsequently plotted to form the corresponding EDS spectrum of the sample.

2.8.5) FTIR

Fourier transform infrared spectroscopy is commonly applied to qualitatively determine the characteristic functional groups of a given compound in fields such as forensic science, pharmaceutics, food and beverages, and environmental science (Alkhuder 2022; Sabbagh *et al.* 2022; Zhang *et al.* 2022a; Ebada *et al.* 2023; Paul *et al.* 2023).

FTIR is based on the absorption of electromagnetic radiation by chemical bonds present in a given sample (Ismail, van de Voort and Sedman 1997). This occurs in the infrared spectrum, prompting vibrational and rotational energy response transitions at a molecular level. These responses exhibit characteristic spectra representative of specific functional groups, thus denoting the molecular "fingerprint" of a given sample. Consequently, FTIR has thus been widely utilized for the characterization of materials used in electrochemical sensor construction (Nallusamy and Sujatha 2021; Iftikhar *et al.* 2022; Karadurmus *et al.* 2022; Rahman *et al.* 2023; Singhal and Khan 2023).

2.9) Computational methods

2.9.1) DFT

The applications of density functional theory for chemists were first explicitly described in the Kohn, Becke and Parr (1996) paper almost thirty years ago, where contributions pertaining to important concepts such as electronegativity, hardness and chemical reactivity index were highlighted. The theory itself centres around electronic density distribution emanating from principles derived from electronic ground state structure supported by appropriate energy functional approximations. From a computational viewpoint, the empirical elucidation of chemical phenomena, including electrical polarizability and excitation energy, proves profitable in promoting synergistic outlooks relating to experimental and computational chemistry (Honarparvar, Kanchi and Bisetty 2019; Ayyappa *et al.* 2021; Kanchi *et al.* 2021; Xing *et al.* 2022; Roohi and Pouryahya 2023).

2.9.2) Molecular docking

The underlying principle of molecular docking centres on ascertaining the best possible structural configuration between a relatively large receptor molecule and a smaller ligand compound by applying spatially cognisant *in-silico* algorithms (Trott and Olson 2010). Many works in the reported literature focus in-depth on docking studies regarding protein-ligand interactions for drug design and associated efforts (Gnanaraj *et al.* 2022; Danel *et al.* 2023; Daoui *et al.* 2023), however, its potential for use outside this niche area is promising, such as in sensor applications (Mehmandoust *et al.* 2022; Bouali *et al.* 2023; Kunene *et al.* 2023).

2.9.3) MC simulation

The original molecular chemistry Monte Carlo simulation article by Metropolis *et al.* (1953) describes the process of investigating the energetic properties of individual interacting particles within a system of predefined thermodynamic conditions. The concept lies in probing the probability of a single particle moving to a new state (or remaining in its original position) relative to its neighbour in a given canonical ensemble, which depicts thermal equilibrium akin to ambient temperature laboratory conditions. The calculation is then repeated for the next individual particle, which naturally involves the mathematical application of Monte Carlo integration over simulated periodic configurational space (Mize *et al.* 2022; Attarki *et al.* 2023; de Jesús González and Rangel Vázquez 2023).

2.9.4) MD simulation

The molecular dynamics method was developed to understand the behaviour of a large number of interacting molecules in a given system at equilibrium and non-equilibrium conditions, as first approached by Alder and Wainwright (1959). The calculation allows for the study of molecular energy relaxation phenomena and kinetic property investigations pertaining to the intrinsic motions of a many-body simulation. The implementation of periodic configurational space caters for the representation of a real-life macroscopic system while keeping the number of molecules investigated per unit cell constant (Khosrowshahi *et al.* 2022; Zeng *et al.* 2022; Hu *et al.* 2023).

CHAPTER 3 – MATERIALS AND METHODS

This chapter entails a description of the materials and methods employed in both the experimental and computational studies of this work. The synthesis and characterization of different nanomaterials, along with the fabrication of the electrochemical sensors for each case study are presented.

3.1) Experimental methods

3.1.1) Chemicals and materials

The anti-AFB1 aptamer employed in the study was procured from Whitehead Scientific (Cape Town, South Africa) with the following base pair sequence: 5'-TGGGGTTTTGGTGGCGGGTGGTGTACGGGCGAGGG-3' (Goud *et al.* 2017). The aptamer was modified for study as follows: 5'- Amino C6, 3'- MB azide. Ultrapure water (18.2 $M\Omega\ cm^{-1}$ resistivity at ambient temperature) was prepared by a Milli-Q Advantage A10 Water Purification System (Millipore, Amsterdam, Netherlands). NovaChem Surfactant 100 solution, a special mix of ionic and non-ionic detergents for Field-Flow Fractionation (FFF) applications was purchased from Postnova Analytics (Landsberg, Germany). Iron (III) chloride ($FeCl_3$) (≥99.9%), ammonium hydroxide (NH_4OH) solution (28.0% – 30.0%), sodium sulphite (Na_2SO_3) (≥98.0%), nickel (II) nitrate hexahydrate ($Ni(NO_3)_2{\cdot}6H_2O$) (≥99.0%), trimesic acid (≥95.0%), hydrochloric acid (37%), PEG-4000 (molecular weight 4000 g mol^{-1}), ethanol (≥99.9%), acetonitrile (≥99.9%), methanol (≥99.9%), carboxylated reduced graphene oxide (cRGO), carboxylic acid functionalized multi-walled carbon nanotubes (cMWCNTs), dimethylformamide (DMF) (≥99.9%), magnesium chloride ($MgCl_2$) (≥98.0%), potassium dihydrogen phosphate (KH_2PO_4) (≥99.0%), potassium chloride (KCl) (99.0% – 100.5%), sodium hydrogen phosphate (Na_2HPO_4) (≥99.0%), sodium chloride (NaCl) (≥99.0%), potassium ferricyanide ($C_6FeK_3N_6$) (≥99.0%), potassium ferrocyanide trihydrate ($C_6FeK_4N_6{\cdot}3H_2O$) (98.5% – 102.0%), sodium dihydrogen orthophosphate (NaH_2PO_4) (≥99.0%), boric acid (H_3BO_3) (≥99.5%), sodium tetraborate ($Na_2B_4O_7$) (99%), sodium hydroxide (NaOH) (≥98.0%), N-Hydroxysuccinimide (NHS) (98.0%), 1-[3-(dimethylamino)propyl]-3-ethylcarbodiimide methiodide (EDC) (≥99.0%), 4-Morpholineethanesulfonic acid monohydrate (MES) (≥99.0%), aflatoxin B1 (AFB1), zearalenone (ZEN) and ochratoxin A (OTA) were procured from Merck (Johannesburg, South

Africa). All chemicals used in this study were analytical grade. Commercially available corn flour and rice flour were sourced locally for real sample analysis.

3.1.2) Instrumentation

Single particle ICP-MS analysis was performed on a PerkinElmer NexION 2000 ICP-MS (Perkin Elmer, Shelton, USA) using the Syngistix Nano Application software module. Here, the particle size distribution information was obtained for the synthesized Fe_3O_4 NPs. The transport efficiency (particle frequency method) was determined using 30 nm, 60 nm and 90 nm Au NP standards. Dissolved Fe standard concentrations of 5 μg L^{-1}, 10 μg L^{-1}, 20 μg L^{-1} and 50 μg L^{-1} were used for particle size calibration. Instrumental conditions were optimized for the maximum sensitivity of Fe^{54} (**Appendix 1, Appendix 2**) (ISO 2017). TEM studies were undertaken with an FEI T20 instrument equipped with a LaB6 emitter (Tecnai, FEI) for Fe_3O_4 NPs shape determination. An AF4 system (model AF2000 Multiflow, Postnova Analytics, GmbH, Germany) equipped with UV-vis (SPD-M20A, Shimadzu, GmbH, Germany) and MALS (PN3621, Postnova Analytics GmbH, Germany) detectors was used for the determination of the particle size distribution and shape of PEG-Fe_3O_4 NPs. XRD analyses were performed using a Bruker D8 Advanced Diffractometer to ascertain the crystalline structural characteristics of the electrode materials used in the study. SEM analyses were performed using a $Mira_3$ RISE Scanning Electron Microscope (Tescan, Czech Republic), while EDS measurements were conducted using an energy-dispersive X-ray spectrometry Oxford X-max 20 mm^2 detector and INCA software. FTIR spectra were recorded from 4000 to 400 cm^{-1} on a Cary 630 FTIR Spectrometer (Agilent Technologies, Santa Clara, USA). All electrochemical measurements were performed with a Metrohm AUTOLAB, PGSTAT 302 with a 663A Computrace. The instrument employs an electrochemical cell that utilizes a three-electrode system consisting of unmodified and modified GCEs as the working electrode, Ag/AgCl (3M KCl) as a reference electrode, and platinum wire as the counter electrode, operated with NOVA (v2.1.4) software. The electrochemical cell was purged with nitrogen gas for 30 s prior to each measurement to ensure oxygen interference removal. A layer-by-layer fabrication approach was implemented where bare and modified electrodes were each immersed in separate 10 mL aliquots of specific buffer solutions for respective mycotoxin quantification analyses.

3.1.3) Synthesis of Fe_3O_4 NPs

The chemical synthesis of Fe_3O_4 NPs was undertaken as adapted from Qu *et al.* (1999). Briefly, a 2:1 molar concentration ratio mixture of $FeCl_3$ (in 2 M HCl) to Na_2SO_3 (aqueous) in addition to a dilute aqueous NH_4OH solution was mixed and stirred vigorously to form a black precipitate. This product was eventually settled and separated by a permanent magnet, with the supernatant discarded. Thereafter, the precipitate was washed several times with ultrapure water, with a portion left wet for subsequent PEGylation as described in the next section.

3.1.4) PEGylation of Fe_3O_4 NPs

In this method, an equivalent mass of PEG-4000 and as-prepared wet Fe_3O_4 NPs were mixed with ultrapure water in a 1:2 g/mL ratio. The mixture was then stirred for 1 hr and subsequently sonicated for 30 min using a 150 W ultrasonic bath (3 L capacity, Labotec, Durban, South Africa). Thereafter, the supernatant was removed after 5 min of centrifugation at 3000 rpm, and the product was then washed with ultrapure water for the removal of any unreacted PEG. Finally, a black powder was obtained after drying at room temperature (Mukhopadhyay *et al.* 2012; Antarnusa and Suharyadi 2020).

3.1.5) Synthesis of Ni-MOF

The synthesis of Ni-MOF was adapted from Sel *et al.* (2015). Briefly, independent aqueous solutions of trimesic acid (adjusted to pH 7.0) and $Ni(NO_3)_2{\cdot}6H_2O$ prepared from equivalent masses were mixed and stirred vigorously to form a light green precipitate. The product was then washed repeatedly with ultrapure water and once with ethanol, after which a light green powder was obtained after oven-drying at 80℃ for 12 hrs.

3.1.6) Preparation of working solutions

All working solutions were prepared in ultrapure water unless otherwise stated.

3.1.6.1) Preparation of phosphate-buffered saline solution

A 1 x PBS solution was prepared by mixing dissolved salts of $MgCl_2$, KH_2PO_4, KCl, Na_2HPO_4 and NaCl in a volumetric flask at a pH of 7.4.

3.1.6.2) Preparation of sodium phosphate buffer solution

In a volumetric flask, 0.1 M sodium phosphate solution was prepared by mixing dissolved salts of Na_2HPO_4 and NaH_2PO_4 at pH 7.4.

3.1.6.3) Preparation of $[Fe(CN)_6]^{-3/-4}$ redox probe solution

A 1 mM $[Fe(CN)_6]^{-3/-4}$ redox probe solution was prepared using $C_6FeK_3N_6$ and $C_6FeK_4N_6{\cdot}3H_2O$ made up to mark in a PBS solution at pH 7.4.

3.1.7) Preparation of aptamer binding buffer

The aptamer employed in the study was prepared in a binding buffer of PBS solution at pH 7.4.

3.1.8) Aptamer immobilization on modified electrode

Prior to the aptamer immobilization, the -COOH groups of the cMWCNTs on the modified electrode surface were required to be activated for their binding to the amino-C6 linker (5') of the aptamer by peptide bond formation. This was achieved by using EDC (100 mM) and NHS (100 mM) prepared in MES buffer (100 mM, pH 6.5) for 1 hr.

Thereafter, 10 μL of the aptamer solution (2.5 μM) was further deposited on the electrode and allowed to incubate for 1 hr. At this stage, the modified electrode surface was rinsed with the binding buffer to remove excess unbound aptamer and was subsequently ready for electrochemical analyses.

3.1.9) Preparation of electrode and modification by nanocomposites

Prior to electrode modification, the GCE surface was polished using alumina powder, activated with a 50% methanol solution, and finally rinsed with ultrapure water. After being oven-dried for 2 min at 50℃ and left to cool at room temperature, the electrode was ready to be modified. For this process, the respective nanocomposite was dissolved and homogenized in DMF to form a thick paste; this was then drop-cast on the GCE surface and left to dry and cool as mentioned for subsequent electrochemical analyses.

3.1.10) Electrochemical analyses

For the first case study regarding AFB1, the electrochemical characterization of the electrodes used in the study was conducted using CV and EIS in the aforementioned 1 mM $[Fe(CN)_6]^{-3/-4}$ redox probe solution. This was performed for the investigation of the electron transport properties of the electrodes. A scan rate of 0.025 V s^{-1} was applied for CV at a potential window from -0.2 V to 1.0 V, while an applied constant potential of 0.2 V (frequency from 100 kHz to 0.1 Hz, amplitude of 0.01 V) was utilized for EIS. The applied voltages for EIS were selected from the $E^{\circ\prime}$ potentials obtained from the corresponding CV voltammograms (**Eq. (2.1)**). DPV was implemented for the quantitative analysis of AFB1 on the developed GCE/cMWCNTs-Fe_3O_4 NP/Apt sensor. An indirect sensing method was utilized whereby the response of the 1 mM $[Fe(CN)_6]^{-3/-4}$ solution was evaluated with respect to standard additions of AFB1. Using DPV, this was performed under optimal conditions, which include a scan rate of 0.025 V s^{-1}, a potential window of 0.0 V to 0.4 V, a modulation amplitude of 0.025 V, a step voltage of 0.005 V, deposition time of 60 s, and a deposition voltage of -0.8 V.

Regarding the second case study for ZEN, the electrochemical characterization of the electrodes was conducted using CV at a scan rate of 0.025 V s^{-1} and EIS with an applied constant potential of 0.2 V, respectively, in a 1 mM $[Fe(CN)_6]^{-3/-4}$ redox probe solution. Thereafter, CV was employed to optimize the electrochemical sensitivity of the employed electrodes towards ZEN within a potential window of -0.6 V to 0.2 V at a scan rate of 0.025 V s^{-1} in a 0.1 M sodium phosphate buffer. For the corresponding EIS analysis, a constant potential of -0.2 V was applied. DPV was implemented to assess the effect of the deposition voltage and deposition time on the peak current of ZEN on the constructed GCE/PEG-Fe_3O_4 NP/cMWCNTs sensor. In addition, the quantitative analysis of ZEN, using DPV, was performed under optimal conditions with a scan rate of 0.100 V s^{-1}, a potential window of -0.5 V to 0.2 V, a step voltage of 0.005 V, a modulation amplitude of -0.025 V, a deposition voltage of 0.2 V, and a deposition time of 60 s.

Finally, in the third case study regarding OTA analyses, CV and EIS measurements of 1 mM $[Fe(CN)_6]^{-3/-4}$ redox probe solution were conducted for the electrochemical characterization of the employed electrodes. A scan rate of 0.025 V s^{-1} was applied for CV, while an applied constant potential of 0.2 V was utilized for EIS. Thereafter, CV was employed to optimize the electrochemical sensitivity of the electrodes towards OTA within a potential window of -0.2

V to 1.0 V at a scan rate of 0.025 V s^{-1} in a PBS solution. For the corresponding EIS analysis, a constant potential of 0.5 V was applied. DPV was implemented to assess the effect of the deposition voltage and deposition time on the peak current response of OTA on the developed GCE/Ni-MOF/cRGO sensor. In addition, using DPV, the quantitative analysis of OTA was performed under optimal conditions with a scan rate of 0.025 V s^{-1}, a potential window of 0.1 V to 0.7 V, a step voltage of 0.005 V, a modulation amplitude of -0.025 V, a deposition voltage of -1.4 V, and a deposition time of 0 s.

3.1.11) Preparation of real samples

In this procedure, 1 g of the corn flour or rice flour sample was mixed with 10 mL of organic solvent (pure acetonitrile for AFB1; pure methanol for ZEN and OTA) and subsequently filtered with Whatman No. 1 filter paper. Afterwards, 1 mL of the extracted solvent was diluted with 10 mL of the respective quantitative buffer solution. The solutions prepared for each corn flour and rice flour sample were then spiked with known concentrations of the mycotoxin standard for spike recovery analyses by the standard addition method in triplicate.

3.2) Computational methods

3.2.1) DFT

DFT computations were performed on the 3D-optimised AFB1 structure in the presence of acetonitrile and gaseous form using the B3LYP functional and the 6-31G** basis set (Burke 2012; Lehtola 2019). Analyses based on the highest occupied to lowest unoccupied molecular orbital (HOMO-LUMO) transitions were undertaken to assess the electronic properties of the predicted redox sites pertaining to the analyte. All calculations were performed using the Maestro (v12.8) computer program (Maestro 2021).

3.2.2) Molecular docking

Docking studies were performed on the optimized AFB1 and aptamer structures to predict the active binding site between the two compounds using the Autodock Vina software (Morris *et al.* 1998; Rao and Olson 1999; Dym *et al.* 2002; Trott and Olson 2010). The simulation was based on the utilization of the empirical force field and the Lamarckian Genetic Algorithm, employing free energy calculations for conformational predictions (Morris *et al.* 2009; Arodola

et al. 2020). Various conformations of the potential AFB1-aptamer docked structure were generated, with the model exhibiting the highest absolute binding affinity selected.

3.2.3) MC simulation

MC simulations were performed to assess and interpret the ZEN analyte interactions at an atomistic level. Initially, the ZEN (adsorbate) and GCE/PEG-Fe_3O_4 NP/cMWCNTs (substrate) compounds were constructed conforming to the standard library of parameters of the Material Studio software package developed by BIOVIA (Biovia 2016). Thereafter, the MC analysis, using the Adsorption Locator module in the MS software, was performed to search for the lowest energy (most energetically stable) conformations and subsequently locate the best adsorption site for the ZEN adsorbate onto the final electrode substrate surface. For all simulations, a UNIVERSAL force field (Rappe *et al.* 1992) was applied, and the charges were assigned using the "use current" method. The summation method for the electrostatics and the van der Waals interactions were both set to "atom-based" and the quality of the calculations was set to "ultra-fine".

3.2.4) MD simulation

MD simulations were performed to assess and interpret how Ni-MOF and the OTA analyte interacted at the molecular level. Accordingly, 10 OTA adsorbates with a single Ni-MOF cage structure were prepared using the AL module and the standard library of parameters of the MS software package (Biovia 2016). For all simulations, a UFF (Rappe *et al.* 1992) was applied, and the charges were assigned using the "use current" method. The summation method for the electrostatics and the van der Waals interactions were both set to "atom-based" and the quality of the calculations was set to "ultra-fine".

CHAPTER 4 – RESULTS AND DISCUSSION

In this chapter, the results of the fabricated electrochemical sensors for the detection of AFB1, ZEN and OTA are presented. Also outlined in this chapter are the accompanying computational studies, which aim to supplement and correlate the experimental data for the respective case studies.

4.1) Case Study I: A novel MB-tagged aptasensor for aflatoxin B1 detection in food using Fe_3O_4 NPs substantiated with *in-silico* modelling

This study used an MB-tagged anti-AFB1 aptamer that was immobilized onto a Fe_3O_4 NP-grafted cMWCNTs nanocomposite for the ultrasensitive detection of AFB1. Firstly, the cMWCNTs-Fe_3O_4 NP layer was loaded onto a GCE as a conductive platform for the developed aptasensor. Next, a peptide bond was formed between the –COOH and -NH_2 groups of the cMWCNTs and the 5'- Amino C6 end of the aptamer, respectively, by EDC coupling, where the C6 chain served as both an anchor and spacer to allow for mobility of the ssDNA. Consequently, the binding of AFB1 to the aptamer facilitated electron transfer through its 3'-MB azide end, the analytical response of which was elucidated by indirect sensing through a $[Fe(CN)_6]^{-3/-4}$ redox probe buffer medium using DPV. Finally, DFT was used to propose a reaction scheme by ascertaining the electronic properties of the redox-active functional groups of AFB1 to support the experimental anodic response findings of DPV, while molecular docking studies were performed to assess the intermolecular interactions of the AFB1-aptamer conjugate system.

4.1.1) Characterization

4.1.1.1) SpICP-MS

SpICP-MS was employed to determine the PSD of the synthesized Fe_3O_4 NPs (**Figure 4.1a**) used in the construction of the electrochemical sensor. It was found that a mean diameter of approximately d = 20 nm with a PSD of around 10 nm to 50 nm was evaluated. In addition, the shape of the Fe_3O_4 NPs was determined to be spherical, as inferred from the TEM imagery (**Figure 4.1b**). Finally, these findings confirm that the synthesized Fe_3O_4 NPs occur in the nano-size range of 1-100 nm, the properties of which are reported to improve the overall conductive performance of the sensor (Elahi and Rizwan 2021).

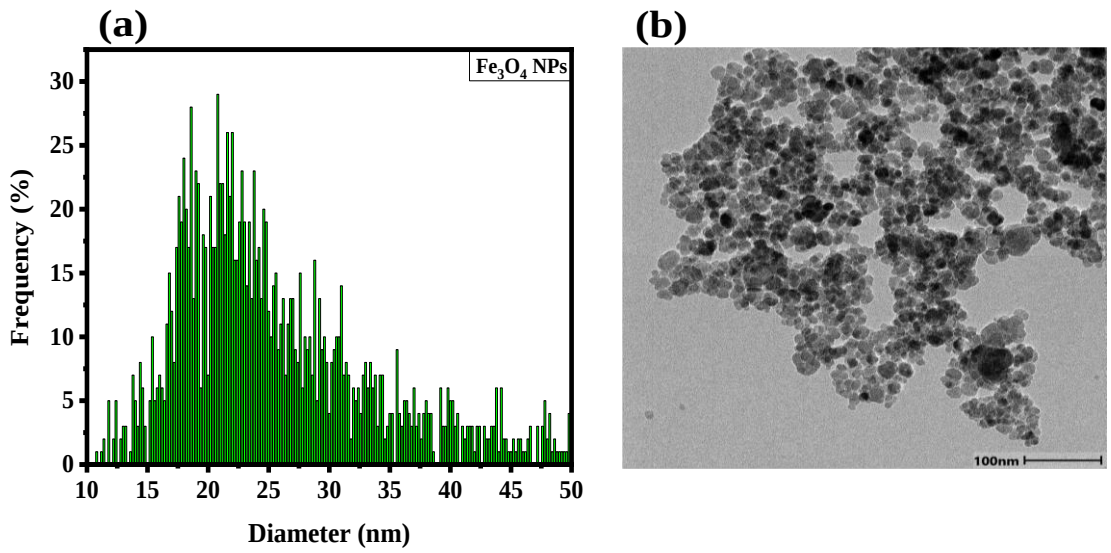

Figure 4.1. (a) SpICP-MS PSD and **(b)** TEM image of synthesized Fe_3O_4 NPs.

4.1.1.2) XRD

The XRD spectra of the Fe_3O_4 NPs, cMWCNTs and the cMWCNTs-Fe_3O_4 NP composite for the structural characterization of the employed electrode materials are represented in **Figure 4.2a**. With regard to Fe_3O_4 NPs, it is observed that the Miller indices for all six peaks (220; 311; 400; 422; 511; 440) are identical to the spectra depicted in reported literature (Zheng *et al.* 2006; El Ghandoor *et al.* 2012; Wei *et al.* 2012). On the other hand, for cMWCNTs, its spectrum exhibiting a distinguished broad peak (002) followed by a smaller, sharp one (100) is also characteristic and similar to reports from other studies (Abdullah and Zulkepli 2015; Kumar *et al.* 2016; Sen *et al.* 2016). In terms of the nanocomposite, the reduced intensity of the characteristic peaks of Fe_3O_4 NP confirms the presence of an interaction with cMWCNTs, while the characteristic peak of the cMWCNTs (002) is observed to have been suppressed in the spectra. Consequently, as the cMWCNT-Fe_3O_4 NP composite is prepared in a mass ratio of 3: Fe_3O_4 NPs to 1: cMWCNTs, it is found that the Fe_3O_4 NP spectra significantly mask those obtained by cMWCNTs in the mixture. Finally, the crystalline sizes of Fe_3O_4 NP, cMWCNTs and cMWCNTs-Fe_3O_4 NP were calculated to be 14.86 nm, 2.46 nm and 14.12 nm, respectively, from their XRD peaks of maximum intensity using the Debye-Scherrer equation **(Eq. (2.7))**. These findings confirm the primarily crystalline nature of the nanomaterials used in the construction of the electrochemical sensor.

4.1.1.3) EDS and SEM

In **Figure 4.2b**, the EDS spectra show the different types of elements that make up the electrode nanomaterials. For the Fe_3O_4 NPs, the significant presence of Fe and O atoms is representative of their primary chemical constituents. On the other hand, the minor indications of Cl and C would originate from precursor salts and trace impurities encountered during synthesis. In reference to cMWCNTs, the significant prevalence of C confirms its composition, while that of O would infer the presence of carboxyl groups. Finally, the composite nature of cMWCNTs-Fe_3O_4 NP is denoted by its spectrum depicting counts of Fe in addition to the C and O atoms similarly observed for cMWCNTs. These results confirm the successful synthesis of the nanocomposite employed for electrode modification.

The SEM imagery depicting the morphologies of the Fe_3O_4 NPs, cMWCNTs and cMWCNTs-Fe_3O_4 NP electrode materials is represented in **Figure 4.2c-e**. **Figure 4.2c** shows the spherical geometry of agglomerated Fe_3O_4 NPs, as confirmed by the aforementioned TEM image (**Figure 4.1b)**, while the nanotube structures of cMWCNTs are revealed in **Figure 4.2d**. Finally, the intercalation of cMWCNTs with Fe_3O_4 NPs is depicted in **Figure 4.2e** for the cMWCNTs-Fe_3O_4 NP nanocomposite.

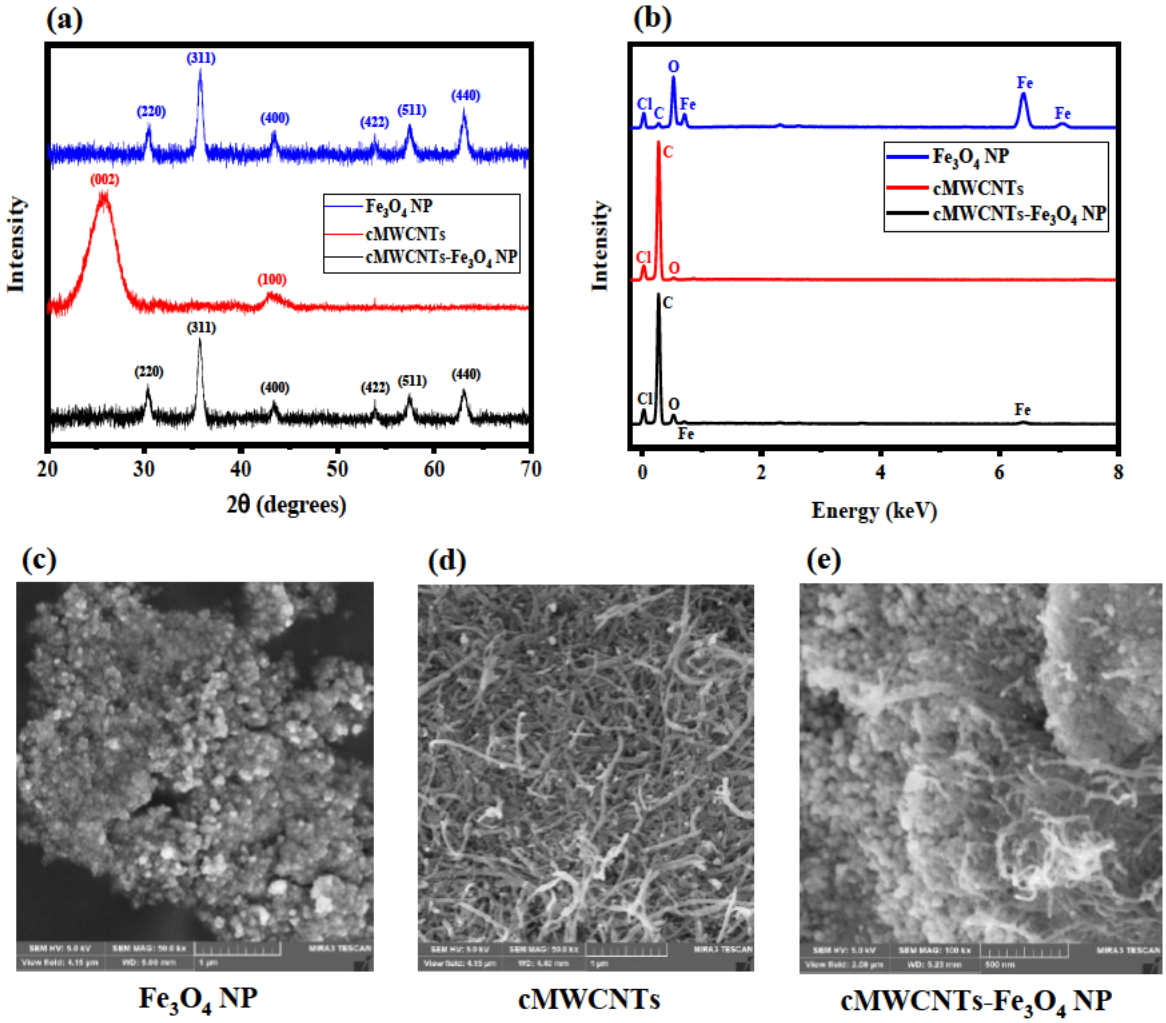

Figure 4.2. (a) XRD **(b)** EDS and SEM **(c, d** and **e)** for Fe_3O_4 NP, cMWCNTs and cMWCNTs-Fe_3O_4 NP.

4.1.2) Electrochemical analyses

4.1.2.1) Electrochemical properties of bare and modified electrodes

The charge transfer capabilities of the modified electrodes were investigated in a layer-by-layer sequence in 1 mM $[Fe(CN)_6]^{3-/4-}$ redox probe solution, employing CV at a scan rate of 0.025 V s^{-1}, and EIS from a frequency of 100 kHz to 0.1 Hz at a fixed applied potential of 0.2 V, respectively **(Figure 4.3)**.

From the CV analysis **(Figure 4.3a)**, it is observed that the GCE (i_{pa} = 4.5 μA) and GCE/Fe_3O_4 NP (i_{pa} = 5.5 μA) layers exhibit a relatively small anodic current response to the electrochemical redox probe. On the other hand, the signal strength goes up almost 10-fold for GCE/cMWCNTs (i_{pa} = 51.0 μA), with a further rise in current observed for the

GCE/cMWCNTs-Fe_3O_4 NP (i_{pa} = 58.0 μA) layer. This may emanate from the intercalated superparamagnetic Fe_3O_4 NPs inducing an electrostatic field within the cMWCNTs, resulting in the strong conductivity exhibited by the cMWCNTs-Fe_3O_4 NP composite (Al-Bagawi, Bayoumy and Ibrahim 2020). The addition of the aptamer further improved the conductivity for the subsequent GCE/cMWCNTs-Fe_3O_4 NP/Apt (i_{pa} = 68.8 μA) electrode; this can be attributed to the peptide bond formation between the carboxyl groups of the cMWCNTs and the amine groups from the amino-C6 linker (5') of the aptamer, facilitating stronger electrode anchorage and enhanced electron transfer. The active surface area, A (cm^2), was determined for each electrode layer using the Randles-Sevcik equation (**Eq. (2.4)**). The trends in terms of increase in A were observed as follows: GCE (4.084×10^{-5} cm^2) < GCE/Fe_3O_4 NP (4.992×10^{-5} cm^2) < GCE/cMWCNTs (4.629×10^{-4} cm^2) < GCE/cMWCNTs-Fe_3O_4 NP (5.264×10^{-4} cm^2) < GCE/cMWCNTs-Fe_3O_4 NP/Apt (6.245×10^{-4} cm^2).

The Nyquist plot for the EIS analysis, based on the data fitting of the respective Randles equivalent circuits (**Figures 4.3c-d**), is shown in **Figure 4.3b**. For the GCE and GCE/Fe_3O_4 NP layers, a semi-circle is depicted, indicative of the electron transfer rate between the electrode and redox probe being slower than the bulk diffusion rate of the electrolyte solution (kinetic control). In addition, at the end of the semi-circle, a 45° straight line is observed, representative of the prevalence of the aforementioned electrolyte bulk diffusion rate (diffusion control). The kinetic control can be explained by the presence of a double-layer charge barrier in-between the electrode and redox probe media, while the diffusion control is representative of Warburg impedance. On the other hand, with regard to the Nyquist plot of the GCE/cMWCNTs layer, a drastic overall suppression in impedance is noted. This can be attributed to the innately strong conductivity of the cMWCNTs, which facilitates an even quicker electron transfer response. This depressed impedance trend is further extended upon the addition of the Fe_3O_4 NPs and subsequently the aptamer for the GCE/cMWCNTs-Fe_3O_4 NP and GCE/cMWCNTs-Fe_3O_4 NP/Apt electrodes, respectively. The χ^2 and corresponding % error (< 100%) values of the circuit parameters (**Table 4.1**) validate the successful fitting of the impedance data. The decrease in electron transfer resistance (R_{ct}) values from GCE to GCE/cMWCNTs-Fe_3O_4 NP/Apt (**Table 4.1**) supports the trend-wise improvement in electron transfer, which directly corresponds to the increase in anodic signal response reported in the CV analysis. Thus, the GCE/cMWCNTs-Fe_3O_4 NP/Apt layer was selected for further AFB1 method optimization because it had the strongest anodic current response.

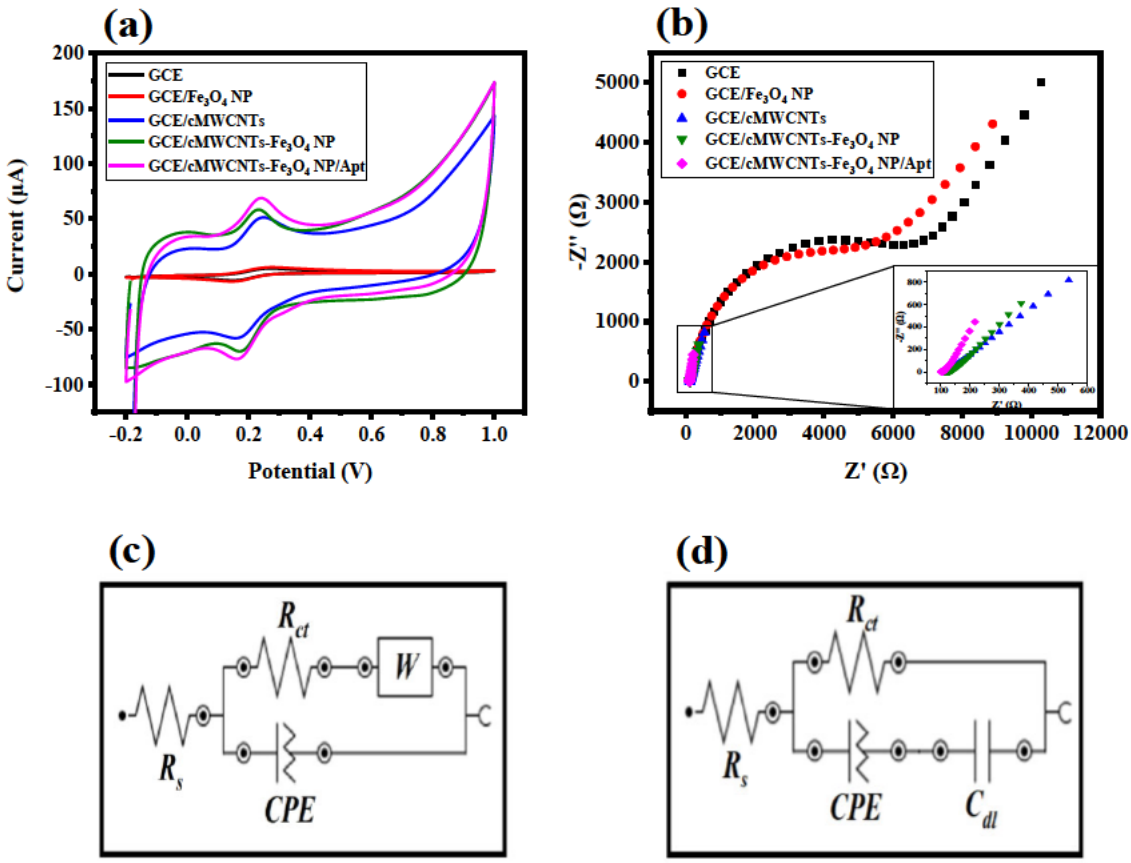

Figure 4.3. Overlay of layer-by-layer electrode characterization by **(a)** CV at 0.025 V s^{-1} and **(b)** EIS from 100 kHz to 0.1 Hz using 1 mM $[Fe(CN)_6]^{3-/4-}$ solution. Randles equivalent circuits of **(c)** GCE and GCE/Fe_3O_4 NP *[R([RW]Q)]* **(d)** GCE/cMWCNTs, GCE/cMWCNTs-Fe_3O_4 NP and GCE/cMWCNTs-Fe_3O_4 NP/Apt *[R(R[QC])]*.

Table 4.1. EIS equivalent circuit data of GCE/cMWCNTs-Fe_3O_4 NP/Apt electrode using 1 mM $[Fe(CN)_6]^{3-/4-}$ solution.

Electrode	R_s (kΩ) (%Error)	R_{ct} (kΩ) (%Error)	χ^2
GCE	0.142 (1.40)	5.602 (2.80)	0.15
GCE/Fe_3O_4 NP	0.143 (1.34)	4.790 (3.05)	0.15
GCE/cMWCNTs	0.117 (0.76)	3.931 (32.29)	0.09
GCE/cMWCNTs-Fe_3O_4 NP	0.111 (1.54)	2.794 (16.33)	0.11
GCE/cMWCNTs-Fe_3O_4 NP/Apt	0.105 (0.64)	1.205 (39.71)	0.08

4.1.2.2) Scan rate variation of developed aptasensor

The CV (**Figure 4.4a**) was used to investigate how the scan rate (0.01 V s^{-1} to 0.10 V s^{-1}) affected the response of 1 mM $[Fe(CN)_6]^{3-/4}$ at the GCE/cMWCNTs-Fe_3O_4 NP/Apt layer. **Figure 4.4b** shows a linear relationship between the peak currents (i_p) and square roots of scan rates ($\upsilon^{1/2}$) with a regression of $R^2 = 0.9992$, suggesting a diffusion-controlled redox process.

In addition, the *log* $_{ip}$ vs. *log* υ graph (**Figure 4.4c**) deduced a similar conclusion, with a slope of 0.604 close to the theoretical value of 0.5 (Thomas *et al.* 2015). Finally, the number of electrons transferred (n) as well as the transport coefficient (α) were evaluated to be 1 and 0.67, respectively, from the E_p vs. *log* υ graph in **Figure 4.4d** using **Eq. (2.2)** and **Eq. (2.3)**.

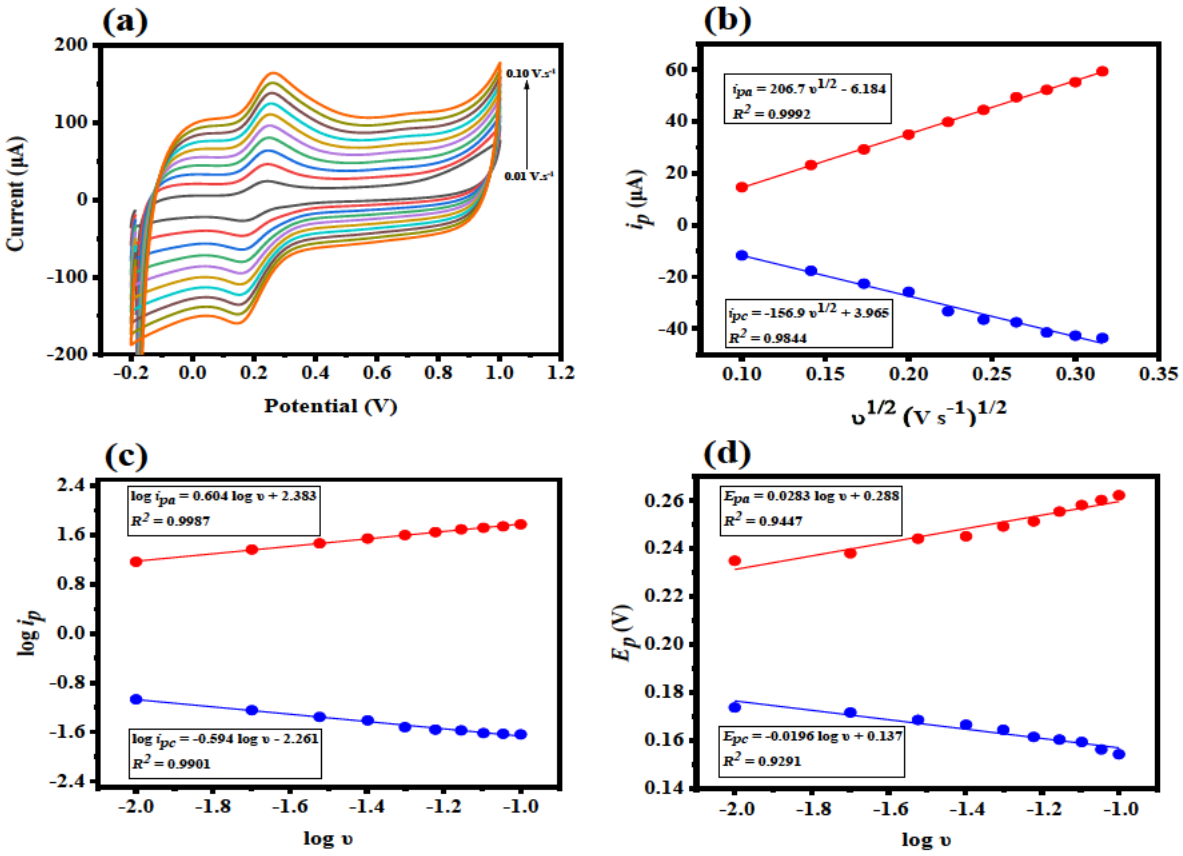

Figure 4.4. (a) Cyclic voltammogram overlay **(b)** i_p vs $\upsilon^{1/2}$ **(c)** *log* $_{ip}$ vs *log* υ **(d)** E_p vs *log* υ of scan rate optimization (0.01 V s^{-1} to 0.10 V s^{-1}) of GCE/cMWCNTs-Fe_3O_4 NP/Apt electrode in 1 mM $[Fe(CN)_6]^{3-/4-}$ solution.

4.1.2.3) Optimization of experimental conditions

The sensitivity of a sensor to its target species is significantly dependent on experimental parameters such as the analyte concentration, deposition voltage and deposition time. Subsequently, these conditions for AFB1 detection were optimized using CV and DPV, respectively, on the selected GCE/cMWCNTs-Fe_3O_4 NP/Apt electrode layer.

Firstly, a fixed concentration of the AFB1 standard was required for subsequent optimization studies. To determine this, a working range from 0.10 fg mL^{-1} to 0.10 ng mL^{-1} AFB1 in 1 mM

$[Fe(CN)_6]^{-3/-4}$ solution was employed (**Figure 4.5**). The concentration selected was 0.10 fg mL^{-1}, where the potential of interest was 0.2 V for the anodic peak. Thereafter, the deposition time (0 s to 60 s) and deposition voltage (-1.4 V to 0.2 V) parameters were similarly optimized to ascertain the most sensitive analytical response for the above 0.10 fg mL^{-1} AFB1 standard using DPV. The maximum anodic responses were attained at DT = 60 s and DV = -0.8 V (**Figures 4.6a-b**), with these parameters subsequently selected for further analysis.

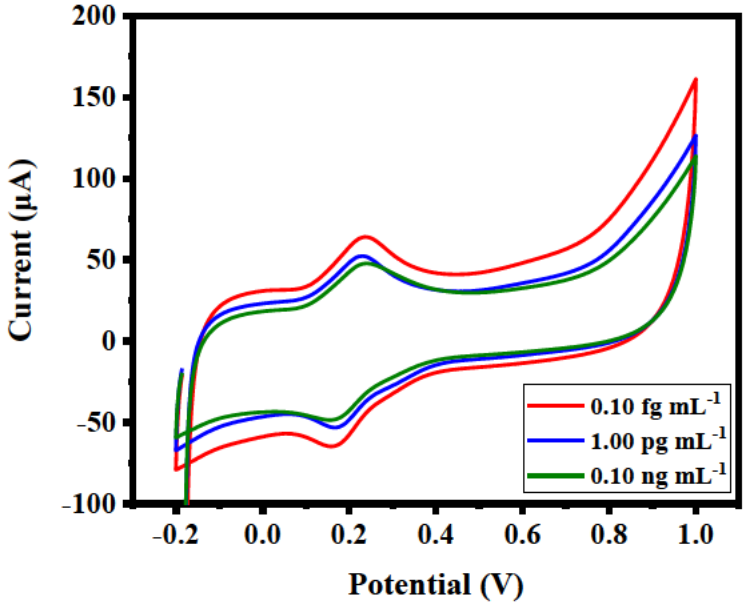

Figure 4.5. Cyclic voltammograms of concentration optimization (0.10 fg mL^{-1} to 0.10 ng mL^{-1}) of AFB1 using GCE/cMWCNTs-Fe_3O_4 NP/Apt electrode in 1 mM $[Fe(CN)_6]^{3-/4-}$ solution.

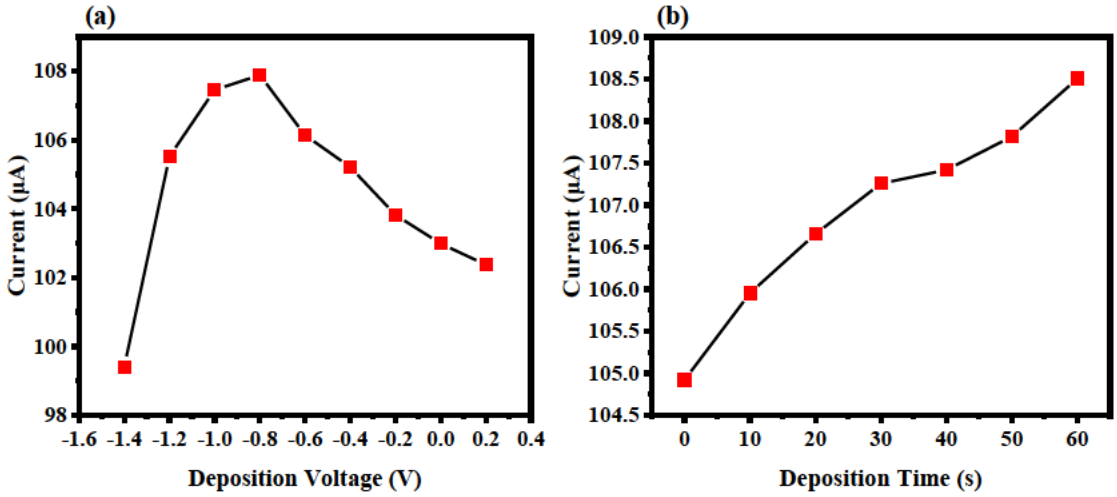

Figure 4.6. Line graphs of **(a)** deposition voltage optimization and **(b)** deposition time optimization for DPV of 0.10 fg mL^{-1} AFB1 using GCE/cMWCNTs-Fe_3O_4 NP/Apt electrode in 1 mM $[Fe(CN)_6]^{3-/4-}$ solution.

4.1.2.4) Evaluation of AFB1 analytical performance of developed aptasensor

The analytical performance of the developed GCE/cMWCNTs-Fe_3O_4 NP/Apt sensor was tested using DPV to see how well it could measure AFB1 indirectly in a 1 mM $[Fe(CN)_6]^{-3/-4}$ solution. **Figure 4.7a** shows the calibration curve plotted in the quadratic analytical response (Raposo and Barceló 2021). It ranged from 0.50 fg mL^{-1} to 5.00 fg mL^{-1} (E_p = 0.0 V to 0.4 V). The anodic peak was found to exhibit suppression in direct relation to the change in concentration of the AFB1 analyte added to the buffer, elucidating a sensitive response and consequently a depressed slope in the calibration curve in **Figure 4.7b** (i_{pa} (µA) = 0.4031 $[AFB1]^2$ – 4.0263 [AFB1] + 94.526, R^2 = 0.9979). This response can be attributed to the conjugative interaction of the aptamer with the AFB1 analyte. In addition, the concentration of "free-moving" aptamers is decreased upon the addition of AFB1; these deductions are expanded upon in the computational section. The LOD and LOQ were determined to be 0.43 fg mL^{-1} and 1.44 fg mL^{-1} using **Eqs. (4.1)** and **(4.2)** (Hloma, Uwaya and Bisetty 2022), respectively. A comparison to other aptasensors in the current literature regarding AFB1 detection is detailed in **Table 4.2**.

$$\text{LOD} = \frac{3 \times \text{Standard Deviation}}{\text{Slope}} \tag{4.1}$$

$$\text{LOQ} = \frac{10 \times \text{Standard Deviation}}{\text{Slope}} \tag{4.2}$$

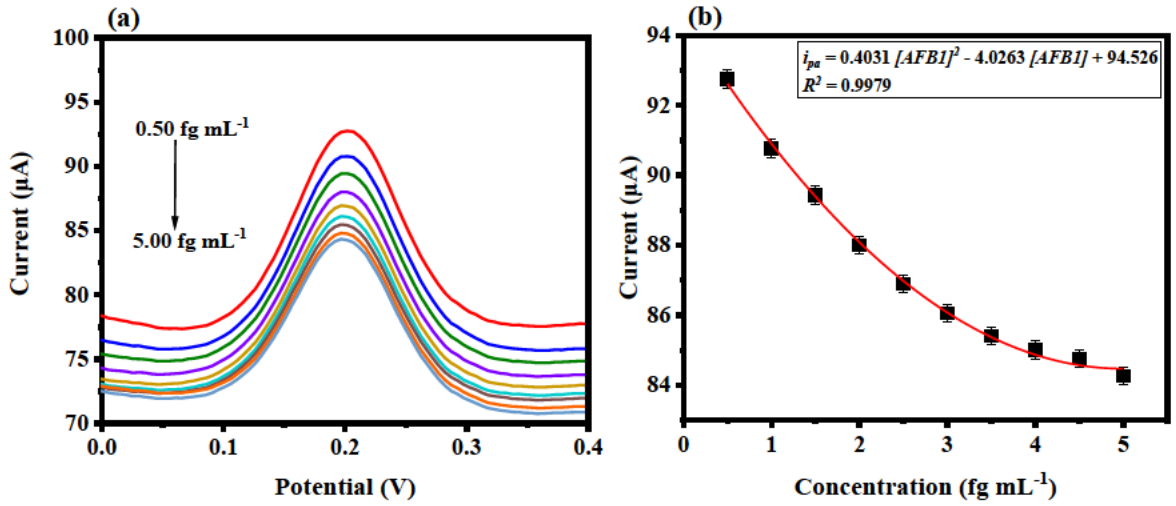

Figure 4.7. (a) DPVs (n = 3) of GCE/cMWCNTs-Fe_3O_4 NP/Apt electrode with increasing concentrations of AFB1 (0.50 fg mL^{-1} to 5.00 fg mL^{-1}) prepared in 1 mM $[Fe(CN)_6]^{3-/4-}$ solution and **(b)** calibration curve of corresponding oxidation peak currents plotted against AFB1 concentrations.

Table 4.2. Comparison of the analytical performance of developed sensor with other aptasensors for AFB1 detection.

Analyte	Detection Strategy	Scheme	LOD	Reference
AFB1	SERS	MNP@Ag-PEI-Apt-Cy5	0.45 pg mL^{-1}	(He *et al.* 2023)
	Fluorescence	MB-dsDNA	0.36 ng mL^{-1}	(Zhan *et al.* 2023)
	Fluorescence	GO/AuNPs/Apt	0.10 pg mL^{-1}	(Dadmehr *et al.* 2023)
	Electrochemistry	Thi-rGO/CS/Apt-cDNA	0.33 pg mL^{-1}	(Lv *et al.* 2023)
	SERS	AuNP dimers/Mxenes/Apt	0.60 pg mL^{-1}	(Wu *et al.* 2022)
	Electrochemistry	**GCE/cMWCNTs-Fe_3O_4 NP/Apt**	**0.43 fg mL^{-1}**	**Current work**

4.1.2.5) Real sample analysis

In order to assess the practicality of the developed aptasensor with regard to real samples, spike recoveries of the AFB1 analyte were determined at different concentrations in corn flour and rice flour by indirection quantification as above by the standard addition method. The overall AFB1 percentage recoveries in both products were excellent in the range of 95% to 105%, with low percentage relative standard deviations (%RSD $<$ 10%) also noted, as per **Table 4.3**.

Table 4.3. Recoveries of AFB1 in real samples using developed aptasensor (n = 3).

Sample	Spiked (fg mL^{-1})	Found (fg mL^{-1})	%Recovery	%RSD
Corn flour	0.50	0.47	95.18	1.71
	1.00	1.05	104.84	1.55
	1.50	1.48	98.39	0.55
Rice flour	0.50	0.49	99.88	0.46
	1.00	1.01	101.41	3.15
	1.50	1.47	97.96	7.48

4.1.2.6) Reproducibility, repeatability, storage stability and interference studies

With regard to the reproducibility study, five identically modified electrodes denoted a %RSD of 8.01% (**Figure 4.8a**). On the other hand, for the repeatability study using a single electrode (n = 5), the %RSD was reported to be 0.17%. In terms of storage stability (electrodes stored at 4℃), the analysis revealed a decrease of 1.21% in anodic current after the second week and

4.73% after the third, where the study was conducted three times over a period of 21 days. Finally, an interference study was conducted using DPV where the analytical detection of AFB1 was determined to be dominant over the presence of ZEN and OTA in the same concentrations (0.10 fg mL^{-1} ZEN, OTA and AFB1 in 1 mM $[Fe(CN)_6]^{-3/-4}$ solution) (**Figure 4.8b**). The slight drop in current response for the mixture could be attributed to minor oxidations of ZEN and OTA at peak potentials close to that of AFB1.

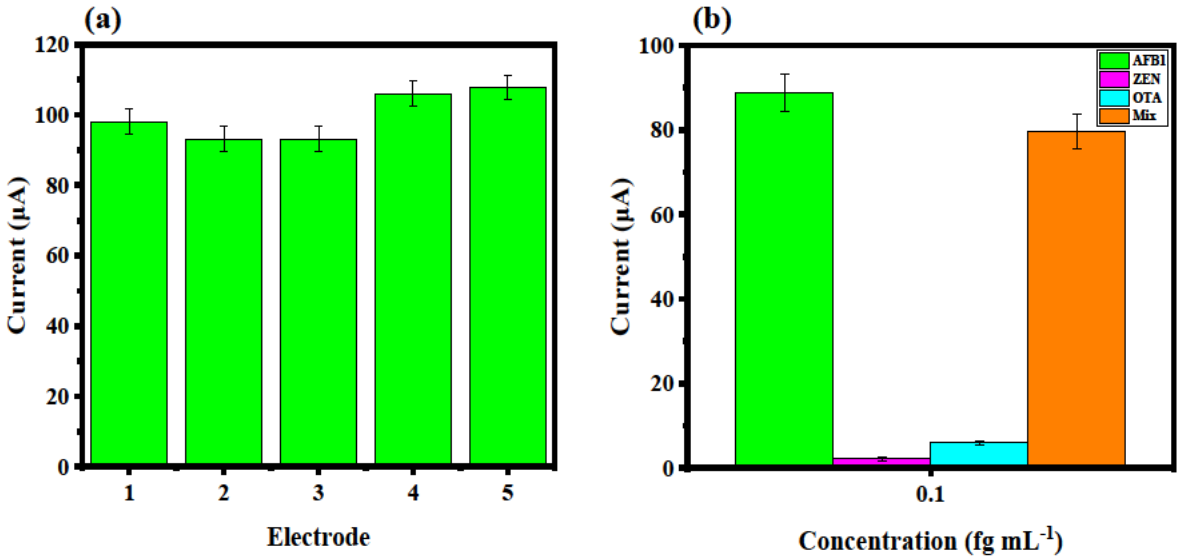

Figure 4.8. (a) Bar graph of reproducibility study **(n = 3)** for DPV of 0.10 fg mL^{-1} AFB1 prepared 1 mM $[Fe(CN)_6]^{3-/4-}$ solution with different **(1-5)** GCE/cMWCNTs-Fe_3O_4 NP/Apt electrodes **(b)** Bar graph of DPV interference study **(n = 3)** of AFB1 in the presence of ZEN and OTA of the same concentration (0.10 fg mL^{-1}).

4.1.3) Computational analyses

4.1.3.1) DFT

Figure 4.9 shows the DFT calculation of the molecular locations of prominent HOMO-LUMO interactions to find possible redox interaction sites of AFB1 in acetonitrile and gaseous form.

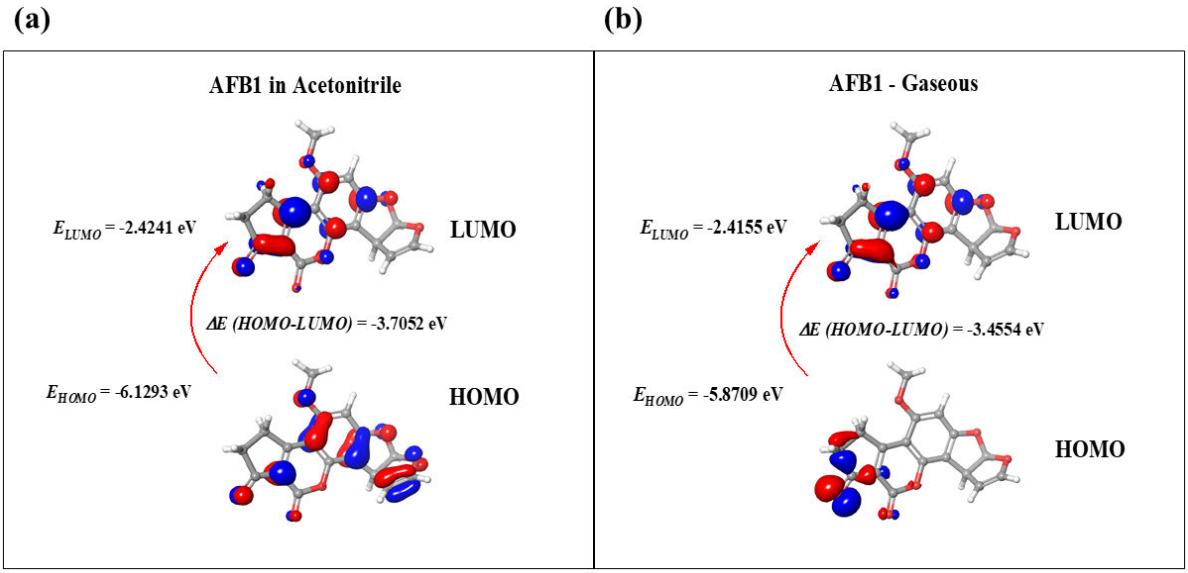

Figure 4.9. HOMO-LUMO depictions of AFB1 in **(a)** acetonitrile and **(b)** gaseous media as determined using DFT (B3LYP/6-31G**).

With regard to the HOMO states, it is observed that when activated by the presence of acetonitrile, the AFB1 terminal furan 8,9 double bond becomes susceptible to electron transfer (**Figure 4.9a**), as opposed to the gaseous form (**Figure 4.9b**), where the absence of electron cloud lobes is noted. Further, with both the LUMO states very similar, the simulation predicts that the overall transfer of electrons is facilitated through resonance π orbital bonding within the aromatic rings and alkene bonds of AFB1. The closeness and negativity of the HOMO-LUMO band gap energy value for AFB1 in acetonitrile, in comparison to the gaseous phase, support the energetically favourable redox reaction occurring. Lastly, a proposed reaction scheme based on the electron transfer from AFB1 in acetonitrile to the MB azide redox probe at the terminal 3' position of the aptamer, in accordance with the experimental voltammetry findings, is depicted in **Figure 4.10**.

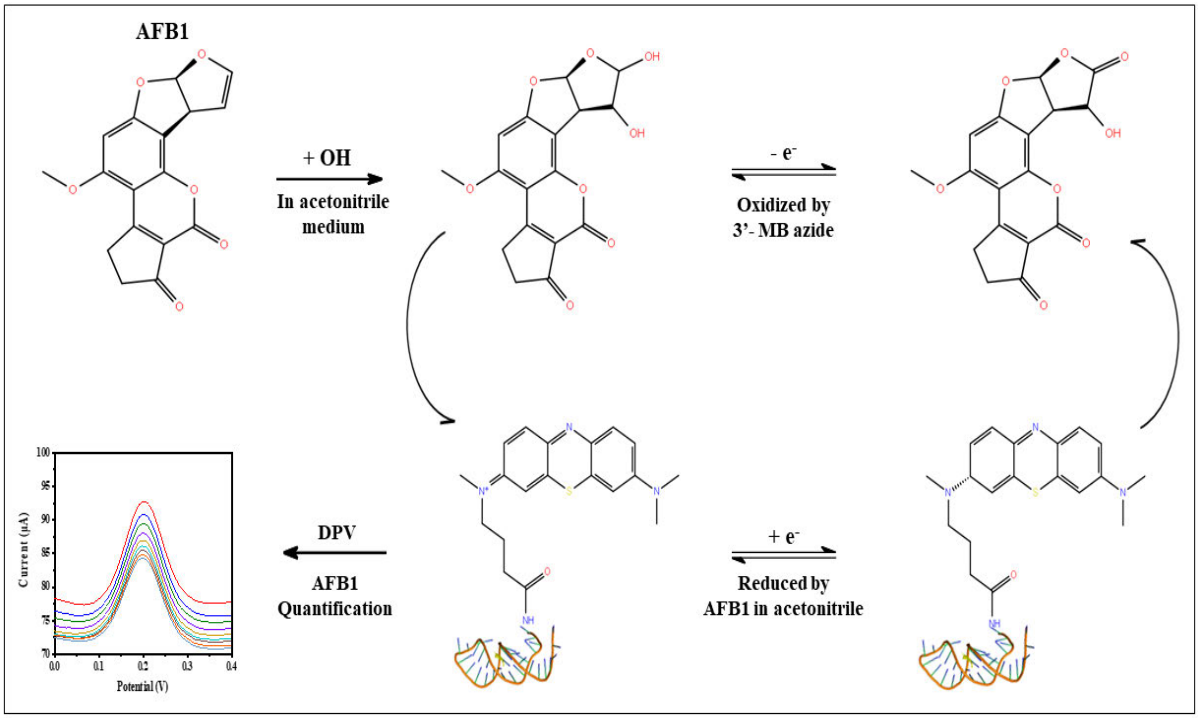

Figure 4.10. Proposed redox reaction scheme of AFB1 in acetonitrile with aptamer for DPV sensing.

4.1.3.2) Molecular docking

Molecular docking was used to ascertain the direct interaction between the 5'- Amino C6-TGGGGTTTTGGTGGCGGGTGGTGTACGGGCGAGGG-MB azide-3' aptamer and the AFB1 analyte. Several combinations of the aptamer and AFB1 were simulated, with the configuration having the highest absolute binding affinity (**Appendix 3, Appendix 4**) being selected for interpretation, as depicted in **Figure 4.11**.

From the insert, it is observed that the prominent modes of affinity stem between the cytosine (C) and guanine (G) bases of the aptamer and the aromatic rings, O and H atoms, from AFB1, respectively. In addition, it is clear that H bonds, together with π interactions, form the basis of the AFB1-aptamer conjugation. Practically, it can be suggested that it is the motion of the aptamer from "free-moving" to "constrained" upon the capture of AFB1 that inhibits the rate of the transfer of electrons. This can be suggested to explain the decrease in current signal response occurring upon fixed additions of AFB1 in the DPV quantitative study (**Figure 4.7**).

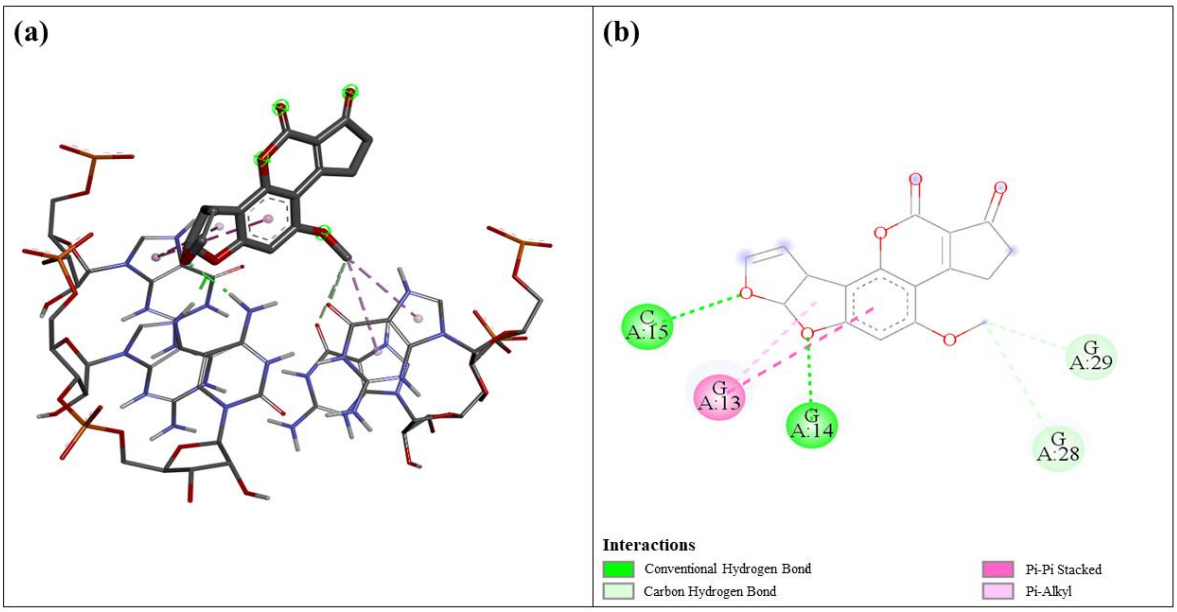

Figure 4.11. A 3D **(a)** and 2D **(b)** representation of the binding of AFB1-aptamer interactions.

4.1.4) Conclusion

A sensitive analytical range was exhibited by the GCE/cMWCNTs-Fe_3O_4 NP/Apt sensor, with low LOD and LOQ values reported (0.43 fg mL^{-1} and 1.44 fg mL^{-1}, respectively). The developed aptasensor was used to detect AFB1 in real samples, exhibiting excellent spike recoveries (95% to 105%) for corn and rice flour. The nano-scaled size of the Fe_3O_4 NPs ($d \approx$ 20 nm) was confirmed by spICP-MS to ensure the enhancement of electrode conductivity for sensor construction. DFT computations predicted that the 8,9-furan ring was the most active site for electron transfer for the proposed AFB1 redox reaction mechanism with the MB tag of the aptamer. Molecular docking simulations inferred that the capture of AFB1 by the aptamer suppressed the anodic current response observed experimentally after each analyte addition in DPV analysis. Finally, the employment of Fe_3O_4 NPs with cMWCNTs has been deduced to enhance aptamer immobilization and the overall electrochemical sensor performance for AFB1 detection.

4.2) Case Study II – A novel electrochemical sensor for the detection of zearalenone in food matrices using PEGylated Fe_3O_4 NPs supported by multidetector AF4 and *in-silico* studies

The previous case study focused on the development of an aptasensor for the detection of AFB1. But in this study, an electrochemical sensor was developed incorporating a nanocomposite that uses the core-shell properties of the synthesized PEG-Fe_3O_4 NPs to its advantage by trapping the ZEN between the entangled polymeric chains that wrap around the spherical Fe_3O_4 NPs. Further, the superparamagnetic properties of the nano-sized Fe_3O_4 NPs bolstered by their $Fe^{2+/3+}$ states, induce an electrostatic field that attracts the ZEN, promoting a higher electron transfer in DPV sensing. Finally, the incorporation of PEG as a binding agent for ZEN detection was viewed as a cheaper alternative to current biomarkers while maintaining analyte sensitivity.

4.2.1) Characterization

4.2.1.1) Multidetector AF4

The PSD of the synthesized PEG-Fe_3O_4 NPs was determined using multidetector AF4, with the measurement of the radius of gyration (r_g) determined by employing the MALS detector at 19 angles (MALS 12° to 164°). In reference to **Figure 4.12**, a clear separation between the void (t_r = 6 min) and sample peak (t_r = 20 min) is noted. In addition, a population of particles within a single peak is eluted. With regard to the characterization of the NPs, it is observed that a PSD of r_g = 10 nm to 60 nm is obtained together with an average r_g at peak height (t_r = 20 min) of 31 $\pm$ 1 nm (n = 3), with spherical geometry elucidated (**Appendix 5**). The AF4-UV (λ = 405 nm) recovery of the PEG-Fe_3O_4 NPs was acceptable (**Appendix 6**) as per the ISO/TS 21362:2018 standard guidelines (ISO 2018), with an average of 86 $\pm$ 4% (n = 3). These findings confirm that the synthesized PEG-Fe_3O_4 NPs occur in the nano-size range of below 100 nm.

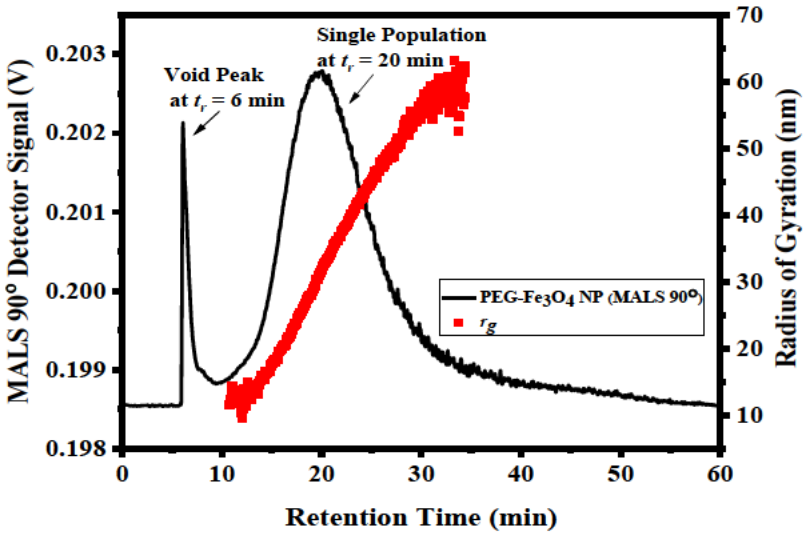

Figure 4.12. AF4-MALS fractogram over MALS 90° for PEG-Fe_3O_4 NP suspension. The red dots display the calculated radius of gyration (r_g) distribution across the eluting peak.

4.2.1.2) FTIR

The functional groups present in PEG-Fe_3O_4 NP, cMWCNTs and PEG-Fe_3O_4 NP/cMWCNTs were evaluated based on their vibrational spectroscopic properties as per FTIR (**Figure 4.13a**). It is observed that for all three layers, vibrational peaks are prevalent at 1020-1275 cm^{-1} which can be attributed to C-O stretching, while C=C stretching is indicated at peaks around 1450-1600 cm^{-1}. The cMWCNTs and PEG-Fe_3O_4 NP/cMWCNTs spectra revealed sharp peaks around 1780 cm^{-1} assigned to C=O, while minor peaks present in the range around 3000-3400 cm^{-1} denoted O-H stretching. The presence of carboxylic groups on PEG-Fe_3O_4 NP/cMWCNTs thus confirms the successful preparation of the nanocomposite.

4.2.1.3) EDS and SEM

Figure 4.13b depicts the EDS spectra showing the qualitative elemental compositions of the developed electrode nanomaterials. From the data for PEG-Fe_3O_4 NP, the high prevalence of Fe and O is expected considering the particles' constituents. The presence of Cl and S in the PEG-Fe_3O_4 NP spectrum would stem from precursor salts used in synthesis, while that of C would originate from PEG. Regarding cMWCNTs, the dominant count of C confirms its composition, with O present from the aforementioned carboxyl groups and Cl present as a small trace impurity. The PEG-Fe_3O_4 NP/cMWCNTs spectrum is similar to that of PEG-Fe_3O_4

NP, with a key difference being an increased count of C in comparison to Fe, attributed to the 3:1 cMWCNTs:PEG-Fe_3O_4 NP mass ratio employed in the synthesis of the nanocomposite.

The morphologies of the nanomaterials (PEG-Fe_3O_4 NP, cMWCNTs and PEG-Fe_3O_4 NP/cMWCNTs) were investigated using SEM (**Figure 4.13c-e**). **Figure 4.13c** shows spherically shaped PEG-Fe_3O_4 NPs in agreement with the AF4-MALS sphere fit (**Appendix 5**), while the micrograph of cMWCNTs (**Figure 4.13d**) revealed agglomeration of intertangled nanotube structures. Finally, the PEG-Fe_3O_4 NP/cMWCNTs nanocomposite image depicted in **Figure 4.13e** shows the interaction of PEG-Fe_3O_4 NPs with cMWCNTs.

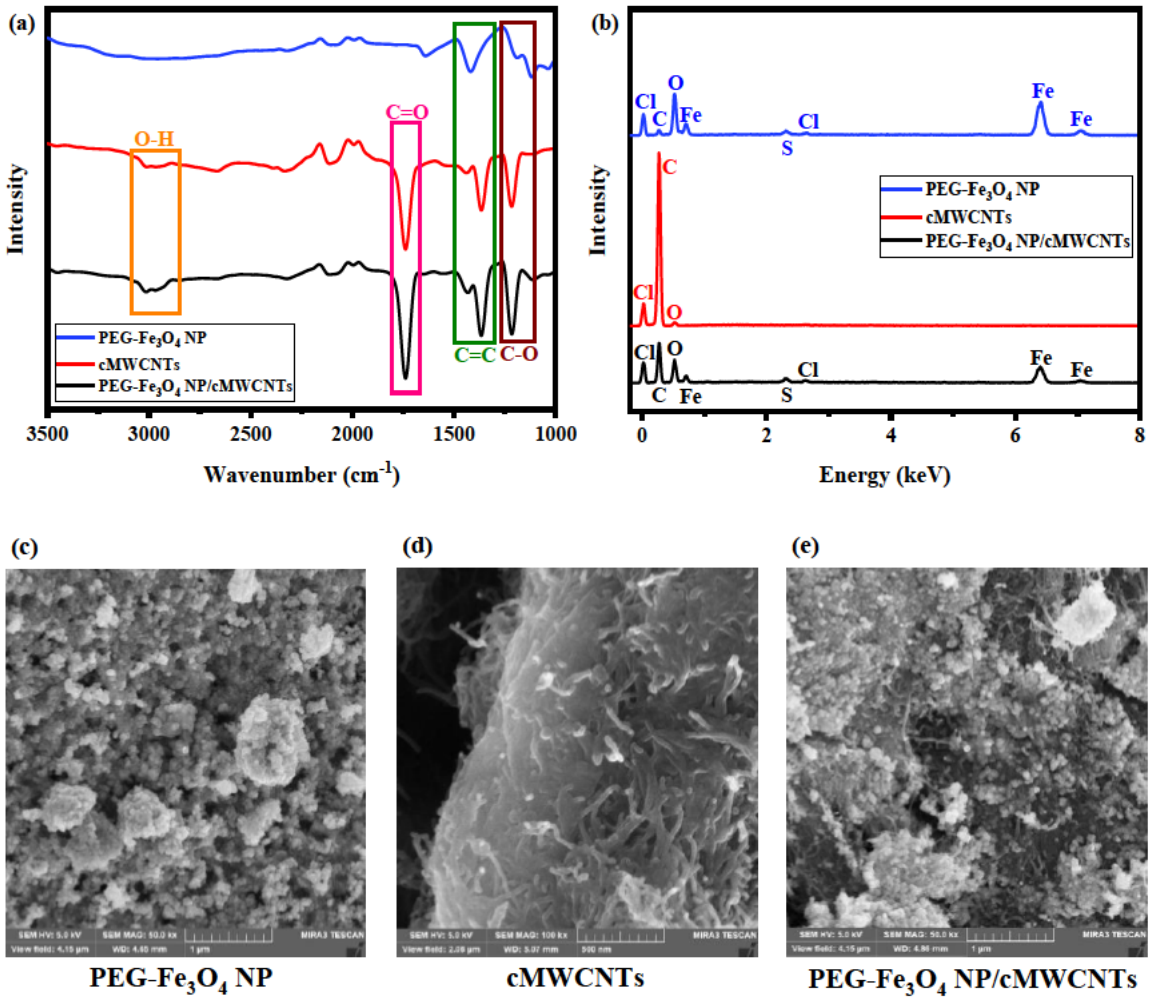

Figure 4.13. (a) FTIR **(b)** EDS and SEM **(c, d** and **e)** for PEG-Fe_3O_4 NP, cMWCNTs and PEG-Fe_3O_4 NP/cMWCNTs.

4.2.2) Electrochemical analyses

4.2.2.1) Electrode characterization using redox probe

The charge transfer capabilities of the employed bare and modified GCEs were assessed using CV at a scan rate of 0.025 V s^{-1}, and EIS at a fixed applied potential of 0.2 V, in 1 mM $[Fe(CN)_6]^{3-/4-}$ solution (**Figure 4.14a-b**).

In **Figure 4.14a**, it is observed that both the bare GCE (i_{pc} = -4.6 μA) and GCE/PEG-Fe_3O_4 NP (i_{pc} = -5.2 μA) electrode layers appear to have suppressed the overall electrochemical responses in their reaction paths. On the other hand, a six-fold current increase is reported for GCE/cMWCNTs (i_{pc} = -28.2 μA). The GCE/PEG-Fe_3O_4 NP/cMWCNTs electrode layer shows a further rise in current response (i_{pc} = -40.9 μA). This trend can be attributed to the presence of carboxyl groups on the surface of the cMWCNTs ends and defect sites (Norizan *et al.* 2020), which facilitate quicker reaction kinetics. In addition, the dispersive properties of PEG allow for the interaction of Fe_3O_4 NPs with cMWCNTs, thus merging the conductive abilities of these nanomaterials. For each electrode layer, the area surface coverage, A (cm^2), was evaluated using the Randles-Sevcik equation (**Eq. (2.4)**) for freely diffusing electrode-adsorbed redox species at 25 ℃. A comparative trend in terms of respective electrode active surface areas for each layer was elucidated, whereby the layer with the highest A facilitated the highest charge transfer due to exhibiting the most contact with the electro-active redox probe species. The trends in increments of A were observed as follows: GCE (4.175×10^{-5} cm^2) < GCE/PEG-Fe_3O_4 NP (4.720×10^{-5} cm^2) < GCE/cMWCNTs (2.560×10^{-4} cm^2) < GCE/PEG-Fe_3O_4 NP/cMWCNTs (3.712×10^{-4} cm^2).

For EIS (**Figure 4.14)**, the Randles equivalent circuits in **Figure 4.14c-d** were used to fit the data to the Nyquist spectra presented in **Figure 4.14b**. The corresponding percentage error (< 100%) and χ^2 values of the circuit parameters (**Table 4.4**) validated the successful fitting of the impedance data. The observed semi-circle arcs (**Figure 4.14b**) are representative of redox species that are under kinetic control, meaning that the rate of the transfer of electrons between the redox probe and the electrode surface is slower than the rate of the bulk diffusion of the electrolyte solution. This can be taken into account by factors indicative of electrode surface imperfections (uneven surface, containing jags, etc.), which are represented by the constant phase element on the Randles circuit (Macdonald and Johnson 2018). The increase in size in the impedance arc from layer GCE to GCE/PEG-Fe_3O_4 NP can be attributed to the PEG coating

slowing down electron flow between the Fe_3O_4 NPs and the GCE electrode surface. Also, competition between the Fe^{2+} and Fe^{3+} ions present in both the redox probe and Fe_3O_4 NPs may increase the presence of an ionic electrode-redox probe interfacial double layer in the electrochemical cell. The increase in R_{ct} values from GCE to GCE/PEG-Fe_3O_4 NP further elucidates this trend (**Table 4.4**), of which the two layers are fitted in *[R([RW]Q)]* Randles equivalent circuits (**Figure 4.14c**). On the other hand, a significant drop in impedance is observed for GCE/cMWCNTs (see insert), which can be explained by the presence of carboxyl groups increasing the dispersibility and hydrophilicity of MWCNTs in polar solvents. An even lower impedance response for GCE/PEG-Fe_3O_4 NP/cMWCNTs can be attributed to PEG, together with the aforementioned carboxyl groups of the cMWCNTs, facilitating an improved physical mixture of the nanocomposite in terms of the resulting electrode paste material. The corresponding decreased trend in R_{ct} values elucidates this reduction in resistance to charge transfer **(Table 4.4)**. In *[R(R[QC])]* Randles equivalent circuits, the GCE/cMWCNTs and GCE/PEG-Fe_3O_4 NP/cMWCNTs electrode layers were fitted **(Figure 4.14d)**. Consequently, the GCE/PEG-Fe_3O_4 NP/cMWCNTs layer was selected for further optimization having the strongest cathodic current response.

Finally, CV was used to find out how the change in scan rate (0.01 V s^{-1} to 0.10 V s^{-1}) affected the redox peaks of the 1 mM $[Fe(CN)_6]^{3-/4-}$ redox probe solution at the GCE/PEG-Fe_3O_4 NP/cMWCNTs layer (**Figure 4.15a**). **Figure 4.15b** shows that there is a linear relationship between the peak currents (i_p) and square roots of scan rates ($\upsilon^{1/2}$) with R^2 = 0.9927. This suggests that the redox process is diffusion-controlled.

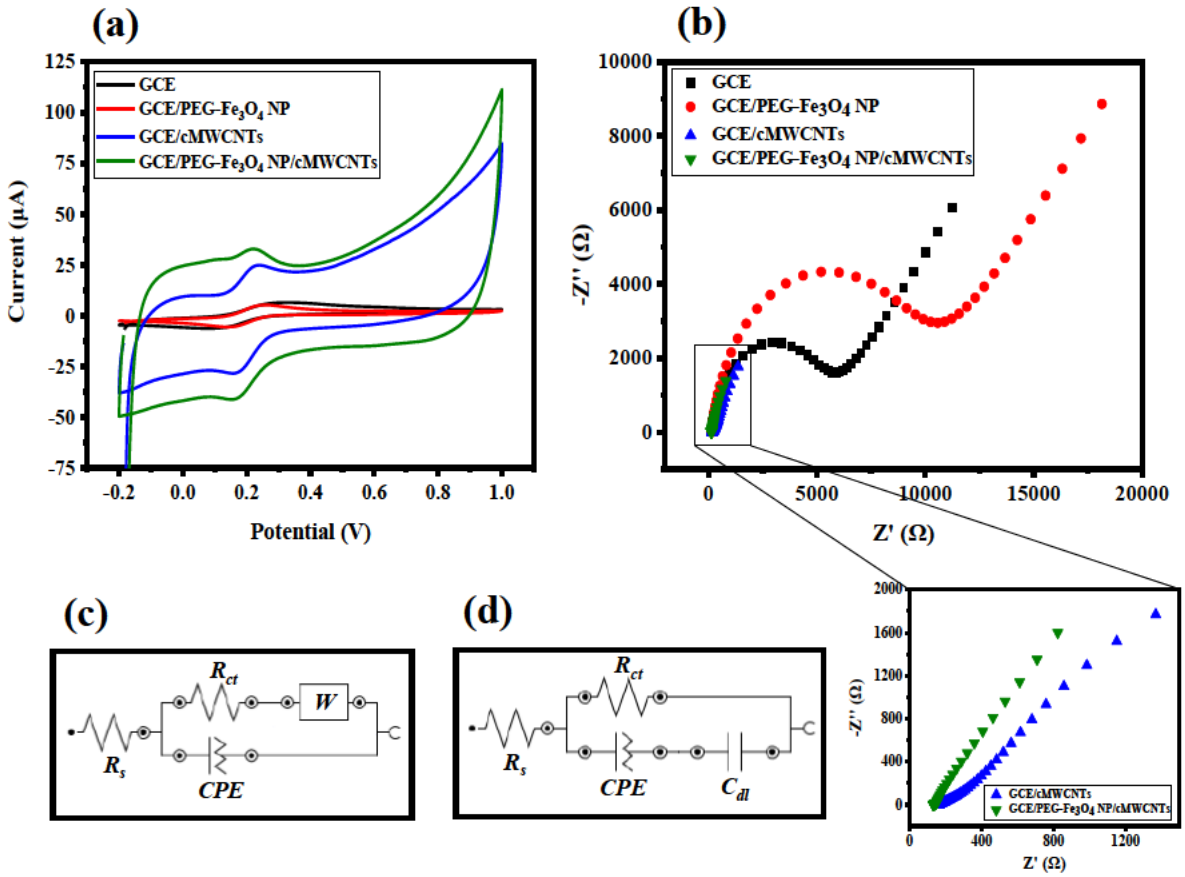

Figure 4.14. Overlay of layer-by-layer electrode characterization by **(a)** CV and **(b)** EIS using 1 mM $[Fe(CN)_6]^{3-/4-}$ solution. Randles equivalent circuits of **(c)** GCE and GCE/PEG-Fe_3O_4 NP *[R([RW]Q)]* **(d)** GCE/cMWCNTs and GCE/PEG-Fe_3O_4 NP/cMWCNTs *[R(R[QC])]*.

Table 4.4. EIS equivalent circuit data of GCE/PEG-Fe_3O_4 NP/cMWCNTs electrode using a 1 mM $[Fe(CN)_6]^{3-/4-}$ solution.

Electrode	R_s (kΩ) (%Error)	R_{ct} (kΩ) (%Error)	χ^2
GCE	0.148 (2.14)	5.175 (2.87)	0.33
GCE/PEG-Fe_3O_4 NP	0.149 (2.23)	9.493 (2.93)	0.33
GCE/cMWCNTs	0.137 (2.23)	0.667 (2.12)	0.12
GCE/PEG-Fe_3O_4 NP/cMWCNTs	0.133 (2.07)	0.606 (1.51)	0.29

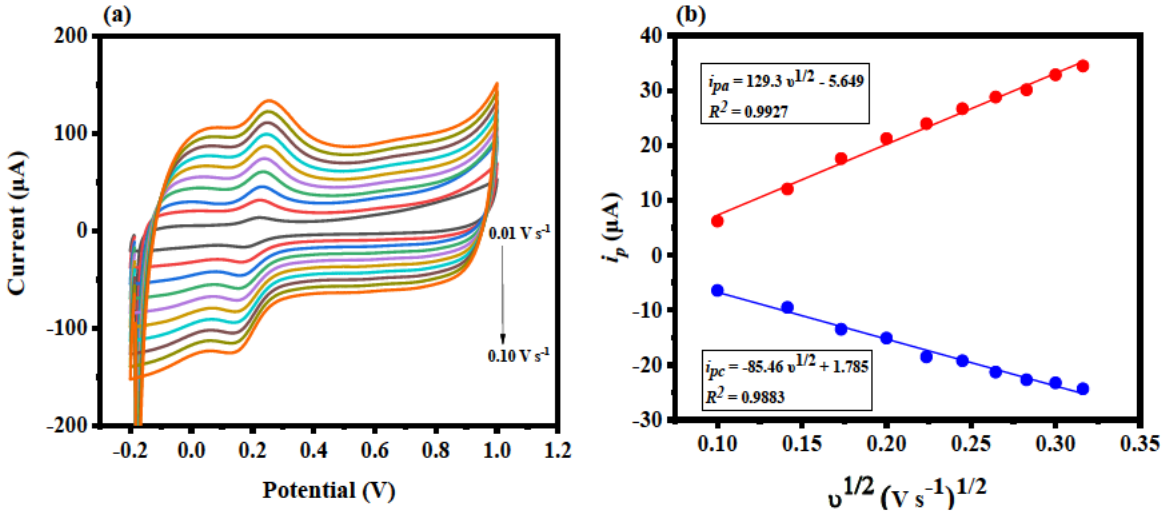

Figure 4.15. (a) Cyclic voltammogram overlay and **(b)** i_p vs $\upsilon^{1/2}$ of scan rate optimization (0.01 V s^{-1} to 0.10 V s^{-1}) of GCE/PEG-Fe_3O_4 NP/cMWCNTs electrode using a 1 mM $[Fe(CN)_6]^{3-/4-}$ solution.

4.2.2.2) Optimization of experimental conditions

The sensitivity of the designed sensor towards the analyte peak is strongly dependent upon certain parameters, including the concentration, supporting electrolyte (buffer), pH of the supporting electrolyte, deposition voltage and deposition time. Thus, these parameters for ZEN detection were optimized using CV and DPV on the GCE/PEG-Fe_3O_4 NP/cMWCNTs electrode layer. Initially, a fixed concentration of ZEN standard was selected for subsequent optimization studies, where a working range from 0.50 ng mL^{-1} to 5.00 ng mL^{-1} ZEN in PBS buffer solution (pH = 7.4) was employed (**Figure 4.16a**). The selected concentration was 0.50 ng mL^{-1} ZEN, with a potential of -0.2 V for the cathodic peak. Thereafter, a buffer optimization was performed using the 0.50 ng mL^{-1} ZEN standard that was prepared in three different buffer solutions, namely PBS, sodium phosphate buffer, and borate buffer, all adjusted to pH 7.4 for physiological medium adaptation of the analyte (**Figure 4.16b**). The best electrochemical response was that from the sodium phosphate buffer (pH 7.4), which was selected for further studies. The next step involved optimizing the pH of the 0.50 ng mL^{-1} ZEN standard prepared in sodium phosphate buffer, where a working pH range (pH 4.0, 6.0, 7.4, and 9.0) to account for an acidic, neutral and basic pH was used. pH 7.4 attained the optimum response and was adopted throughout the study (**Figure 4.17**). Finally, the deposition voltage in the range of 0.2 V to -1.6 V and deposition time (0 s to 60 s) parameters were similarly optimized to ascertain the highest analytical response for the above ZEN standard using DPV. The maximum cathodic

responses were attained at DV = 0.2 V and DT = 60 s (**Figure 4.18a-b**), with these parameters subsequently selected for further experiments.

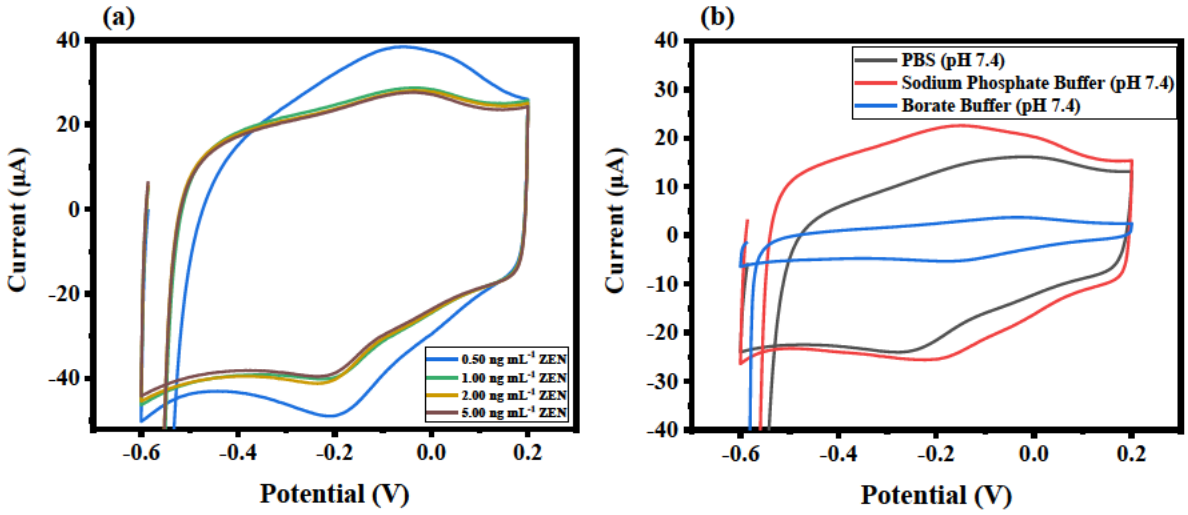

Figure 4.16. Cyclic voltammograms of **(a)** concentration optimization (0.50 ng mL^{-1} to 5.00 ng mL^{-1}) and **(b)** buffer optimization (0.50 ng mL^{-1}) of ZEN using GCE/PEG-Fe_3O_4 NP/cMWCNTs electrode.

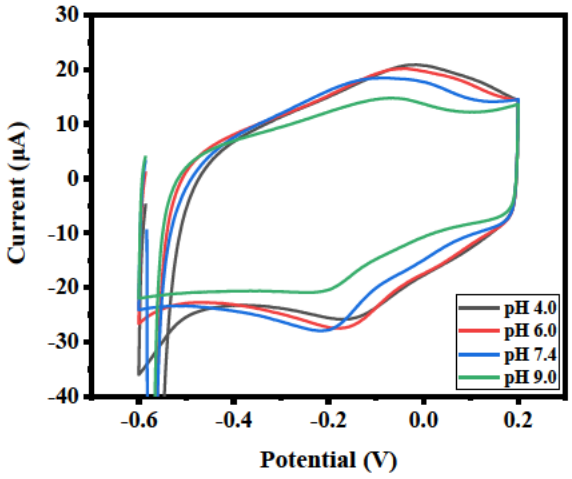

Figure 4.17. Cyclic voltammogram of pH optimization of 0.50 ng mL^{-1} ZEN prepared in sodium phosphate buffer with GCE/PEG-Fe_3O_4 NP/cMWCNTs electrode.

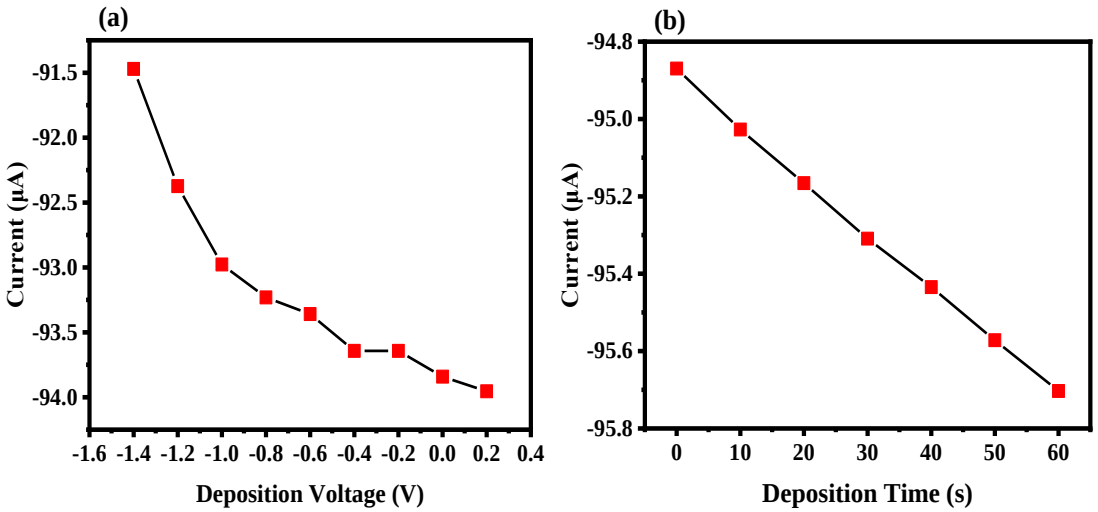

Figure 4.18. Line graphs of **(a)** deposition voltage optimization and **(b)** deposition time optimization for DPV of 0.50 ng mL^{-1} ZEN prepared in sodium phosphate buffer with GCE/PEG-Fe_3O_4 NP/cMWCNTs electrode.

4.2.2.3) Evaluation of electrode performance towards ZEN

The electrochemical performance of the electrodes was assessed for ZEN sensitivity using CV at 0.025 V s^{-1} and EIS (applied potential of -0.2 V) in a 0.50 ng mL^{-1} ZEN solution prepared in sodium phosphate buffer, as shown in **Figure 4.19**.

For CV analysis, in reference to **Figure 4.19a**, for layers GCE and GCE/PEG-Fe_3O_4 NP, it is found that the suppression of current flow occurs due to the lack of any significant analyte response electrochemically. On the other hand, for GCE/cMWCNTs, an improvement in current strength is noted, and a peak is distinguished, especially for the cathodic reaction (E_{pc} = -0.2 V). A further increase in current response is noted for GCE/PEG-Fe_3O_4 NP/cMWCNTs. The magnitudes of cathodic current responses (E_{pc} = -0.2 V) are observed as follows: GCE (-0.16 μA) > GCE/PEG-Fe_3O_4 NP (-0.13 μA) < GCE/cMWCNTs (-18.4 μA) < GCE/PEG-Fe_3O_4 NP/cMWCNTs (-30.0 μA). Consequently, the GCE/PEG-Fe_3O_4 NP/cMWCNTs layer having the response with the highest absolute magnitude was selected for further method development for ZEN analyses.

With regard to the EIS analysis, as depicted in **Figure 4.19b**, the behaviour of GCE and GCE/PEG-Fe_3O_4 NP is supported by the exceedingly arced impedance responses and high R_{ct} values (**Table 4.5**). On the other hand, the relatively small impedance signals obtained for GCE/cMWCNTs and GCE/PEG-Fe_3O_4 NP/cMWCNTs are distinguished in the insert, with an

almost 100-fold decrease in R_{ct} values evaluated in comparison to the first two layers. Consequently, this could be attributed to the electrochemical reduction of the positively charged (methanol-dissolved) ZEN on the electrode surface due to the polarity gradient induced by the negative electrostatic field of PEG-Fe_3O_4 NP together with cMWCNTs, thus facilitating an exchange of electrons at a higher rate. The decrement trend in R_{ct} values elucidates this reduction in resistance to charge transfer **(Table 4.5)**, which supports the increase in conductivity together with the overall charge transfer between the ZEN molecule and the PEG-Fe_3O_4 NP/cMWCNTs composite. All electrode layers were fitted in *[R(R[QC])]* Randles equivalent circuits **(Figure 4.19c)**.

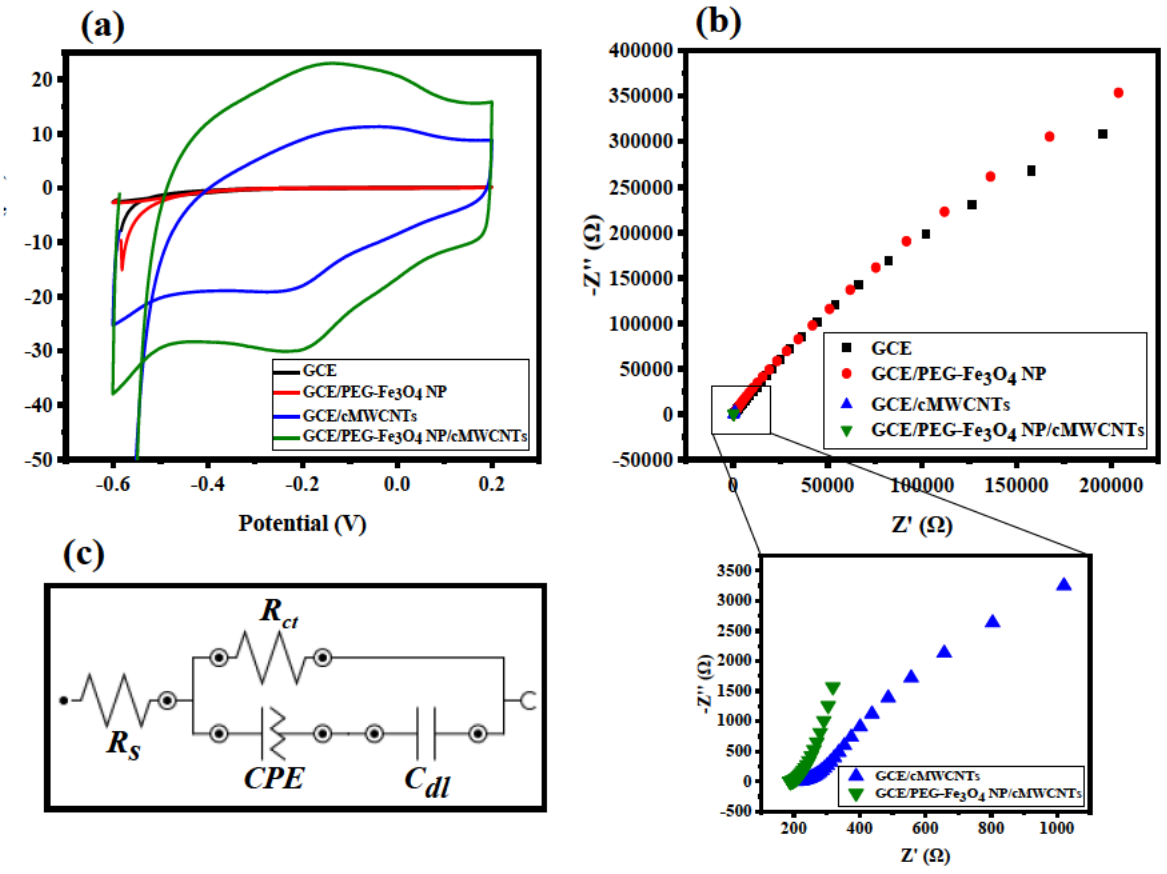

Figure 4.19. Overlay of **(a)** CV and **(b)** EIS for layer-by-layer electrode study of 0.50 ng mL^{-1} ZEN prepared in sodium phosphate buffer. Randles equivalent circuit of **(c)** GCE, GCE/PEG-Fe_3O_4 NP, GCE/cMWCNTs and GCE/PEG-Fe_3O_4 NP/cMWCNTs *[R(R[QC])]*.

Table 4.5. EIS equivalent circuit data of GCE/PEG-Fe_3O_4 NP/cMWCNTs electrode using 0.50 ng mL^{-1} ZEN prepared in sodium phosphate buffer.

Electrode	R_s (kΩ) (%Error)	R_{ct} (kΩ) (%Error)	χ^2
GCE	0.221 (1.56)	1532 (1.89)	0.16
GCE/PEG-Fe_3O_4 NP	0.223 (1.68)	1709 (2.58)	0.20
GCE/cMWCNTs	0.206 (1.70)	19.64 (2.41)	0.18
GCE/PEG-Fe_3O_4 NP/cMWCNTs	0.132 (0.927)	6.06 (1.51)	0.12

4.2.2.4) Evaluation of ZEN analytical performance on developed electrode

The GCE/PEG-Fe_3O_4 NP/cMWCNTs sensor's ability to detect ZEN was evaluated using DPV with a calibration curve plotted in a quadratic analytical response range of 1.00 fg mL^{-1} to 10.00 fg mL^{-1} (E_p = -0.4 V to 0.2 V), as depicted in **Figure 4.20**. The cathodic peak was found to exhibit a sensitive response to the change in concentration of the ZEN analyte, consequently in the negative current direction (**Figure 4.20a**), thus elucidating the depressed slope in the calibration curve in **Figure 4.20b** (i_{pc} (μA) = 0.0261 [ZEN]^2 – 0.5171 [ZEN] – 57.203, R^2 = 0.9951). The LOD and LOQ were evaluated to be 0.34 fg mL^{-1} and 1.12 fg mL^{-1} using **Eqs. (4.1)** and **(4.2),** respectively. A comparison to other analytical techniques in terms of ZEN detection is depicted in **Table 4.6**.

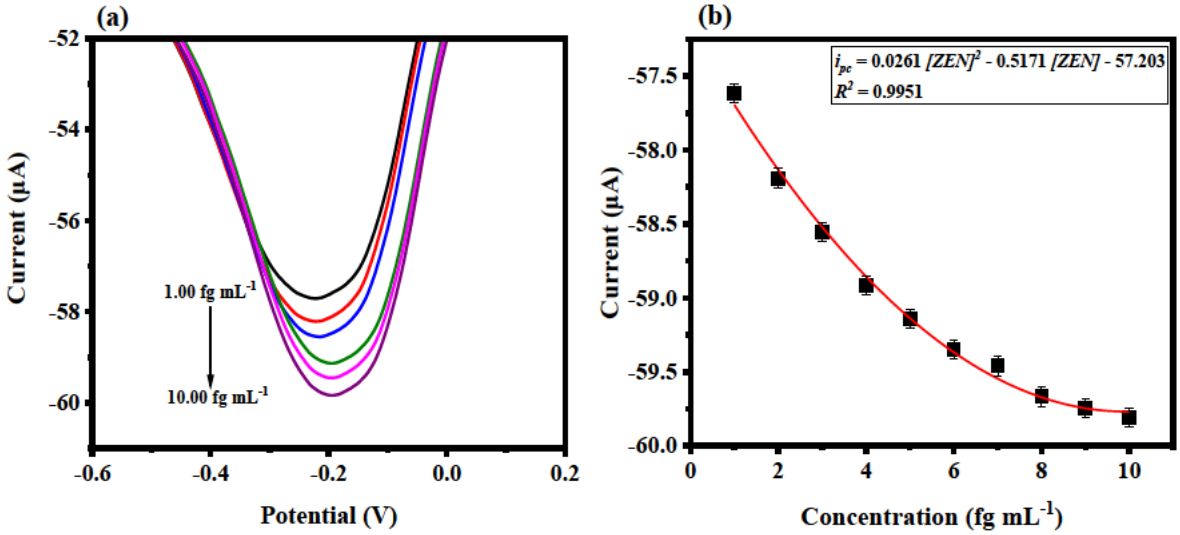

Figure 4.20. (a) DPVs (n = 3) at GCE/PEG-Fe_3O_4 NP/cMWCNTs electrode with increasing concentrations of ZEN (1.00 fg mL^{-1} to 10.00 fg mL^{-1}) prepared in sodium phosphate buffer and **(b)** calibration curve of corresponding reduction peak currents plotted against ZEN concentrations.

Table 4.6. Comparison of the analytical performance of developed sensor with other analytical techniques for ZEN detection.

Analyte	Detection Strategy	LOD	References
Zearalenone	Aptasensor	0.39 pg mL^{-1}	(Chen *et al.* 2022d)
	Immunoassay	0.15 pg mL^{-1}	(Hao *et al.* 2022)
	UHPLC-MS/MS	0.02 ng mL^{-1}	(Li *et al.* 2018a)
	Molecularly imprinted polymer	18.00 ng mL^{-1}	(Du *et al.* 2019)
	DNA tweezer	0.04 ng mL^{-1}	(Chen *et al.* 2022a)
	DPV	**0.34 fg mL^{-1}**	**Current work**

4.2.2.5) Real sample analysis

To assess the real-life applicability of the developed sensor, rice flour and corn flour were analyzed to determine spike recoveries of the ZEN analyte at different concentrations. The overall percentage recoveries for ZEN in both products were excellent in the range of 92% to 106%, with low percentage relative standard deviations (%RSD $<$ 10%) noted as well, as per **Table 4.7**.

Table 4.7. Recoveries of ZEN in real samples using modified electrode (n = 3).

Sample	Spiked (fg mL^{-1})	Found (fg mL^{-1})	%Recovery	%RSD
Rice flour	1.00	0.97	97.35	0.84
	2.00	2.09	104.67	1.15
	3.00	2.89	96.34	0.60
	4.00	4.05	101.18	0.06
Corn flour	1.00	1.05	105.11	5.19
	2.00	1.86	92.95	7.96
	3.00	3.13	104.06	4.35
	4.00	3.96	99.03	1.07

4.2.2.6) Repeatability, reproducibility, storage stability and interference studies

For the repeatability study (n = 5), the %RSD was reported to be 0.61%. In addition, a reproducibility study was undertaken using five different electrodes modified in the same way, with the %RSD for the electrodes reported to be 3.68% (**Figure 4.21a**). In terms of storage stability (electrode stored at 4℃), the analysis was performed three times over a period of 21 days, where the decrease in cathodic current response was noted to be 5.24% after the second week and 6.10% after the third. Finally, an interference study was conducted using DPV

whereby the analytical detection of ZEN was found to be dominant over that of OTA and AFB1 in the same concentrations (0.50 ng mL^{-1} ZEN, OTA and AFB1) in a solution containing all three mycotoxins (**Figure 4.21b**).

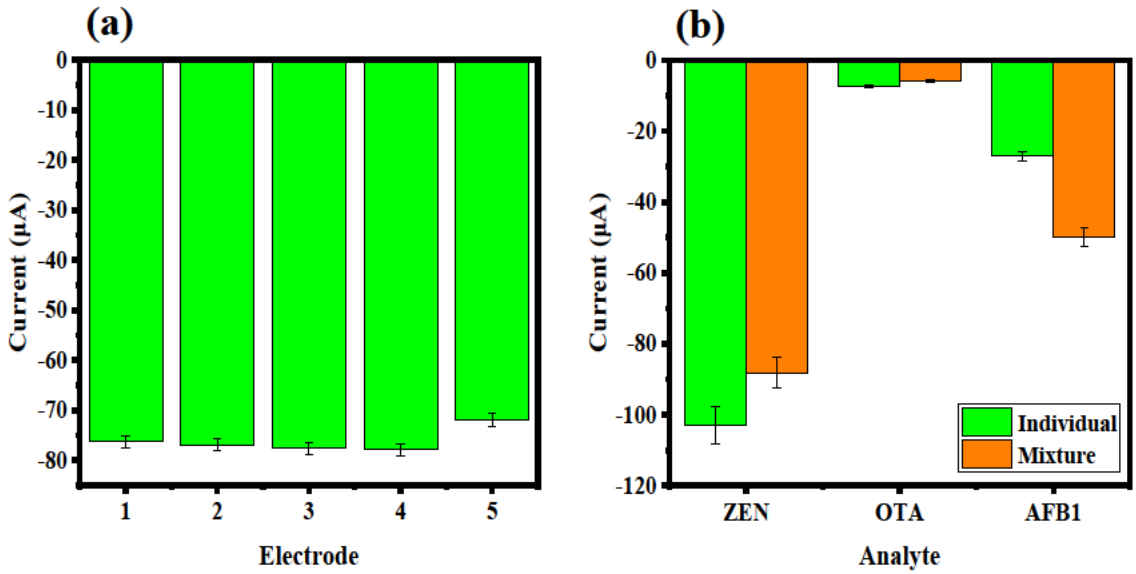

Figure 4.21. (a) Bar graph of reproducibility study (n = 3) for DPV of 0.50 ng mL^{-1} ZEN prepared in sodium phosphate buffer with different **(1-5)** GCE/PEG-Fe_3O_4 NP/cMWCNTs electrodes **(b)** Bar graph of DPV interference study (n = 3) of ZEN in the presence of OTA and AFB1 of the same concentration (0.50 ng mL^{-1}).

4.2.3) Computational analyses

4.2.3.1) MC simulation

The MC simulation allowed for the study of the interaction between the ZEN analyte and the developed electrode under canonical ensemble conditions by energetics. The GCE/PEG-Fe_3O_4 NP/cMWCNTs/ZEN electrode scheme is depicted in **Figure 4.22**, with ZEN highlighted in yellow.

Figure 4.22 shows that ZEN is observed to be in between the PEG chains and the Fe_3O_4 NP, indicative of high analyte adsorption between the two layers. The strongly negative polarity of the latter appealed more to the relatively positive polar field of the analyte; this promotes the ZEN-PEG interaction as the nature of the polymer provides a relatively neutral backbone-oriented potential field. In addition, the Fe_3O_4 NP component, acting as an appropriate "sandwich" layer, provides this strong negative potential field for the system due to the

transitional Fe^{2+}/Fe^{3+} states, which intrinsically facilitate electrophilicity. The GCE acts as a base to support the rest of the layers, with the carboxyl groups from the cMWCNTs providing further energetic potential anchorage.

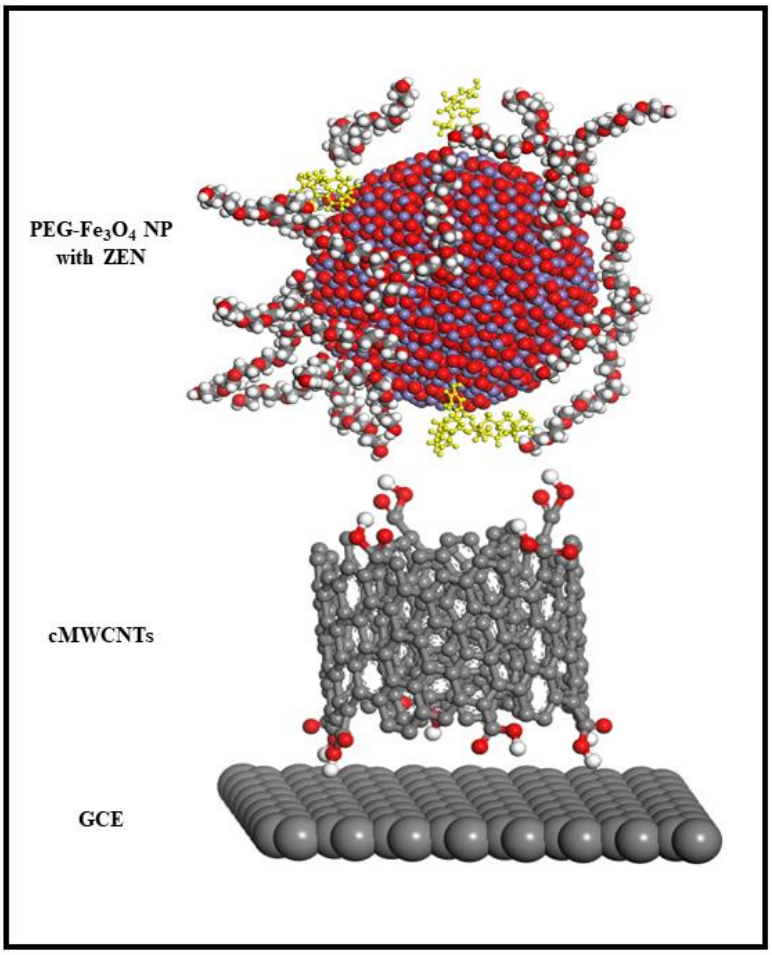

Figure 4.22. Monte Carlo simulation of ZEN (shown in yellow) interacting with GCE/PEG-Fe_3O_4 NP/cMWCNTs electrode scheme.

The energy distribution of the system looks further into ZEN interacting with each component of the electrode. Each electrode layer was treated as a substrate with ZEN as the adsorbate; the energetics are detailed in **Table 4.8**.

A trend is noticed upon the additions of cMWCNTs, Fe_3O_4 NP, and PEG to the GCE base layer with regard to decreasing adsorption energies (**Table 4.8**); this lowering of energy is characteristic of the energetic stabilization (hence adsorption) of the ZEN analyte with the respective electrode layers, indicative of a strong interaction (Naidoo *et al.* 2021; Hloma, Uwaya and Bisetty 2022; Uwaya and Bisetty 2023).

Table 4.8. Energy distribution (kcal mol^{-1}) of ZEN on the layer-by-layer scheme of the GCE/PEG-Fe_3O_4 NP/cMWCNTs electrode.

Substrate	Total Energy	Adsorption Energy	Rigid Adsorption Energy	Deformation Energy
GCE	-46.87	-20.13	-20.33	0.19
GCE/Fe_3O_4 NP	-198.38	-171.65	-220.98	49.34
GCE/PEG-Fe_3O_4 NP	-272.09	-245.35	-307.68	62.33
GCE/PEG-Fe_3O_4 NP/cMWCNTs	-400.93	-374.19	-495.07	120.88

4.2.4) Conclusion

The developed electrochemical sensor exhibited a sensitive analytical range with low LOD and LOQ values reported (0.34 fg mL^{-1} and 1.12 fg mL^{-1}, respectively) along with excellent spike recoveries (92% to 106%) for real sample analysis. The size characterization and distribution of the nano-sized ($r_g \approx 31$ nm) PEG-Fe_3O_4 NPs confirmed by multidetector AF4 contributed to the high charge transfer in DPV sensing of ZEN. Lastly, MC simulations predicted that ZEN interacted the strongest with the GCE/PEG-Fe_3O_4 NP/cMWCNTs electrode scheme, as elucidated by the lowest adsorption energy obtained (E_{Ads} = -374.19 kcal mol^{-1}).

4.3) Case Study III – A nickel MOF-based electrochemical sensor for ochratoxin A detection in food supported by *in-silico* studies

The previous work dealt with the development of an electrochemical sensor for ZEN using PEG as a trapping mechanism with spherically shaped Fe_3O_4 NPs. In this case study, however, an electrochemical sensor incorporating a Ni-MOF with cRGO applied to a GCE was developed (GCE/Ni-MOF/cRGO) for the detection of OTA in foods. Further, the affinity of the network of interconnected functional groups of trimesic acid to OTA allowed for efficient analyte capture into the porous cavity of the MOF. Finally, the conductive properties of the Ni-O metal-oxide clusters in Ni-MOF, together with the core graphitic attributes of cRGO, allowed for improved electron transfer and enhancement of the sensitivity in DPV for OTA analysis.

4.3.1) Characterization

4.3.1.1) FTIR

The FTIR spectra of Ni-MOF, cRGO and the Ni-MOF/cRGO composite depicting their functional groups are represented in **Figure 4.23**. With regard to Ni-MOF, it is observed that a characteristic peak for Ni-O likely present from the Ni(II) precursor salt is obtained at around 1513 cm^{-1}, while C-O and C=C stretching from the trimesic acid organic linker are indicated by peaks around 1204 cm^{-1} and 1353 cm^{-1} respectively. For cRGO, the C=O peak around 1737 cm^{-1} confirms the presence of carboxyl groups. Finally, pertaining to the Ni-MOF/cRGO spectrum, it is elucidated that both the aforementioned Ni-O and C=O characteristic peaks are prevalent in the composite, along with O-H stretching around 3000 cm^{-1} for all three electrode layers. These findings confirm the successful preparation of the nanocomposite used in the construction of the electrochemical sensor.

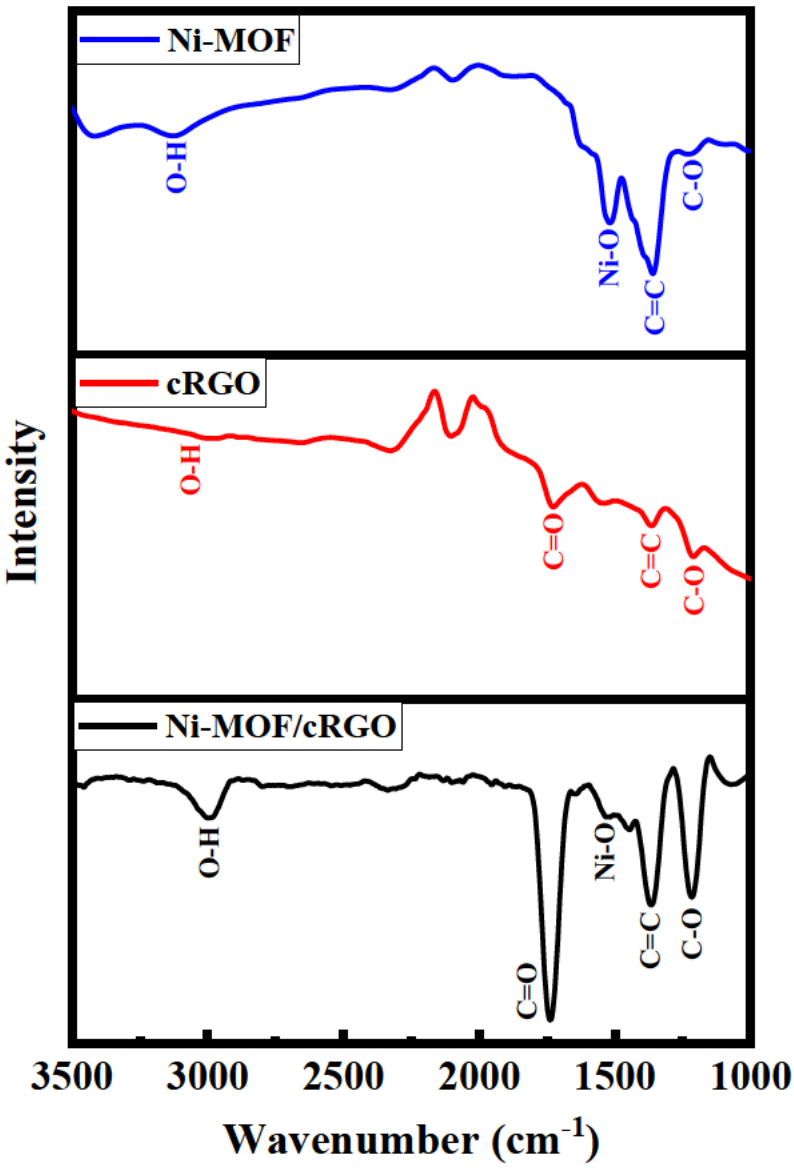

Figure 4.23. FTIR for Ni-MOF, cRGO and Ni-MOF/cRGO.

4.3.1.2) EDS and SEM

Figure 4.24a displays the EDS spectra denoting the precise elemental compositions of the electrode nanomaterials that were used. With regard to Ni-MOF, the indication of Ni is representative of the metallic core of the MOF, while the presence of C and O shows that the trimesic acid linker is made up of organic atomic constituents. For cRGO, on the other hand, the prevalence of C and O elucidates its composition and carboxylation functionalization, with Na indicative of minor trace impurities. Finally, the presence of Ni, in combination with the

increased C intensity count, confirms the structural composite makeup of the Ni-MOF/cRGO layer used in the electrode modification.

The SEM imagery of Ni-MOF, cRGO and Ni-MOF/cRGO showing the morphologies of the electrode materials is represented in **Figure 4.24b-d**. In **Figure 4.24b** for Ni-MOF, rod-like elongated crystals are observed as representative of the MOF structural frame, while for cRGO (**Figure 4.24c**), the graphitic sheets of its structure are revealed. Finally, the layering of Ni-MOF on cRGO is depicted in the image of the Ni-MOF/cRGO nanocomposite in **Figure 4.24d**.

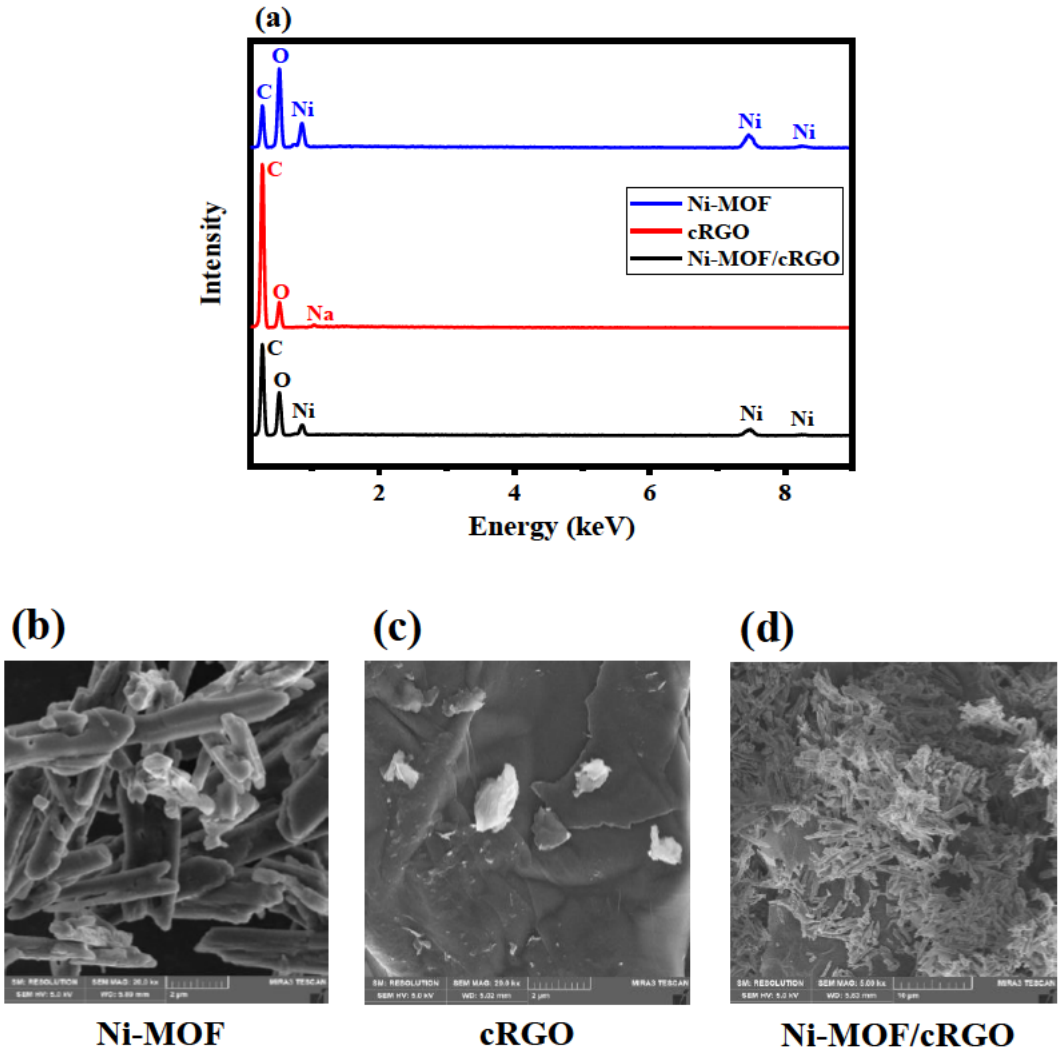

Figure 4.24. (a) EDS and SEM **(b, c** and **d)** for Ni-MOF, cRGO and Ni-MOF/cRGO.

4.3.2) Electrochemical analyses

4.3.2.1) Electrochemical properties of bare and modified electrodes

The charge transfer capabilities of the modified electrodes were investigated in a layer-by-layer sequence using CV at a scan rate of 0.025 V s^{-1}, and EIS at a fixed applied potential of 0.2 V, respectively, in 1 mM $[Fe(CN)_6]^{3-/4-}$ redox probe solution (**Figure 4.25a-b**).

With reference to the CV analysis (**Figure 4.25a**), it is observed that the GCE/Ni-MOF/cRGO (i_{pa} = 27.2 μA) electrode layer anodic current response is multiple factors greater than those of GCE (i_{pa} = 5.2 μA), GCE/Ni-MOF (i_{pa} = 0.2 μA), and GCE/cRGO (i_{pa} = 2.7 μA). In addition, a positive shift in the anodic peak potential value to 0.5 V of this composite layer in comparison to the previous electrodes is noted. These observations can be attributed to the interaction between Ni-MOF and cRGO as a conductive platform, facilitating enhanced electron transfer. The active surface area, A (cm^2), was determined using the Randles-Sevcik equation (**Eq. (2.4)**) for each electrode layer. The trends in terms of increase in A were elucidated as follows: GCE/Ni-MOF (1.815×10^{-6} cm^2) < GCE/cRGO (2.451×10^{-5} cm^2) < GCE (4.720×10^{-5} cm^2) < GCE/Ni-MOF/cRGO (2.469×10^{-4} cm^2).

In terms of EIS, the Randles equivalent circuits in **Figure 4.25c-d** were applied to the Nyquist plots presented in **Figure 4.25b**. It is observed that all electrode layers exhibit some degree of diffusion-controlled redox transfer based on the depiction of roughly 45° straight lines from each plot. With regard to the GCE/Ni-MOF/cRGO electrode, a significant overall suppression in impedance is observed in comparison to the other layers. This is in accordance with the decrease in R_{ct} values obtained (**Table 4.9**), directly corresponding to the increase in current response as reported in the CV analysis. Thus, the GCE/Ni-MOF/cRGO layer was selected for further optimization because it had the strongest anodic current response.

Finally, the influence of scan rate variation (0.01 V s^{-1} to 0.10 V s^{-1}) on the response of 1 mM $[Fe(CN)_6]^{3-/4-}$ solution applying the GCE/Ni-MOF/cRGO electrode was determined using CV (**Figure 4.26a**). In addition, a linear relationship between the peak currents (i_p) and square roots of scan rates ($\upsilon^{1/2}$) with a regression of R^2 = 0.9929 was denoted (**Figure 4.26b**), suggesting a diffusion-controlled redox process; this is in agreement with the findings discussed in EIS.

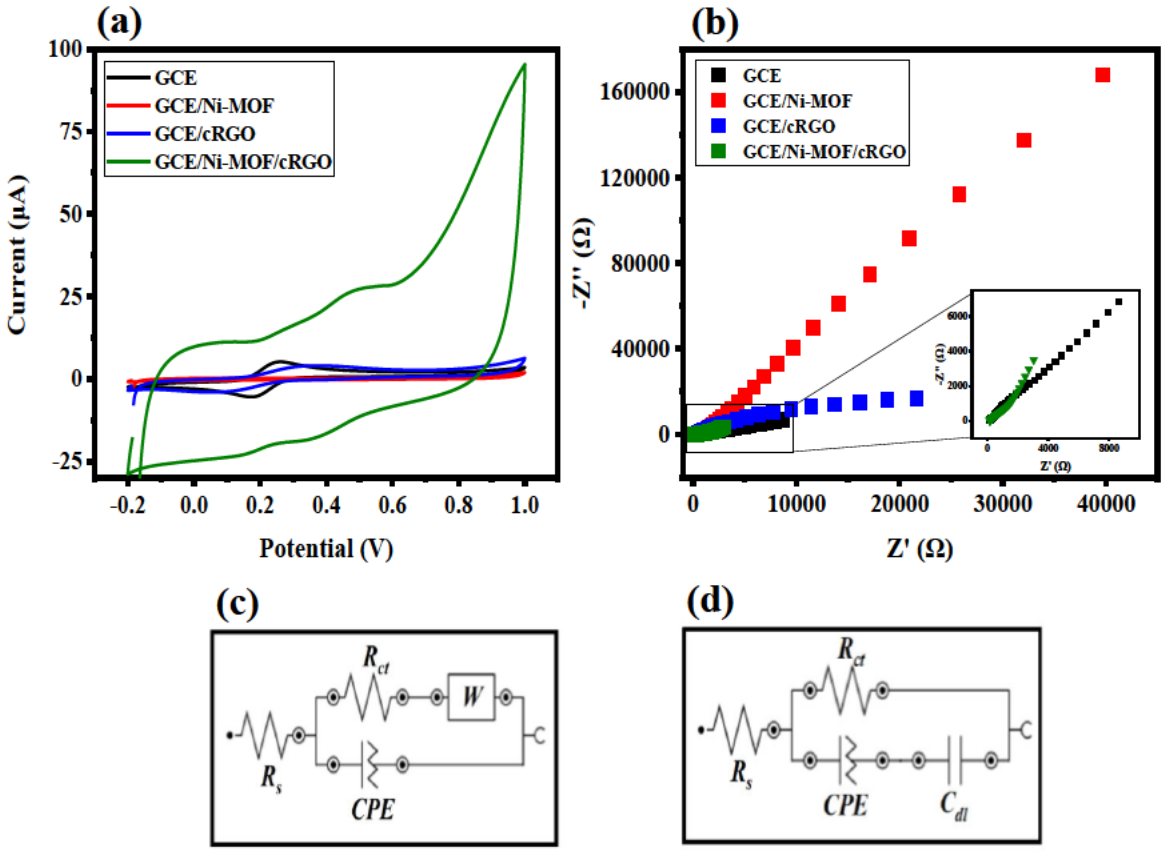

Figure 4.25. Overlay of layer-by-layer electrode characterization by **(a)** CV and **(b)** EIS using 1 mM $[Fe(CN)_6]^{3-/4-}$ solution. Randles equivalent circuits of **(c)** GCE and GCE/Ni-MOF *[R([RW]Q)]* **(d)** GCE/cRGO and GCE/Ni-MOF/cRGO *[R(R[QC])]*.

Table 4.9. EIS equivalent circuit data of GCE/Ni-MOF/cRGO electrode using a 1 mM $[Fe(CN)_6]^{3-/4-}$ solution.

Electrode	R_s (kΩ) (%Error)	R_{ct} (kΩ) (%Error)	χ^2
GCE	0.157 (2.36)	16.06 (28.71)	0.11
GCE/Ni-MOF	0.141 (2.47)	44.01 (19.41)	0.25
GCE/cRGO	0.199 (1.62)	26.10 (5.75)	0.21
GCE/Ni-MOF/cRGO	0.168 (1.94)	4.86 (16.11)	0.15

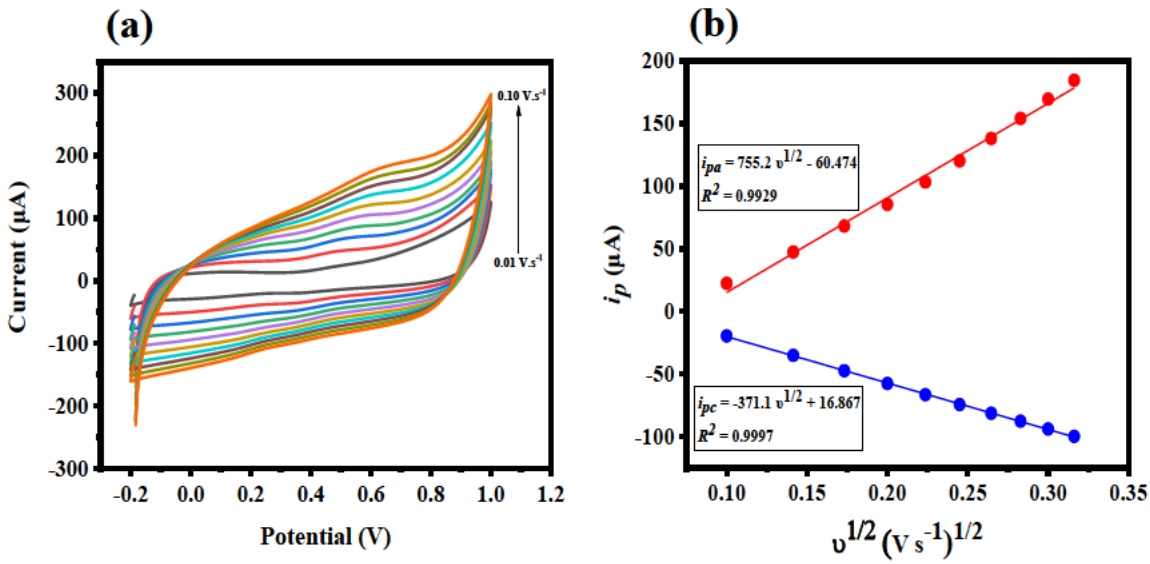

Figure 4.26. (a) Cyclic voltammogram overlay and **(b)** i_p vs $\upsilon^{1/2}$ of scan rate optimization (0.01 V s^{-1} to 0.10 V s^{-1}) of GCE/Ni-MOF/cRGO electrode using 1 mM $[Fe(CN)_6]^{3-/4-}$ solution.

4.3.2.2) Optimization of experimental conditions

The sensitivity of the designed sensor to its analyte is significantly dependent on experimental parameters such as the analyte concentration, pH of the supporting electrolyte, deposition time, and deposition voltage. Consequently, these parameters for OTA detection were optimized using CV and DPV, respectively, on the GCE/Ni-MOF/cRGO electrode.

Firstly, a fixed concentration of OTA standard was selected for subsequent optimization studies, where a working range from 10.00 fg mL^{-1} to 0.10 ng mL^{-1} OTA in a PBS buffer solution (pH = 7.4) was employed (**Figure 4.27a**). The concentration selected was 10.00 fg mL^{-1} where the potential of interest was 0.5 V for the anodic peak. The following step involved optimizing the pH of the 10.00 fg mL^{-1} OTA standard prepared in PBS buffer solution, where a working pH range (pH 4.0, 6.0, 7.4 and 9.0) to account for an acidic, neutral and basic pH was used. pH 7.4 attained the optimum response and was adopted throughout the study (**Figure 4.27b**). Finally, the deposition time (0 s to 60 s) and deposition voltage (-1.4 V to 0.2 V) parameters were similarly optimized to determine the most sensitive analytical response for the 10.00 fg mL^{-1} OTA standard using DPV. The maximum anodic responses were obtained at DT = 0 s and DV = -1.4 V **(Figure 4.28a-b)**, with these parameters subsequently selected for further analysis.

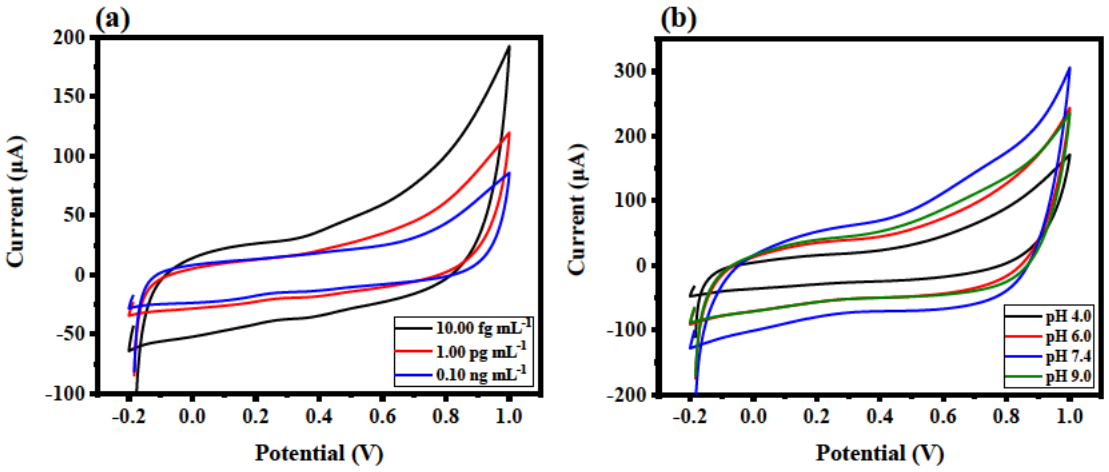

Figure 4.27. Cyclic voltammograms of **(a)** concentration optimization (10.00 fg mL^{-1} to 0.10 ng mL^{-1}) **(b)** pH optimization (pH 4-9, 10.00 fg mL^{-1}) of OTA prepared in PBS solution using GCE/Ni-MOF/cRGO electrode.

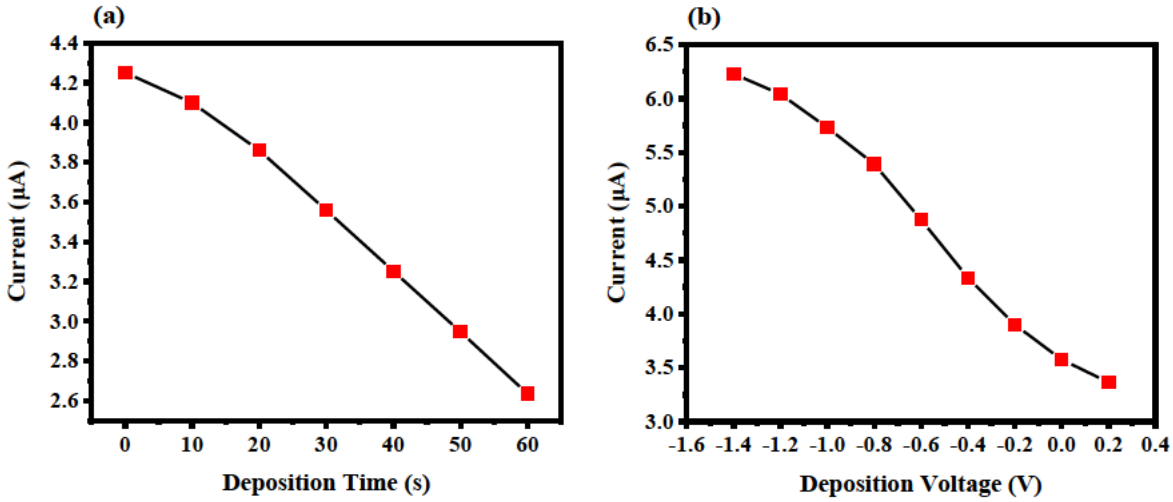

Figure 4.28. Line graphs of **(a)** deposition time optimization and **(b)** deposition voltage optimization for DPV of 10.00 fg mL^{-1} OTA prepared in PBS solution using GCE/Ni-MOF/cRGO electrode.

4.3.2.3) Evaluation of electrode performance towards OTA

In order to test the electrochemical performance of the characterized layer-by-layer electrodes, they were assessed for OTA sensitivity using CV at 0.025 V s^{-1} and EIS from 100 kHz to 0.1 Hz (applied potential of 0.5 V) in a 10.00 fg mL^{-1} OTA solution prepared in PBS, as shown in **Figure 4.29**.

For CV analysis (**Figure 4.29a**), it is found that the GCE/Ni-MOF/cRGO anodic current response is considerably greater and hence more significant in terms of analyte response in comparison to the other electrode layers. This can be attributed to the enhanced transfer of

electrons between OTA and the composite. The trend observed regarding the magnitudes of anodic current responses (E_{pa} = 0.5 V), which elucidates these findings, is as follows: GCE/Ni-MOF (i_{pa} = 0.99 μA) < GCE (i_{pa} = 1.15 μA) < GCE/cRGO (i_{pa} = 4.23 μA) < GCE/Ni-MOF/cRGO (i_{pa} = 47.83 μA). Thus, the GCE/Ni-MOF/cRGO layer having the highest magnitude anodic peak response was selected for further method development for OTA analyses.

With regard to EIS analysis (**Figure 4.29b**), it is observed that a significantly small impedance signal is obtained for the GCE/Ni-MOF/cRGO electrode relative to the other layers. The decreased trend in R_{ct} values **(Table 4.10)** justifies the overall improved charge transfer deduced between the OTA analyte and the GCE/Ni-MOF/cRGO layer. All electrode layers were fitted in *[R([RW]Q)]* Randles equivalent circuits **(Figure 4.29c)**.

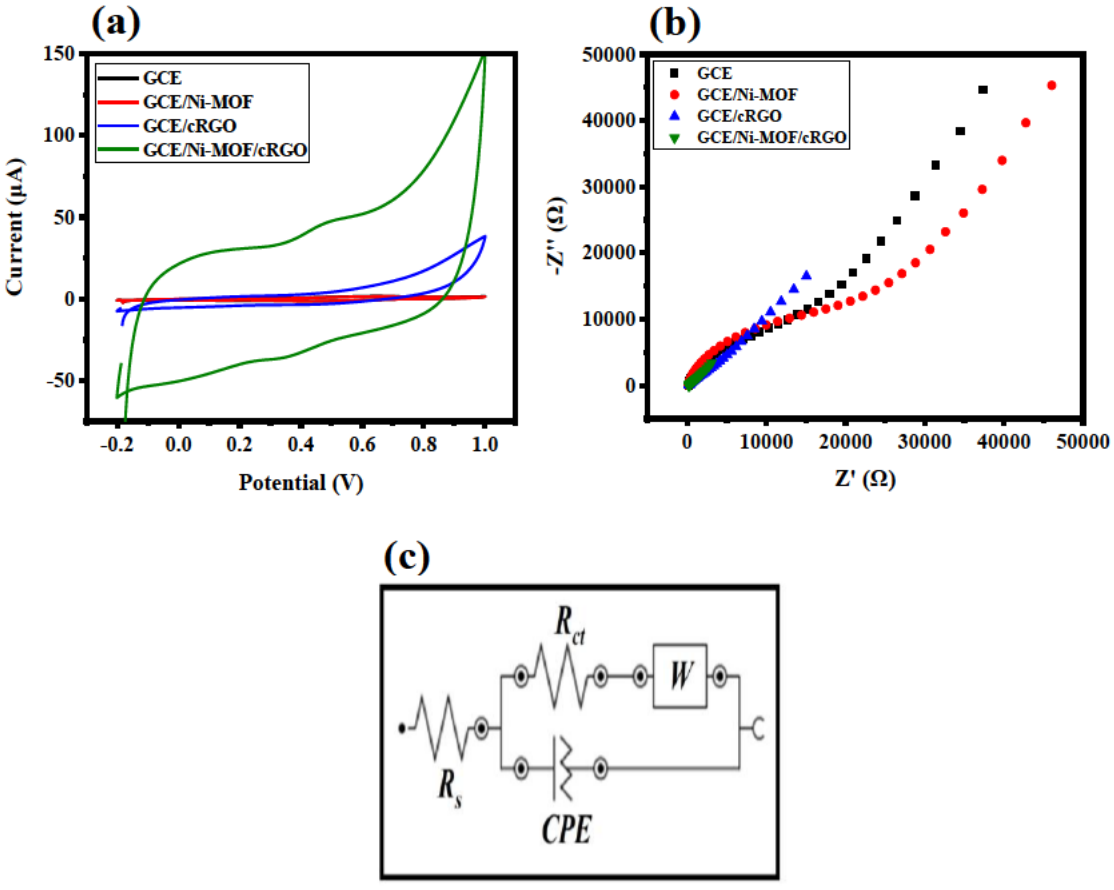

Figure 4.29. Overlay of **(a)** CV and **(b)** EIS for layer-by-layer electrode study of 10.00 fg mL^{-1} OTA prepared in PBS solution. Randles equivalent circuit of **(c)** GCE, GCE/Ni-MOF, GCE/cRGO and GCE/Ni-MOF/cRGO *[R([RW]Q)]*.

Table 4.10. EIS equivalent circuit data of GCE/Ni-MOF/cRGO electrode using 10.00 fg mL^{-1} OTA prepared in PBS solution.

Electrode	R_s (kΩ) (%Error)	R_{ct} (kΩ) (%Error)	χ^2
GCE	0.162 (1.55)	8.455 (7.40)	0.20
GCE/Ni-MOF	0.161 (1.62)	14.874 (4.59)	0.18
GCE/cRGO	0.194 (1.60)	2.938 (21.27)	0.11
GCE/Ni-MOF/cRGO	0.193 (2.32)	0.071 (15.24)	0.18

4.3.2.4) Evaluation of OTA analytical performance on developed electrode

The analytical performance of the constructed GCE/Ni-MOF/cRGO sensor for OTA was assessed using DPV. The calibration curve obtained was plotted in the quadratic analytical response range of 10.00 fg mL^{-1} to 90.00 fg mL^{-1} (E_p = 0.3 V to 0.7 V), as depicted in **Figure 4.30**. It was found that the anodic peak exhibited a sensitive response to the change in concentration of the OTA analyte in the positive current direction (**Figure 4.30a**), resulting in an upwards slope in the calibration curve in **Figure 4.30b** (i_{pa} (μA) = -0.0011 [OTA]^2 + 0.1677 [OTA] + 9.069, R^2 = 0.9912). The LOD and LOQ were evaluated to be 3.29 fg mL^{-1} and 10.97 fg mL^{-1} using **Eqs. (4.1)** and **(4.2)**, respectively. A comparison to other analytical techniques regarding OTA detection is depicted in **Table 4.11**.

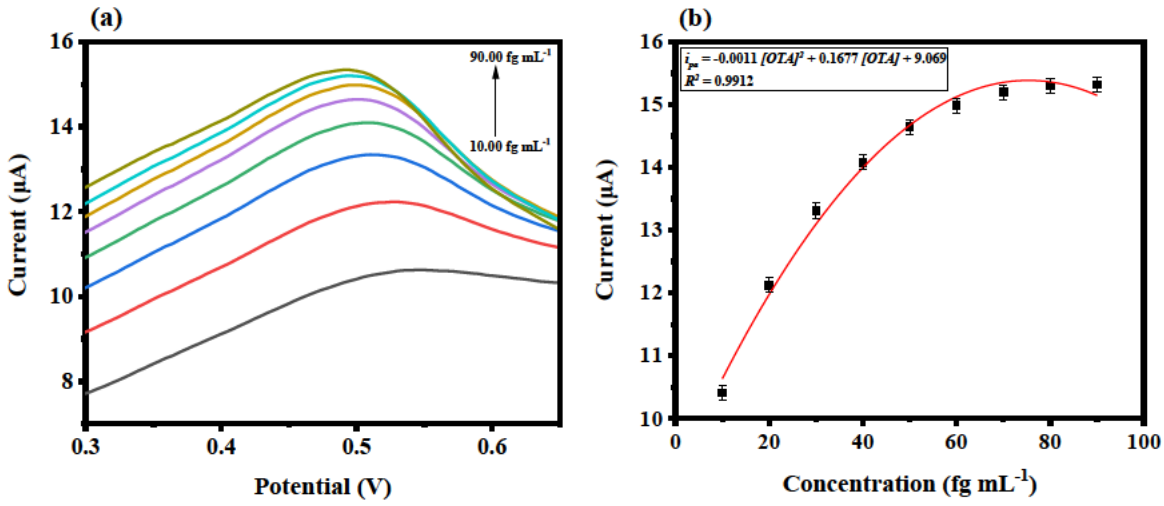

Figure 4.30. (a) DPVs (n = 3) at GCE/Ni-MOF/cRGO electrode with increasing concentrations of OTA (10.00 fg mL^{-1} to 90.00 fg mL^{-1}) prepared in PBS solution and **(b)** calibration curve of corresponding oxidation peak currents plotted against OTA concentrations.

Table 4.11. Comparison of the analytical performance of developed sensor with other analytical techniques for OTA detection.

Analyte	Detection Strategy	LOD	Reference
OTA	Immunoassay	0.16 ng mL^{-1}	(Yi *et al.* 2023)
	Molecularly imprinted polymer	0.675 ng mL^{-1}	(Dou *et al.* 2023)
	DNA tweezer	0.032 ng mL^{-1}	(Chen *et al.* 2022a)
	Aptasensor	1.03 pg mL^{-1}	(Wang *et al.* 2022b)
	Electrochemistry	**3.29 fg mL^{-1}**	**Current work**

4.3.2.5) Real sample analysis

To assess the applicability of the developed sensor, samples of corn flour and rice flour were analyzed to determine the recoveries of the OTA analyte spiked at different concentrations. The overall OTA percentage recoveries in both products were excellent in the range of 95% to 105%, with low percentage relative standard deviations (%RSD $<$ 10%) also noted, as per **Table 4.12**.

Table 4.12. Recoveries of OTA in real samples using developed sensor (n = 3).

Sample	Spiked (fg mL^{-1})	Found (fg mL^{-1})	%Recovery	%RSD
Corn flour	10.00	9.99	99.86	0.70
	20.00	20.12	100.61	0.41
	30.00	30.67	102.22	1.26
Rice flour	10.00	9.51	95.06	3.51
	20.00	20.96	104.78	3.13
	30.00	29.40	98.01	0.66

4.3.2.6) Reproducibility, repeatability, storage stability and interference studies

Five identically modified electrodes yielded a %RSD of 6.05% in the reproducibility study (**Figure 4.31a**). With regard to the repeatability study, using a single electrode (n = 5), the %RSD was reported to be 6.75%. In terms of storage stability (electrodes stored at 4℃), the analysis revealed a decrease of 8.41% in anodic current after the second week and 9.80% after the third, where the study was performed three times over a period of 21 days. Finally, an interference study was conducted using DPV whereby the analytical detection of OTA was found to be dominant over that of ZEN and AFB1 in the same concentrations (10.00 fg mL^{-1} OTA, ZEN and AFB1) in a solution containing all three mycotoxins (**Figure 4.31b**).

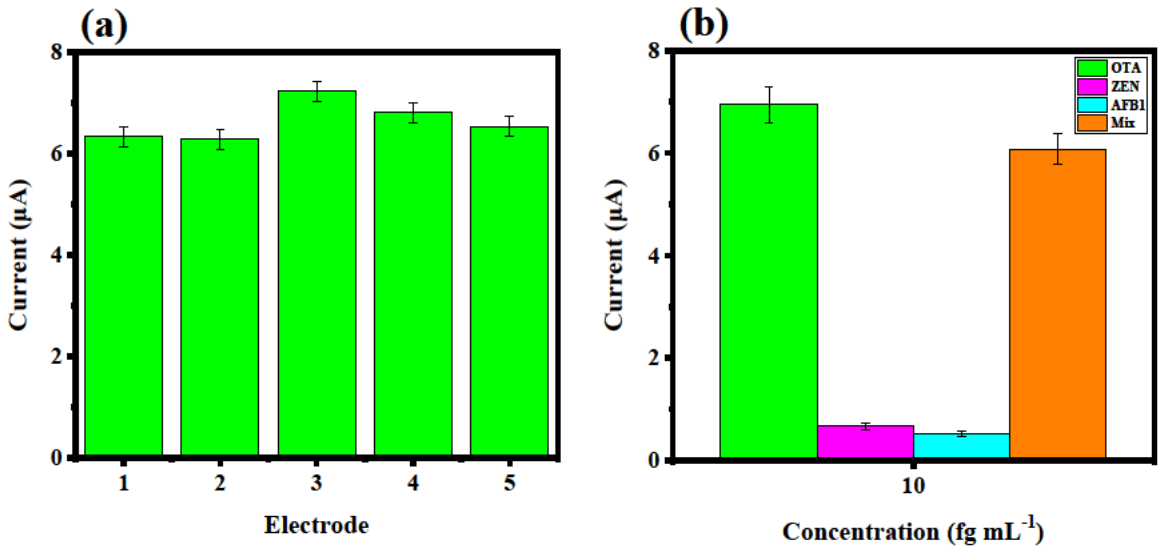

Figure 4.31. (a) Bar graph of reproducibility study (n = 3) for DPV of 10.00 fg mL^{-1} OTA prepared in PBS solution with different **(1-5)** GCE/Ni-MOF/cRGO electrodes **(b)** Bar graph of DPV interference study (n = 3) of OTA in the presence of ZEN and AFB1 of the same concentration (10.00 fg mL^{-1} prepared in PBS).

4.3.3) Computational analyses

4.3.3.1) MD simulation

The interaction between OTA and Ni-MOF was studied using MD simulations. Structural changes between the Ni-MOF substrate and 10 OTA adsorbates (in yellow) are depicted in **Figure 4.32**. It is observed that the OTA molecules tend to electrostatically cluster within the Ni-O indices of the Ni-MOF cage. This can be attributed to the affinity between the functional groups of OTA and trimesic acid present in the inner linkages of the MOF. In addition, it is assumed that the structural integrity of the Ni-MOF-OTA complex remains resolute, as justified by the stabilization of its energetic profile throughout the simulation (**Figure 4.33**). Finally, from an experimental point of view, it can be deduced that the binding of trimesic acid to OTA, as well as the intrinsic conductivity of the Ni-O atoms, contribute strongly to the analyte loading and electron transfer properties of the Ni-MOF for its application in the constructed sensor for OTA detection.

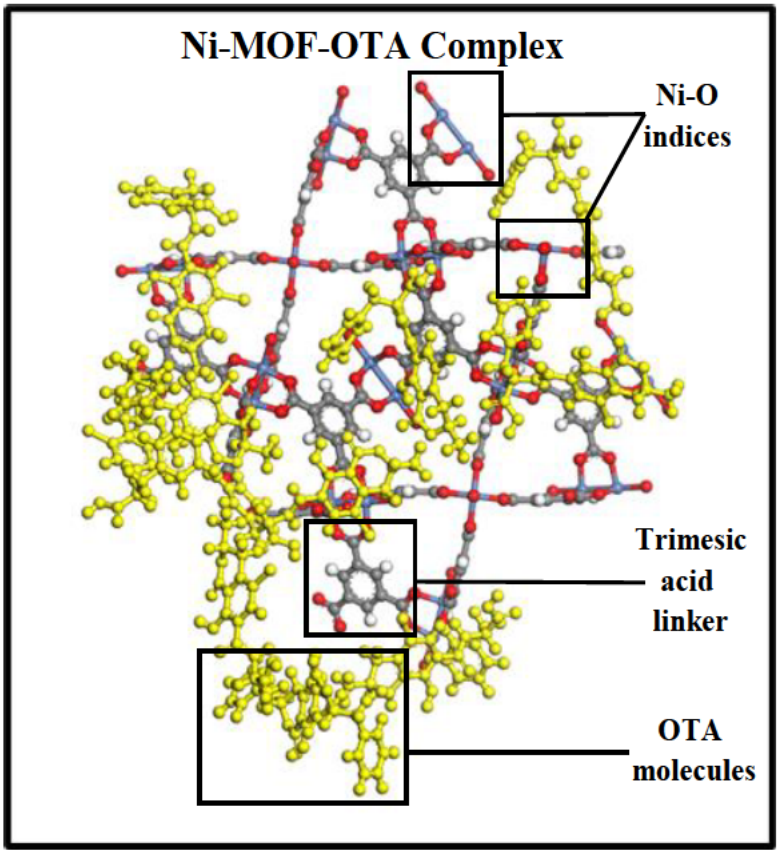

Figure 4.32. MD simulation of 10 OTA molecules (shown in yellow) interacting with Ni-MOF.

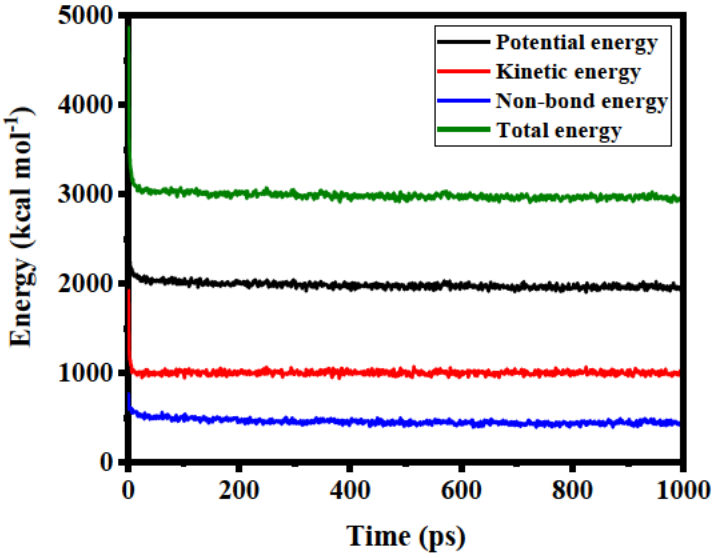

Figure 4.33. Total energy distribution for MD simulation of Ni-MOF-OTA complex.

4.4) Conclusion

A sensitive analytical range was exhibited by the developed electrochemical sensor. with low LOD and LOQ values reported (3.29 fg mL^{-1} and 10.97 fg mL^{-1}, respectively), along with excellent spike recoveries (95% to 105%) for real sample analysis. CV studies for the GCE/Ni-MOF/cRGO electrode response reported a significant enhancement of anodic current for OTA, which was supported by the reduction in resistance to charge transfer elucidated by EIS analysis. Finally, MD simulations predicted a strong electrostatic interaction between the OTA analyte and Ni-MOF, corresponding to the experimental voltammetry findings supporting the sensitivity of the constructed sensor for OTA detection.

CHAPTER 5 – SUMMARY, CONCLUSIONS AND FUTURE RECOMMENDATIONS

This chapter presents the summary, conclusions and future recommendations of this work.

5.1) Summary

The development of electrochemical sensors for AFB1, ZEN and OTA respectively, was successfully fulfilled for the detection of mycotoxins in foods.

In the first case study, an ultrasensitive electrochemical aptasensor for AFB1 analysis was constructed using carboxylated multiwalled carbon nanotubes (cMWCNTs) and iron oxide (Fe_3O_4) nanoparticles (NPs) on a glassy carbon electrode (GCE). The peptide bond formation by EDC coupling between the aptamer and cMWCNTs-Fe_3O_4 NP composite exhibited a strong anodic redox response from AFB1 using cyclic voltammetry (CV) in this study. Applying differential pulse voltammetry (DPV), the GCE/cMWCNTs-Fe_3O_4 NP aptasensor exhibited very low limits of detection (LOD) and quantification (LOQ) of 0.43 fg mL^{-1} and 1.44 fg mL^{-1}, respectively, over a calibration range of 0.50 fg mL^{-1} to 5.00 fg mL^{-1}. For the actual sample analysis, excellent spike recoveries of 95% to 105% were obtained for corn and rice flour. Single particle ICP-MS (spICP-MS) confirmed the average mass-based diameter of the synthesized Fe_3O_4 NPs to be in the nano-range ($d \approx 20$ nm), the properties of which are essential for the facilitation of strong electron transfer in DPV sensing. Density functional theory (DFT) and molecular docking studies predicted the sensing mechanism and supported deductions based on the AFB1 capture by the employed aptamer, respectively.

Regarding the second case study, the impact of PEGylated Fe_3O_4 NPs interacted with carboxylic acid functionalized multiwalled carbon nanotubes (PEG-Fe_3O_4 NPs/cMWCNTs) was investigated for the design of an electrochemical sensor for ZEN analysis. Results showed that the nanocomposite-enhanced electrode exhibited a strong cathodic redox response of ZEN using CV. The developed sensor provided significantly low LODs and LOQs of 0.34 fg mL^{-1} and 1.12 fg mL^{-1}, respectively, over a calibration range of 1.00 fg mL^{-1} to 10.00 fg mL^{-1} by DPV. Excellent spike recoveries of 92% to 106% were obtained for real samples of rice and corn flour. The multidetector Asymmetrical-Flow Field-Flow Fractionation (AF4) measurements on the synthesized PEG-Fe_3O_4 NPs verified their nano-sized dimensions ($r_g \approx$ 31 nm), contributing to the exceptionally high charge transfer in DPV sensing. The Monte

Carlo (MC) adsorption simulation studies demonstrated that the ZEN/PEG-Fe_3O_4 NP/cMWCNTs electrode interaction was the strongest on the GCE surface.

Finally, the third case study entailed the development of an electrochemical sensor for OTA analysis using a nickel metal-organic framework (Ni-MOF) with carboxylated reduced graphene oxide (cRGO) on a GCE. Results showed that the nanocomposite-enhanced electrode exhibited a strong anodic redox response of OTA using CV. Applying DPV, the GCE/Ni-MOF/cRGO sensor provided significantly low LODs and LOQs of 3.29 fg mL^{-1} and 10.97 fg mL^{-1}, respectively, over a calibration range of 10.00 fg mL^{-1} to 90.00 fg mL^{-1}. Regarding real sample analysis, excellent spike recoveries from 95% to 105% were obtained for corn and rice flour. Molecular dynamics (MD) studies predicted that the Ni-MOF exhibited a strong electrostatic interaction with the OTA analyte, supporting experimental findings.

5.2) Conclusions

Case Studies I, II and III involved the analyses of AFB1, ZEN and OTA respectively in foods. Various electrochemical sensor methodologies for the quantification of each mycotoxin in rice and corn flour samples were developed. In Case Study I, the detection of AFB1 was based on the development of an MB-tagged aptasensor supported by the cMWCNTs-Fe_3O_4 NP composite electrode layer. On the other hand, for Case Study II, the developed electrochemical sensor highlighted entangling polymeric chains of PEG acting as a trapping mechanism for ZEN analysis within the synthesized PEG-Fe_3O_4 NPs. With regards to Case Study III, the affinitive analyte loading, and innate conductive properties of Ni-MOF were utilized for the sensing of OTA. Very low LOD and LOQ values, along with excellent spike recoveries were reported for all three case studies. Finally, the employed computational methodologies predicted and validated strong intermolecular interactions between the analytes and the fabricated electrode surfaces.

5.3) Future recommendations

The following recommendations may be considered based on the findings of the study:

- Implementation of screen-printed electrodes for the development of on-site sensors.
- Increasing the number and variation of samples for testing.
- Exploring complex sample matrix analysis outside food applications.

- Employment of more computational studies extended to assess the conformational profile of the nanocomposites of the different fabricated sensors.

This study contributes toward food quality control and regulatory frameworks for the prevention of mycotoxin exposure to human and animal health in South Africa.

REFERENCES

Abbasi, M., Ezazi, M., Jouyban, A., Lulek, E., Asadpour-Zeynali, K., Ertas, Y. N., Houshyar, J., Mokhtarzadeh, A. and Soleymani, J. 2022. An ultrasensitive and preprocessing-free electrochemical platform for the detection of doxorubicin based on tryptophan/polyethylene glycol-cobalt ferrite nanoparticles modified electrodes. *Microchemical Journal*, 183: 108055-108062.

Abdullah, M. P. and Zulkepli, S. A. 2015. The functionalization and characterization of multi-walled carbon nanotubes (MWCNTs). *AIP Conference Proceedings*, 1678 (1): 50033-50037.

Abid, N., Khan, A. M., Shujait, S., Chaudhary, K., Ikram, M., Imran, M., Haider, J., Khan, M., Khan, Q. and Maqbool, M. 2022. Synthesis of nanomaterials using various top-down and bottom-up approaches, influencing factors, advantages, and disadvantages: A review. *Advances in Colloid and Interface Science*, 300: 102597-102614.

Abnous, K., Danesh, N. M., Alibolandi, M., Ramezani, M., Sarreshtehdar Emrani, A., Zolfaghari, R. and Taghdisi, S. M. 2017. A new amplified π-shape electrochemical aptasensor for ultrasensitive detection of aflatoxin B1. *Biosensors and Bioelectronics*, 94: 374-379.

Adegoke, K. A. and Maxakato, N. W. 2022. Porous metal oxide electrocatalytic nanomaterials for energy conversion: Oxygen defects and selection techniques. *Coordination Chemistry Reviews*, 457: 214389-214426.

Ahmed, S. F., Mofijur, M., Ahmed, B., Mehnaz, T., Mehejabin, F., Maliat, D., Hoang, A. T. and Shafiullah, G. M. 2022. Nanomaterials as a sustainable choice for treating wastewater. *Environmental Research*, 214: 113807-113825.

Al-Bagawi, A. H., Bayoumy, A. M. and Ibrahim, M. A. 2020. Molecular modeling analyses for graphene functionalized with Fe_3O_4 and NiO. *Heliyon*, 6 (7): 4456-4462.

Alder, B. J. and Wainwright, T. E. 1959. Studies in Molecular Dynamics. I. General Method. *The Journal of Chemical Physics*, 31 (2): 459-466.

Ali, M. F. B., Saraya, R. E., El Deeb, S., Ibrahim, A. E. and Salman, B. I. 2023. An Innovative Polymer-Based Electrochemical Sensor Encrusted with Tb Nanoparticles for the Detection of Favipiravir: A Potential Antiviral Drug for the Treatment of COVID-19. *Biosensors*, 13 (2): 243-256.

Alkhuder, K. 2022. Attenuated total reflection-Fourier transform infrared spectroscopy: a universal analytical technique with promising applications in forensic analyses. *International Journal of Legal Medicine*, 136 (6): 1717-1736.

Antarnusa, G., Jayanti, P. D., Denny, Y. R. and Suherman, A. 2022. Utilization of co-precipitation method on synthesis of Fe_3O_4/PEG with different concentrations of PEG for biosensor applications. *Materialia*, 25: 101525-101536.

Antarnusa, G. and Suharyadi, E. 2020. A synthesis of polyethylene glycol (PEG)-coated magnetite Fe_3O_4 nanoparticles and their characteristics for enhancement of biosensor. *Materials Research Express*, 7 (5): 56103-56108.

Aoki, K., Tokuda, K. and Matsuda, H. 1984. Theory of differential pulse voltammetry at stationary planar electrodes. *Journal of Electroanalytical Chemistry and Interfacial Electrochemistry*, 175 (1): 1-13.

Arodola, O. A., Kanchi, S., Hloma, P., Bisetty, K., Asiri, A. M. and Inamuddin. 2020. An in-silico layer-by-layer adsorption study of the interaction between Rebaudioside A and the T1R2 human sweet taste receptor: modelling and biosensing perspectives. *Scientific Reports*, 10 (1): 18391-18408.

Attarki, J., Khnifira, M., Boumya, W., Mahsoune, A., Lemdek, E. M., Sadiq, M., Abdennouri, M., Kaya, S. and Barka, N. 2023. Adsorption mechanism investigation of methylthioninium chloride dye onto some metal phosphates using Monte Carlo dynamic simulations and DFT calculations. *Inorganic Chemistry Communications*, 149: 110436-110444.

Ayyappa, B., Kanchi, S., Sabela, I. M. and Bisetty, K. 2021. Separation of Sucralose in Food Samples using Amines as Background Electrolyte Supported with DFT Calculations. *Current Analytical Chemistry*, 17 (7): 989-1002.

Azara, A., Belbessai, S. and Abatzoglou, N. 2022. A review of filamentous carbon nanomaterial synthesis via catalytic conversion of waste plastic pyrolysis products. *Journal of Environmental Chemical Engineering*, 10 (1): 107049-107073.

Bahmani, H. and Mostofinejad, D. 2022. Microstructure of ultra-high-performance concrete (UHPC) – A review study. *Journal of Building Engineering*, 50: 104118-104137.

Bai, Q., Yin, Y., Liu, Y., Jiang, H., Wu, M., Wang, W., Tan, Z., Liu, J., Moon, M. H. and Xing, B. 2023. Flow field-flow fractionation hyphenated with inductively coupled plasma mass spectrometry: a robust technique for characterization of engineered elemental metal nanoparticles in the environment. *Applied Spectroscopy Reviews*, 58 (2): 110-131.

Baig, N., Kammakakam, I. and Falath, W. 2021. Nanomaterials: a review of synthesis methods, properties, recent progress, and challenges. *Materials Advances*, 2 (6): 1821-1871.

Balaram, V., Rahaman, W. and Roy, P. 2022. Recent advances in MC-ICP-MS applications in Earth and environmental sciences: Challenges and solutions. *Geosystems and Geoenvironment*, 1 (2): 100019-100044.

Becheva, Z. R., Gabrovska, K. I., Godjevargova, T. I. and Zvereva, E. A. 2019. Aflatoxin B1 Determination in Peanuts by Magnetic Nanoparticle–Based Immunofluorescence Assay. *Food Analytical Methods*, 12 (6): 1456-1465.

Beitollahi, H., Tajik, S., Dourandish, Z., Zhang, K., Le, Q. V., Jang, H. W., Kim, S. Y. and Shokouhimehr, M. 2020. Recent Advances in the Aptamer-Based Electrochemical Biosensors for Detecting Aflatoxin B1 and Its Pertinent Metabolite Aflatoxin M1. *Sensors*, 20 (11): 3256-3272.

Biovia, D. S. 2016. Discovery Studio modelling. v. 16.10. 15350 ed (computer software).

Bölükbaşı, Ö. S., Yola, B. B., Boyacıoğlu, H. and Yola, M. L. 2022. A novel paraoxon imprinted electrochemical sensor based on MoS_2NPs@MWCNTs and its application to tap water samples. *Food and Chemical Toxicology*, 163: 112994-113002.

Bouali, W., Kurtay, G., Genç, A. A., Ahmed, H. E. H., Soylak, M., Erk, N. and Karimi-Maleh, H. 2023. Nanodiamond (ND)-Based ND@$CuAl_2O_4$@Fe_3O_4 electrochemical sensor for Tofacitinib detection: A unified approach to integrate experimental data with DFT and molecular docking. *Environmental Research*, 238: 117166-117180.

Braz, B. A., Moreira, C. S., Oliveira, V. B. and Pinto, A. M. F. R. 2022. Electrochemical impedance spectroscopy as a diagnostic tool for passive direct methanol fuel cells. *Energy Reports*, 8: 7964-7975.

Brett, C. M. A. 2022. Electrochemical Impedance Spectroscopy in the Characterisation and Application of Modified Electrodes for Electrochemical Sensors and Biosensors. *Molecules*, 27 (5): 1497-1513.

Bunaciu, A. A., Udriştioiu, E. g. and Aboul-Enein, H. Y. 2015. X-Ray Diffraction: Instrumentation and Applications. *Critical Reviews in Analytical Chemistry*, 45 (4): 289-299.

Burke, K. 2012. Perspective on density functional theory. *The Journal of Chemical Physics*, 136 (15): 150901-150909.

Caglayan, M. O., Şahin, S. and Üstündağ, Z. 2022. Detection Strategies of Zearalenone for Food Safety: A Review. *Critical Reviews in Analytical Chemistry*, 52 (2): 294-313.

Cai, Y., Chen, Z., Wang, S., Chen, J., Hu, B., Shen, C. and Wang, X. 2023. Carbon-based nanocomposites for the elimination of inorganic and organic pollutants through sorption and catalysis strategies. *Separation and Purification Technology*, 308: 122862-122875.

Cesewski, E. and Johnson, B. N. 2020. Electrochemical biosensors for pathogen detection. *Biosensors and Bioelectronics*, 159: 112214-112242.

Chavan, S. G., Yagati, A. K., Koyappayil, A., Go, A., Yeon, S., Lee, T. and Lee, M.-H. 2022. Conformationally Flexible Dimeric-Serotonin-Based Sensitive and Selective Electrochemical Biosensing Strategy for Serotonin Recognition. *Analytical Chemistry*, 94 (49): 17020-17030.

Chavez, R. A., Opit, G., Opoku, B. and Stasiewicz, M. J. 2023. Spectral kernel sorting based on high-risk visual features associated with mycotoxin contamination reduces aflatoxin and fumonisin contamination in maize from Ghana. *Food Control*, 151: 109788-109797.

Chen, C. and Wang, J. 2020. Optical biosensors: an exhaustive and comprehensive review. *Analyst*, 145 (5): 1605-1628.

Chen, F., Zhang, Y. and Huang, H. 2023. Layered photocatalytic nanomaterials for environmental applications. *Chinese Chemical Letters*, 34 (3): 107523-107537.

Chen, R., Mao, Z., Lu, R., Wang, Z., Hou, Y., Zhu, W., Li, S., Ren, S., Han, D., Liang, J. and Gao, Z. 2022a. Simple and programmed three-dimensional DNA tweezer for simultaneous one-step detection of ochratoxin A and zearalenone. *Spectrochimica Acta Part A: Molecular and Biomolecular Spectroscopy*, 272: 120991-120997.

Chen, R., Sun, Y., Huo, B., Mao, Z., Wang, X., Li, S., Lu, R., Li, S., Liang, J. and Gao, Z. 2021. Development of Fe_3O_4@Au nanoparticles coupled to Au@Ag core-shell nanoparticles for the sensitive detection of zearalenone. *Analytica Chimica Acta*, 1180: 1-9.

Chen, X., Gao, D., Sun, F., Li, Z., Wang, Y., Qiu, C., He, K. and Wang, J. 2022b. Nanomaterial-based aptamer biosensors for ochratoxin A detection: a review. *Analytical and Bioanalytical Chemistry*, 414 (9): 2953-2969.

Chen, X., Li, J., Li, J., Zhang, L., Zhao, P., Wang, C., Fei, J. and Xie, Y. 2022c. Determination of luteolin in Chrysanthemum tea with a ultra-sensitive electrochemical sensor based on MoO_3/poly(3,4-ethylene dioxythiophene)/gama-cyclodextrin metal–organic framework composites. *Food Chemistry*, 397: 133723-133731.

Chen, Z., Yang, M., Li, Z., Liao, W., Chen, B., Yang, T., Hu, R., Yang, Y. and Meng, S. 2022d. Highly sensitive and convenient aptasensor based on Au NPs@Ce-TpBpy COF for quantitative determination of zearalenone. *RSC Advances*, 12 (27): 17312-17320.

Cheng, W., Tang, X., Zhang, Y., Wu, D. and Yang, W. 2021. Applications of metal-organic framework (MOF)-based sensors for food safety: Enhancing mechanisms and recent advances. *Trends in Food Science & Technology*, 112: 268-282.

Chu, H., Sun, D. and Cui, P. 2022. Highly Water-Stable Zn_5 Cluster-Based Metal–Organic Framework for Efficient Gas Storage and Organic Dye Adsorption. *Inorganic Chemistry*, 61 (48): 19642-19648.

Chubarov, A. S. 2022. Serum Albumin for Magnetic Nanoparticles Coating. *Magnetochemistry*, 8 (2): 13-30.

Cölfen, H. and Antonietti, M. 2000. Field-Flow Fractionation Techniques for Polymer and Colloid Analysis. In: Schmidt, M. ed. *New Developments in Polymer Analytics I*. Berlin, Heidelberg: Springer Berlin Heidelberg, 67-187. Available: https://doi.org/10.1007/3-540-48764-6_2 (Accessed 12/10/2023).

Contado, C. 2017. Field flow fractionation techniques to explore the "nano-world". *Analytical and Bioanalytical Chemistry*, 409 (10): 2501-2518.

Coskun, O. 2016. Separation techniques: Chromatography. *Northern Clinics of Istanbul*, 3 (2): 156-160.

Cowie, J. M. G. and Arrighi, V. 2007. Polymers: Chemistry and Physics of Modern Materials. In. CRC press, 229-252.

da Silva, A. B. S. and Arruda, M. A. Z. 2023. Single-cell ICP-MS to address the role of trace elements at a cellular level. *Journal of Trace Elements in Medicine and Biology*, 75: 127086-127100.

Dadmehr, M., Shahi, S. C., Malekkiani, M., Korouzhdehi, B. and Tavassoli, A. 2023. A stem-loop like aptasensor for sensitive detection of aflatoxin based on graphene oxide/AuNPs nanocomposite platform. *Food Chemistry*, 402: 134212-134218.

Dan, Y., Shi, H., Stephan, C. and Liang, X. 2015. Rapid analysis of titanium dioxide nanoparticles in sunscreens using single particle inductively coupled plasma–mass spectrometry. *Microchemical Journal*, 122: 119-126.

Danel, T., Łęski, J., Podlewska, S. and Podolak, I. T. 2023. Docking-based generative approaches in the search for new drug candidates. *Drug Discovery Today*, 28 (2): 103439-103445.

Daoui, O., Nour, H., Abchir, O., Elkhattabi, S., Bakhouch, M. and Chtita, S. 2023. A computer-aided drug design approach to explore novel type II inhibitors of c-Met receptor tyrosine kinase for cancer therapy: QSAR, molecular docking, ADMET and molecular dynamics simulations. *Journal of Biomolecular Structure and Dynamics*, 41 (16): 7768-7785.

de Jesús González, A. and Rangel Vázquez, N. A. 2023. PM3 semi-empirical method and Monte Carlo simulation application on pesticides adsorption on SWCNT. *Colloid and Interface Science Communications*, 53: 100699-100705.

De Rycke, E., Foubert, A., Dubruel, P., Bol'hakov, O. I., De Saeger, S. and Beloglazova, N. 2021. Recent advances in electrochemical monitoring of zearalenone in diverse matrices. *Food Chemistry*, 353: 129342-129349.

Demir Duman, F., Monaco, A., Foulkes, R., Becer, C. R. and Forgan, R. S. 2022. Glycopolymer-Functionalized MOF-808 Nanoparticles as a Cancer-Targeted Dual Drug Delivery System for Carboplatin and Floxuridine. *ACS Applied Nano Materials*, 5 (10): 13862-13873.

Dhinakaran, V., Vigneswari, K., Lavanya, M. and Varsha Shree, M. 2020. Chapter Ten - Point-of-care applications with graphene in human life. In: Hussain, C. M. ed. *Comprehensive Analytical Chemistry*. Elsevier, 235-262. Available: https://www.sciencedirect.com/science/article/pii/S0166526X20300623 (Accessed 10/11/2023).

Díez-Pascual, A. M. 2021. Carbon-Based Nanomaterials. *International Journal of Molecular Sciences*, 22 (14): 7726-7730.

Dikshit, P. K., Kumar, J., Das, A. K., Sadhu, S., Sharma, S., Singh, S., Gupta, P. K. and Kim, B. S. 2021. Green Synthesis of Metallic Nanoparticles: Applications and Limitations. *Catalysts*, 11 (8): 902-936.

Dou, M., Wang, S., Li, W., Li, Q., Xu, J. and Li, J. 2023. High-performance molecularly imprinted polymers grafted magnetic photonic crystal microspheres for selective enrichment of ochratoxin a. *Journal of Chromatography A*, 1695: 463932-463941.

Du, Q., Wu, P., Hu, F., Li, G., Shi, J. and He, H. 2019. Novel molecularly imprinted polymers on metal–organic frameworks as sensors for the highly selective detection of zearalenone in wheat. *New Journal of Chemistry*, 43 (18): 7044-7050.

Duan, F., Rong, F., Guo, C., Chen, K., Wang, M., Zhang, Z., Pettinari, R., Zhou, L. and Du, M. 2022. Electrochemical aptasensing strategy based on a multivariate polymertitanium-metal-organic framework for zearalenone analysis. *Food Chemistry*, 385: 132654-132663.

Dym, O., Xenarios, I., Ke, H. and Colicelli, J. 2002. Molecular Docking of Competitive Phosphodiesterase Inhibitors. *Molecular Pharmacology*, 61 (1): 20-25.

Ebada, D., Hefnawy, H. T., Gomaa, A., Alghamdi, A. M., Alharbi, A. A., Almuhayawi, M. S., Alharbi, M. T., Awad, A., Al Jaouni, S. K., Selim, S., Eldeeb, G. S. and Namir, M. 2023. Characterization of Delonix regia Flowers’ Pigment and Polysaccharides: Evaluating Their Antibacterial, Anticancer, and Antioxidant Activities and Their Application as a Natural Colorant and Sweetener in Beverages. *Molecules*, 28 (7): 3243-3261.

El-Sayed, R. A., Jebur, A. B., Kang, W. and El-Demerdash, F. M. 2022. An overview on the major mycotoxins in food products: characteristics, toxicity, and analysis. *Journal of Future Foods*, 2 (2): 91-102.

El Ghandoor, H., Zidan, H. M., Khalil, M. M. H. and Ismail, M. I. M. 2012. Synthesis and Some Physical Properties of Magnetite (Fe_3O_4) Nanoparticles. *International Journal of Electrochemical Science*, 7 (6): 5734-5745.

Elahi, N. and Rizwan, M. 2021. Progress and prospects of magnetic iron oxide nanoparticles in biomedical applications: A review. *Artificial Organs*, 45 (11): 1272-1299.

Elton, L. R. B. and Jackson, D. F. 1966. X-Ray Diffraction and the Bragg Law. *American Journal of Physics*, 34 (11): 1036-1038.

Espinoza, E. M., Clark, J. A., Soliman, J., Derr, J. B., Morales, M. and Vullev, V. I. 2019. Practical Aspects of Cyclic Voltammetry: How to Estimate Reduction Potentials When Irreversibility Prevails. *Journal of The Electrochemical Society*, 166 (5): 3175-3187.

Evtugyn, G. and Hianik, T. 2019. Electrochemical Immuno- and Aptasensors for Mycotoxin Determination. *Chemosensors*, 7 (1): 10-38.

Fan, T., Xie, Y. and Ma, W. 2021. Research progress on the protection and detoxification of phytochemicals against aflatoxin B1-Induced liver toxicity. *Toxicon*, 195: 58-68.

Fan, Y., Li, J., Amin, K., Yu, H., Yang, H., Guo, Z. and Liu, J. 2023. Advances in aptamers, and application of mycotoxins detection: A review. *Food Research International*, 170: 113022-113039.

Feng, S., Hua, M. Z., Roopesh, M. S. and Lu, X. 2023. Rapid detection of three mycotoxins in animal feed materials using competitive ELISA-based origami microfluidic paper analytical device (μPAD). *Analytical and Bioanalytical Chemistry*, 415 (10): 1943-1951.

Ganapathe, L. S., Mohamed, M. A., Mohamad Yunus, R. and Berhanuddin, D. D. 2020. Magnetite (Fe_3O_4) Nanoparticles in Biomedical Application: From Synthesis to Surface Functionalisation. *Magnetochemistry*, 6 (4): 68-102.

Gao, H., Yao, J., Jiang, B., Yuan, R. and Xiang, Y. 2022. $NiCo_2S_4$ nanoparticle-dispersed MoS_2 nanosheets for catalytic and sensitive electrochemical aptamer sensing of ochratoxin A via cascaded amplifications. *Sensors and Actuators B: Chemical*, 371: 132530-132535.

Ghalkhani, M., Kaya, S. I., Bakirhan, N. K., Ozkan, Y. and Ozkan, S. A. 2022. Application of Nanomaterials in Development of Electrochemical Sensors and Drug Delivery Systems for Anticancer Drugs and Cancer Biomarkers. *Critical Reviews in Analytical Chemistry*, 52 (3): 481-503.

Ghalkhani, M. and Sohouli, E. 2022. Synthesis of the decorated carbon nano onions with aminated MCM-41/Fe_3O_4 NPs: Morphology and electrochemical sensing performance for methotrexate analysis. *Microporous and Mesoporous Materials*, 331: 111658-111667.

Giannioti, Z., Albero, B., Hernando, M. D., Bontempo, L. and Pérez, R. A. 2023. Determination of Regulated and Emerging Mycotoxins in Organic and Conventional Gluten-Free Flours by LC-MS/MS. *Toxins*, 15 (2): 155-166.

Gnanaraj, C., Sekar, M., Fuloria, S., Swain, S. S., Gan, S. H., Chidambaram, K., Rani, N. N. I. M., Balan, T., Stephenie, S., Lum, P. T., Jeyabalan, S., Begum, M. Y., Chandramohan, V., Thangavelu, L., Subramaniyan, V. and Fuloria, N. K. 2022. In Silico Molecular Docking Analysis of Karanjin against Alzheimer's and Parkinson's Diseases as a Potential Natural Lead Molecule for New Drug Design, Development and Therapy. *Molecules*, 27 (9): 2834-2851.

Gosser, D. K. 1993. Cyclic Voltammetry: Simulation and Analysis of Reaction Mechanisms. In. VCH New York, 27-68.

Goud, K. Y., Hayat, A., Catanante, G., M, S., Gobi, K. V. and Marty, J. L. 2017. An electrochemical aptasensor based on functionalized graphene oxide assisted electrocatalytic signal amplification of methylene blue for aflatoxin B1 detection. *Electrochimica Acta*, 244: 96-103.

Guo, H., Ma, P., Li, K., Zhang, S., Zhang, Y., Guo, H. and Wang, Z. 2022a. A novel ratiometric aptasensor based on dual-emission fluorescent signals and the conformation of G-quadruplex for OTA detection. *Sensors and Actuators B: Chemical*, 358: 131484-131493.

Guo, J.-X., Pan, L.-M., Wang, M.-C., Chen, L.-J. and Zhao, X. 2023a. Exogenous interference and autofluorescence-free ratiometric aptasensor for detection of OTA based on dual-colored persistent luminescence nanoparticles. *Food Chemistry*, 413: 135611-135617.

Guo, Y., Wang, W., Lei, H., Wang, M. and Jiao, S. 2022b. Alternate Storage of Opposite Charges in Multisites for High-Energy-Density Al–MOF Batteries. *Advanced Materials*, 34 (13): 1-11.

Guo, Y., Ye, H., Wang, H., Wang, Q., Fan, S. and Dou, H. 2023b. Asymmetrical flow field-flow fractionation combined with ultrafiltration: A novel and high-efficiency approach for

separation, purification, and characterization of Ganoderma lucidum polysaccharides. *Talanta*, 253: 124053-124059.

Guo, Z., Gao, L., Yin, L., Arslan, M., El-Seedi, H. R. and Zou, X. 2023c. Novel mesoporous silica surface loaded gold nanocomposites SERS aptasensor for sensitive detection of zearalenone. *Food Chemistry*, 403: 134384-134393.

Gupta, V., Mohapatra, S., Mishra, H., Farooq, U., Kumar, K., Ansari, M. J., Aldawsari, M. F., Alalaiwe, A. S., Mirza, M. A. and Iqbal, Z. 2022. Nanotechnology in Cosmetics and Cosmeceuticals—A Review of Latest Advancements. *Gels*, 8 (3): 173-203.

Hachem, K., Ansari, M. J., Saleh, R. O., Kzar, H. H., Al-Gazally, M. E., Altimari, U. S., Hussein, S. A., Mohammed, H. T., Hammid, A. T. and Kianfar, E. 2022. Methods of Chemical Synthesis in the Synthesis of Nanomaterial and Nanoparticles by the Chemical Deposition Method: A Review. *BioNanoScience*, 12 (3): 1032-1057.

Hamad, G. M., Mehany, T., Simal-Gandara, J., Abou-Alella, S., Esua, O. J., Abdel-Wahhab, M. A. and Hafez, E. E. 2023. A review of recent innovative strategies for controlling mycotoxins in foods. *Food Control*, 144: 109350-109360.

Han, X., Huangfu, B., Xu, T., Xu, W., Asakiya, C., Huang, K. and He, X. 2022. Research Progress of Safety of Zearalenone: A Review. *Toxins*, 14 (6): 386-404.

Hao, W., Ge, Y., Qu, M., Wen, Y., Liang, H., Li, M., Chen, C. and Xu, L. 2022. A simple rapid portable immunoassay of trace zearalenone in feed ingredients and agricultural food. *Journal of Food Composition and Analysis*, 107: 104292-104299.

Harpaz, D., Bernstein, N., Namdar, D. and Eltzov, E. 2022. Portable biosensors for rapid on-site determination of cannabinoids in cannabis, a review. *Biotechnology Advances*, 61: 108031-108047.

Hasanzadeh, M., Zargami, A., Baghban, H. N., Mokhtarzadeh, A., Shadjou, N. and Mahboob, S. 2018. Aptamer-based assay for monitoring genetic disorder phenylketonuria (PKU). *International Journal of Biological Macromolecules*, 116: 735-743.

Hattori, Y., Matsuda, W. and Seki, S. 2022. Solid-solid transition of microcrystalline oligo(phenylene ethynylene)s: Impact of crystalline structure on optoelectronic properties. *Chemical Physics Letters*, 801: 139709-139712.

He, B. and Yan, X. 2020. Ultrasensitive electrochemical aptasensor based on $CoSe_2$/AuNRs and 3D structured DNA-PtNi@Co-MOF networks for the detection of zearalenone. *Sensors and Actuators B: Chemical*, 306: 127558-127565.

He, H., Sun, D.-W., Pu, H. and Huang, L. 2020. Bridging Fe_3O_4@Au nanoflowers and Au@Ag nanospheres with aptamer for ultrasensitive SERS detection of aflatoxin B1. *Food Chemistry*, 324: 126832-126842.

He, H., Sun, D.-W., Pu, H. and Wu, Z. 2023. A SERS-Fluorescence dual-signal aptasensor for sensitive and robust determination of AFB1 in nut samples based on Apt-Cy5 and MNP@Ag-PEI. *Talanta*, 253: 123962-123972.

Hloma, P., Uwaya, G. E. and Bisetty, K. 2022. Smart electrochemical immunosensor for detection of aspartame in dietary products supported by in silico methods. *Biosensors and Bioelectronics: X*, 11: 100203-100212.

Honarparvar, B., Kanchi, S. and Bisetty, K. 2019. Theoretical insights into the competitive metal bioaffinity of lactoferrin as a metal ion carrier: a DFT study. *New Journal of Chemistry*, 43 (41): 16374-16384.

Hong, F., Huang, C., Wu, L., Wang, M., Chen, Y. and She, Y. 2021. Highly sensitive magnetic relaxation sensing method for aflatoxin B1 detection based on Au NP-assisted triple self-assembly cascade signal amplification. *Biosensors and Bioelectronics*, 192: 113489-113496.

Hou, Y., Long, N., Xu, Q., Li, Y., Song, P., Yang, M., Wang, J., Zhou, L., Sheng, P. and Kong, W. 2023. Development of a Nafion-MWCNTs and in-situ generated Au nanopopcorns dual-amplification electrochemical aptasensor for ultrasensitive detection of OTA. *Food Chemistry*, 403: 134375-134383.

Hu, X., Xia, Y., Liu, Y., Chen, Y. and Zeng, B. 2022. An effective ratiometric electrochemical sensor for highly selective and reproducible detection of ochratoxin A: Use of magnetic field improved molecularly imprinted polymer. *Sensors and Actuators B: Chemical*, 359: 131582-131589.

Hu, X., Zeng, Z., Zhang, J., Wu, D., Li, H. and Geng, F. 2023. Molecular dynamics simulation of the interaction of food proteins with small molecules. *Food Chemistry*, 405: 134824-134835.

Hua, Q., Liu, Z., Wang, J., Liang, Z., Zhou, Z., Shen, X., Lei, H. and Li, X. 2022. Magnetic immunochromatographic assay with smartphone-based readout device for the on-site detection of zearalenone in cereals. *Food Control*, 134: 108760-108770.

Huang, L. C., Zheng, N., Zheng, B. Q., Wen, F., Cheng, J. B., Han, R. W., Xu, X. M., Li, S. L. and Wang, J. Q. 2014. Simultaneous determination of aflatoxin M1, ochratoxin A, zearalenone and α-zearalenol in milk by UHPLC–MS/MS. *Food Chemistry*, 146: 242-249.

Huang, T., Wang, M., Hong, N., Cui, H., Fan, Q., Wei, G., Qin, L., Zhang, J. and Fan, H. 2023. An autonomous driven DNA walker-based electrochemical aptasensor for on-site detection of Ochratoxin A. *Talanta*, 252: 123785-123791.

Huang, X., Zhu, Y. and Kianfar, E. 2021. Nano Biosensors: Properties, applications and electrochemical techniques. *Journal of Materials Research and Technology*, 12: 1649-1672.

Hussain, G. and Silvester, D. S. 2018. Comparison of Voltammetric Techniques for Ammonia Sensing in Ionic Liquids. *Electroanalysis*, 30 (1): 75-83.

Iftikhar, T., Aziz, A., Ashraf, G., Xu, Y., Li, G., Zhang, T., Asif, M., Xiao, F. and Liu, H. 2022. Engineering MOFs derived metal oxide nanohybrids: Towards electrochemical sensing of catechol in tea samples. *Food Chemistry*, 395: 133642-133650.

İnada, A. A., Arman, S. and Safaei, B. 2022. A novel review on the efficiency of nanomaterials for solar energy storage systems. *Journal of Energy Storage*, 55: 105661-105685.

Indiarto, R., Indriana, L. P. A., Andoyo, R., Subroto, E. and Nurhadi, B. 2022. Bottom–up nanoparticle synthesis: a review of techniques, polyphenol-based core materials, and their properties. *European Food Research and Technology*, 248 (1): 1-24.

Inkson, B. J. 2016. 2 - Scanning electron microscopy (SEM) and transmission electron microscopy (TEM) for materials characterization. In: Hübschen, G., Altpeter, I., Tschuncky, R. and Herrmann, H.-G. eds. *Materials Characterization Using Nondestructive Evaluation (NDE) Methods*. Woodhead Publishing, 17-43. Available: https://www.sciencedirect.com/science/article/pii/B978008100040300002X (Accessed 30/10/2023).

Ismail, A. A., van de Voort, F. R. and Sedman, J. 1997. Chapter 4 Fourier transform infrared spectroscopy: Principles and applications. In: Paré, J. R. J. and Bélanger, J. M. R. eds. *Techniques and Instrumentation in Analytical Chemistry*. Elsevier, 93-139. Available: https://www.sciencedirect.com/science/article/pii/S0167924497800133 (Accessed 30/10/2023).

ISO. 2017. *Nanotechnologies — Size distribution and concentration of inorganic nanoparticles in aqueous media via single particle inductively coupled plasma mass spectrometry (ISO/TS 19590)*. Available: https://www.iso.org/standard/65419.html (Accessed 12/10/2023).

ISO. 2018. *Nanotechnologies — Analysis of nano-objects using asymmetrical-flow and centrifugal field-flow fractionation (ISO/TS 21362)*. Available: https://www.iso.org/standard/70761.html (Accessed 12/10/2023).

Jafarzadeh, S., Hadidi, M., Forough, M., Nafchi, A. M. and Mousavi Khaneghah, A. 2023. The control of fungi and mycotoxins by food active packaging: a review. *Critical Reviews in Food Science and Nutrition*, 63 (23): 6393-6411.

Jahangiri–Dehaghani, F., Zare, H. R. and Shekari, Z. 2022. A Non-label Electrochemical Aptasensor Based on Cu Metal–Organic Framework to Measure Aflatoxin B1 in Wheat Flour. *Food Analytical Methods*, 15 (1): 192-202.

Jahangiri–Dehaghani, F., Zare, H. R. and Shekari, Z. 2023. Simultaneous measurement of ochratoxin A and aflatoxin B1 using a duplexed-electrochemical aptasensor based on carbon nanodots decorated with gold nanoparticles and two redox probes hemin@HKUST-1 and ferrocene@HKUST-1. *Talanta*, 266: 124947-124954.

Jia, Y., Zhou, G., Wang, X., Zhang, Y., Li, Z., Liu, P., Yu, B. and Zhang, J. 2020. A metal-organic framework/aptamer system as a fluorescent biosensor for determination of aflatoxin B1 in food samples. *Talanta*, 219: 121342-121349.

Jiang, K., Nie, D., Huang, Q., Fan, K., Tang, Z., Wu, Y. and Han, Z. 2019. Thin-layer MoS_2 and thionin composite-based electrochemical sensing platform for rapid and sensitive detection of zearalenone in human biofluids. *Biosensors and Bioelectronics*, 130: 322-329.

Jiang, Y.-Y., Zhao, X., Chen, L.-J., Yang, C., Yin, X.-B. and Yan, X.-P. 2021. A dual-colored persistent luminescence nanosensor for simultaneous and autofluorescence-free determination of aflatoxin B1 and zearalenone. *Talanta*, 232: 122395-122401.

Kajal, N., Singh, V., Gupta, R. and Gautam, S. 2022. Metal organic frameworks for electrochemical sensor applications: A review. *Environmental Research*, 204: 112320-112338.

Kanchi, S., Sabela, I. M., Shahbaaz, M. and Bisetty, K. 2021. Sensitivity Enhancement of Pre-Capillary Chelation Method for the Separation of Metal Ions: Experimental and DFT Study. *Current Analytical Chemistry*, 17 (6): 839-848.

Kant, T., Shrivas, K., Dewangan, K., Kumar, A., Jaiswal, N. K., Deb, M. K. and Pervez, S. 2022. Design and development of conductive nanomaterials for electrochemical sensors: a modern approach. *Materials Today Chemistry*, 24: 100769-100784.

Karachaliou, C.-E., Koukouvinos, G., Pissaridi, K., Ladikos, D., Goustouridis, D., Raptis, I., Livaniou, E., Kakabakos, S. and Petrou, P. 2022. Fast and Accurate Determination of Minute Ochratoxin A Levels in Cereal Flours: Towards Application at the Field. *Engineering Proceedings*, 16 (1): 14-18.

Karadurmus, L., Corman, M. E., Uzun, L. and Ozkan, S. A. 2022. Enantioselective recognition of esomeprazole with a molecularly imprinted sol–gel-based electrochemical sensor. *Microchimica Acta*, 189 (6): 225-233.

Karimi-Maleh, H., Beitollahi, H., Senthil Kumar, P., Tajik, S., Mohammadzadeh Jahani, P., Karimi, F., Karaman, C., Vasseghian, Y., Baghayeri, M., Rouhi, J., Show, P. L., Rajendran, S., Fu, L. and Zare, N. 2022. Recent advances in carbon nanomaterials-based electrochemical sensors for food azo dyes detection. *Food and Chemical Toxicology*, 164: 112961-112973.

Kashyap, B. and Kumar, R. 2022. A novel multi-set differential pulse voltammetry technique for improving precision in electrochemical sensing. *Biosensors and Bioelectronics*, 216: 114628-114634.

Kaya, S. I., Ozcelikay, G., Mollarasouli, F., Bakirhan, N. K. and Ozkan, S. A. 2022. Recent achievements and challenges on nanomaterial based electrochemical biosensors for the detection of colon and lung cancer biomarkers. *Sensors and Actuators B: Chemical*, 351: 130856-130872.

Khan, H., Yerramilli, A. S., D'Oliveira, A., Alford, T. L., Boffito, D. C. and Patience, G. S. 2020. Experimental methods in chemical engineering: X-ray diffraction spectroscopy—XRD. *The Canadian Journal of Chemical Engineering*, 98 (6): 1255-1266.

Khataee, A., Sohrabi, H., Arbabzadeh, O., Khaaki, P. and Majidi, M. R. 2021. Frontiers in conventional and nanomaterials based electrochemical sensing and biosensing approaches for Ochratoxin A analysis in foodstuffs: A review. *Food and Chemical Toxicology*, 149: 112030-112054.

Khoi, C.-S., Chen, J.-H., Lin, T.-Y., Chiang, C.-K. and Hung, K.-Y. 2021. Ochratoxin A-Induced Nephrotoxicity: Up-to-Date Evidence. *International Journal of Molecular Sciences*, 22 (20): 11237-11256.

Khosrowshahi, M. S., Abdol, M. A., Mashhadimoslem, H., Khakpour, E., Emrooz, H. B. M., Sadeghzadeh, S. and Ghaemi, A. 2022. The role of surface chemistry on CO_2 adsorption in biomass-derived porous carbons by experimental results and molecular dynamics simulations. *Scientific Reports*, 12 (1): 8917-8935.

Kissinger, P. T. and Heineman, W. R. 1983. Cyclic voltammetry. *Journal of Chemical Education*, 60 (9): 702-706.

Kobets, A. A., Iurchenkova, A. A., Asanov, I. P., Okotrub, A. V. and Fedorovskaya, E. O. 2019. Redox Processes in Reduced Graphite Oxide Decorated by Carboxyl Functional Groups. *Physica Status Solidi (b)*, 256 (9): 1-7.

Koch, M., Mauch, T. and Riedel, J. 2022. Development of a Hydrazine-Based Solid-Phase Extraction and Clean-Up Method for Highly Selective Quantification of Zearalenone in Edible Vegetable Oils by HPLC-FLD. *Toxins*, 14 (8): 549-560.

Kohn, W., Becke, A. D. and Parr, R. G. 1996. Density Functional Theory of Electronic Structure. *The Journal of Physical Chemistry*, 100 (31): 12974-12980.

Kononenko, G. P., Burkin, A. A., Georgiev, A. A. and Georgieva, M. L. 2022. Composition and Content of Mycotoxins in the White Sea Fucoids. *Oceanology*, 62 (6): 833-838.

Korgel, B. A., van Zanten, J. H. and Monbouquette, H. G. 1998. Vesicle Size Distributions Measured by Flow Field-Flow Fractionation Coupled with Multiangle Light Scattering. *Biophysical Journal*, 74 (6): 3264-3272.

Kumar, D., Singh, K., Verma, V. and Bhatti, H. S. 2016. Low-temperature hydrothermal synthesis and functionalization of multiwalled carbon nanotubes. *Indian Journal of Physics*, 90 (2): 139-148.

Kunene, K., Sayegh, S., Weber, M., Sabela, M., Voiry, D., Iatsunskyi, I., Coy, E., Kanchi, S., Bisetty, K. and Bechelany, M. 2023. Smart electrochemical immunosensing of aflatoxin B1 based on a palladium nanoparticle-boron nitride-coated carbon felt electrode for the wine industry. *Talanta*, 253: 124000-124009.

Kunene, K., Weber, M., Sabela, M., Voiry, D., Kanchi, S., Bisetty, K. and Bechelany, M. 2020. Highly-efficient electrochemical label-free immunosensor for the detection of ochratoxin A in coffee samples. *Sensors and Actuators B: Chemical*, 305: 127438-127446.

Lehtola, S. 2019. A review on non-relativistic, fully numerical electronic structure calculations on atoms and diatomic molecules. *International Journal of Quantum Chemistry*, 119 (19): 25968-25998.

Lephalala, M., Kanchi, S., Sabela, M. I. and Bisetty, K. 2020. Electrochemical Enzymatic Biosensing of Neotame Supported by Computational Methods. *Electroanalysis*, 32 (12): 2669-2680.

Li, C., Deng, C., Zhou, S., Zhao, Y., Wang, D., Wang, X., Gong, Y. Y. and Wu, Y. 2018a. High-throughput and sensitive determination of urinary zearalenone and metabolites by UPLC-

MS/MS and its application to a human exposure study. *Analytical and Bioanalytical Chemistry*, 410 (21): 5301-5312.

Li, D.-l., Zhang, X., Ma, Y., Deng, Y., Hu, R. and Yang, Y. 2018b. Preparation of an OTA aptasensor based on a metal–organic framework. *Analytical Methods*, 10 (26): 3273-3279.

Li, H., Yang, J., Han, R., Wang, Y., Han, X., Wang, S. and Pan, M. 2023. Magnetic-fluorescent immunosensing platform applying AuNPs heterogeneous MIL-53(Al) composite for efficient detection of zearalenone. *Food Chemistry*, 433: 137369-137378.

Li, L., Chen, L. and Chen, Z. 2022. High throughput sensing of multiple amino acids with differential pulse voltammetry measurement. *Analytical Biochemistry*, 647: 114684-114689.

Li, X., He, F., Wang, Z. and Xing, B. 2022. Roadmap of environmental health research on emerging contaminants: Inspiration from the studies on engineered nanomaterials. *Eco-Environment & Health*, 1 (3): 181-197.

Liao, Z., Guo, W., Ning, G., Wu, Y., Wang, Y. and Ning, G. 2023. A sensitive electrochemical aptasensor for zearalenone detection based on target-triggered branched hybridization chain reaction and exonuclease I–assisted recycling. *Analytical and Bioanalytical Chemistry*, 415 (20): 4911-4921.

Lin, X., Fang, Y., Wei, J., Jiao, T., Chen, Q., Chen, Q. and Chen, X. 2023a. Gd_2O_3:Eu^{3+} nanoparticle-based magnetic relaxation switch/fluorescence dual-mode immunoassays for aflatoxin B1 in grain. *Sensors and Actuators B: Chemical*, 396: 134564-134571.

Lin, X., Ge, R., Wei, J., Jiao, T., Chen, Q., Oyama, M., Chen, Q. and Chen, X. 2023b. Magnetic-encoded fluorescent nanospheres-based competitive immunoassay for near-simultaneous detection of four mycotoxins in wheat. *Food Chemistry*, 432: 137267-137276.

Liu, M., Zhang, J., Liu, S. and Li, B. 2022a. A label-free visual aptasensor for zearalenone detection based on target-responsive aptamer-cross-linked hydrogel and color change of gold nanoparticles. *Food Chemistry*, 389: 133078-133084.

Liu, N., Meng, F., Chen, L., Yang, L. and Liu, D. 2022b. Investigating the effects of MWCNT-HB on gas storage performance of CO_2 hydrate. *Fuel*, 316: 123289-123298.

Liu, R., Feng, Z.-Y., Li, D., Jin, B., Lan, Y. and Meng, L.-Y. 2022c. Recent trends in carbon-based microelectrodes as electrochemical sensors for neurotransmitter detection: A review. *TrAC Trends in Analytical Chemistry*, 148: 116541-116556.

Liu, R., Shi, R., Zou, W., Chen, W., Yin, X., Zhao, F. and Yang, Z. 2020a. Highly sensitive phage-magnetic-chemiluminescent enzyme immunoassay for determination of zearalenone. *Food Chemistry*, 325: 126905-126910.

Liu, S., Yu, B., Wang, S., Shen, Y. and Cong, H. 2020b. Preparation, surface functionalization and application of Fe_3O_4 magnetic nanoparticles. *Advances in Colloid and Interface Science*, 281: 102165-102194.

Liu, W.-C., Pushparaj, K., Meyyazhagan, A., Arumugam, V. A., Pappuswamy, M., Bhotla, H. K., Baskaran, R., Issara, U., Balasubramanian, B. and Mousavi Khaneghah, A. 2022d. Ochratoxin A as an alarming health threat for livestock and human: A review on molecular interactions, mechanism of toxicity, detection, detoxification, and dietary prophylaxis. *Toxicon*, 213: 59-75.

Lohrke, J., Briel, A. and Mäder, K. 2008. Characterization of superparamagnetic iron oxide nanoparticles by asymmetrical flow-field-flow-fractionation. *Nanomedicine*, 3 (4): 437-452.

Lv, M., Li, F., Du, Y., Guo, X., Zhang, P. and Liu, Y. 2023. Ratiometric electrochemical aptasensor for AFB1 detection in peanut and peanut products. *International Journal of Electrochemical Science*, 18 (2): 9-15.

Lv, S., Wu, X., Guan, J., Yan, Y., Ge, M. and Zhu, G. 2021. Quantification and Confirmation of Zearalenone Using a LC-MS/MS QTRAP System in Multiple Reaction Monitoring and Enhanced Product Ion Scan Modes. *Food Analytical Methods*, 14 (9): 1843-1851.

Lv, X., Xu, X., Miao, T., Zang, X., Geng, C., Li, Y., Cui, B. and Fang, Y. 2022. A ratiometric electrochemiluminescent/electrochemical strategy based on novel designed BPYHBF nanorod and Fc-MOF with tungsten for ultrasensitive AFB1 detection. *Sensors and Actuators B: Chemical*, 352: 131026-131036.

Macdonald, J. R. and Johnson, W. B. 2018. Fundamentals of Impedance Spectroscopy. In: *Impedance Spectroscopy*. 1-20. Available: https://onlinelibrary.wiley.com/doi/abs/10.1002/9781119381860.ch1 (Accessed 12/10/2023).

Maestro. 2021. Schrödinger Release 2021: Schrödinger, LLC, New York, NY, 2021 (computer software).

Magar, H. S., Hassan, R. Y. A. and Mulchandani, A. 2021. Electrochemical Impedance Spectroscopy (EIS): Principles, Construction, and Biosensing Applications. *Sensors*, 21 (19): 6578-6598.

Maggira, M., Sakaridis, I., Ioannidou, M. and Samouris, G. 2022. Comparative Evaluation of Three Commercial Elisa Kits Used for the Detection of Aflatoxins B1, B2, G1, and G2 in Feedstuffs and Comparison with an HPLC Method. *Veterinary Sciences*, 9 (3): 104-114.

Malir, F., Pickova, D., Toman, J., Grosse, Y. and Ostry, V. 2023. Hazard characterisation for significant mycotoxins in food. *Mycotoxin Research*, 39 (2): 81-93.

Mallakpour, S., Nikkhoo, E. and Hussain, C. M. 2022. Application of MOF materials as drug delivery systems for cancer therapy and dermal treatment. *Coordination Chemistry Reviews*, 451: 214262-214282.

Manh, T. D., Nguyen, V. T., Duyen, V. T., Nga, N. T. T., Man, N. Q., Thoa, P. T. H., Trinh, L. H. and Khieu, D. Q. 2023. Differential pulse voltammetry determination of acetaminophen and codeine in pharmaceutical formulations using a Mn/UiO-66 modified glassy carbon electrode. *Journal of Nanoparticle Research*, 25 (9): 185-199.

Marimuthu, M., Arumugam, S. S., Jiao, T., Sabarinathan, D., Li, H. and Chen, Q. 2022. Metal organic framework based sensors for the detection of food contaminants. *TrAC Trends in Analytical Chemistry*, 154: 116642-116666.

Marken, F., Neudeck, A. and Bond, A. M. 2010. Cyclic Voltammetry. In: Scholz, F., Bond, A. M., Compton, R. G., Fiedler, D. A., Inzelt, G., Kahlert, H., Komorsky-Lovrić, Š., Lohse, H., Lovrić, M., Marken, F., Neudeck, A., Retter, U., Scholz, F. and Stojek, Z. eds. *Electroanalytical Methods: Guide to Experiments and Applications*. Berlin, Heidelberg: Springer Berlin Heidelberg, 57-106. Available: https://doi.org/10.1007/978-3-642-02915-8_4 (Accessed 15/06/2023).

Mashtalyar, D. V., Nadaraia, K. V., Plekhova, N. G., Imshinetskiy, I. M., Piatkova, M. A., Pleshkova, A. I., Kislova, S. E., Sinebryukhov, S. L. and Gnedenkov, S. V. 2022. Antibacterial Ca/P-coatings formed on Mg alloy using plasma electrolytic oxidation and antibiotic impregnation. *Materials Letters*, 317: 132099-132103.

Mehmandoust, M., Pourhakkak, P., Hasannia, F., Özalp, Ö., Soylak, M. and Erk, N. 2022. A reusable and sensitive electrochemical sensor for determination of Allura red in the presence of Tartrazine based on functionalized nanodiamond@SiO_2@TiO_2; an electrochemical and molecular docking investigation. *Food and Chemical Toxicology*, 164: 113080-113089.

Meng, D., Gan, X. and Tian, T. 2022. An Electrochemical Sensing Method for Aflatoxin B1 Detection Based on Pt-coordinated Titanium-based Porphyrin MOF. *International Journal of Electrochemical Science*, 17 (2): 1-10.

Metropolis, N., Rosenbluth, A. W., Rosenbluth, M. N., Teller, A. H. and Teller, E. 1953. Equation of State Calculations by Fast Computing Machines. *The Journal of Chemical Physics*, 21 (6): 1087-1092.

Mize, C. J., Crosby, L. D., Isbill, S. B. and Roy, S. 2022. Insight into Subsurface Adsorption Derived from a Lattice-Gas Model and Monte Carlo Simulations. *The Journal of Physical Chemistry C*, 126 (11): 5343-5353.

Mo, X., Liu, X., Chen, J., Zhu, S., Xu, W., Tan, K., Wang, Q., Lin, Z. and Liu, W. 2022. Separation of lattice-incorporated Cr(vi) from calcium carbonate by converting microcrystals into nanocrystals via the carbonation pathway based on the density functional theory study of incorporation energy. *Environmental Science: Nano*, 9 (5): 1617-1626.

Modarresi, M., Harfbol, M. R., Eshraghi, A. and Ahmadi, F. 2022. Development of ternary H-point standard addition method for simultaneous analysis of curcuminoids by differential pulse voltammetry. *Food Research International*, 161: 111802-111809.

Mohamed Noor, M. H., Wong, S., Ngadi, N., Mohammed Inuwa, I. and Opotu, L. A. 2022. Assessing the effectiveness of magnetic nanoparticles coagulation/flocculation in water treatment: a systematic literature review. *International Journal of Environmental Science and Technology*, 19 (7): 6935-6956.

Mohammadpour, Z., Kamankesh, M., Shokrollahi Barough, M., Walsh, T., Ghorbanzadeh, S., Hamdi, D., Akbari, M., Zare, Y., Rhee, K. Y. and Seyfoori, A. 2023. A review on polymeric

nanocomposites for the electrochemical sensing of breast cancer biomarkers. *Microchemical Journal*, 195: 109528-109547.

Mohan, B., Kumari, R., Virender, Singh, G., Singh, K., Pombeiro, A. J. L., Yang, X. and Ren, P. 2023. Covalent organic frameworks (COFs) and metal–organic frameworks (MOFs) as electrochemical sensors for the efficient detection of pharmaceutical residues. *Environment International*, 175: 107928-107946.

Mokhtar, N. A. I. M., Zawawi, R. M., Khairul, W. M. and Yusof, N. A. 2022. Electrochemical and optical sensors made of composites of metal–organic frameworks and carbon-based materials. A review. *Environmental Chemistry Letters*, 20 (5): 3099-3131.

Montaño, M. D., Olesik, J. W., Barber, A. G., Challis, K. and Ranville, J. F. 2016. Single Particle ICP-MS: Advances toward routine analysis of nanomaterials. *Analytical and Bioanalytical Chemistry*, 408 (19): 5053-5074.

Moro, G., Barich, H., Driesen, K., Felipe Montiel, N., Neven, L., Domingues Mendonça, C., Thiruvottriyur Shanmugam, S., Daems, E. and De Wael, K. 2020. Unlocking the full power of electrochemical fingerprinting for on-site sensing applications. *Analytical and Bioanalytical Chemistry*, 412 (24): 5955-5968.

Morris, G. M., Goodsell, D. S., Halliday, R. S., Huey, R., Hart, W. E., Belew, R. K. and Olson, A. J. 1998. Automated docking using a Lamarckian genetic algorithm and an empirical binding free energy function. *Journal of Computational Chemistry*, 19 (14): 1639-1662.

Morris, G. M., Huey, R., Lindstrom, W., Sanner, M. F., Belew, R. K., Goodsell, D. S. and Olson, A. J. 2009. AutoDock4 and AutoDockTools4: Automated docking with selective receptor flexibility. *Journal of Computational Chemistry*, 30 (16): 2785-2791.

Mukhopadhyay, A., Joshi, N., Chattopadhyay, K. and De, G. 2012. A Facile Synthesis of PEG-Coated Magnetite (Fe_3O_4) Nanoparticles and Their Prevention of the Reduction of Cytochrome C. *ACS Applied Materials & Interfaces*, 4 (1): 142-149.

Murad, A., Liew, J. Y. C., Yaacob, M. H., Noor, I. M., Osman, N. H., Kamarudin, M. A., Tan, S. T., Lee, H. K., Talib, Z. A., Alresheedi, M. T. and Mahdi, M. A. 2022. Effect of nickel ion concentration on structural, optical and electrical properties towards Ni–H_3BTC-MOF formation for nonlinear saturable absorption phenomenon. *Journal of Physics and Chemistry of Solids*, 167: 110743-110750.

Na, T. W., Seo, H.-J., Jang, S.-N., Kim, H., Yun, H., Kim, H., Ahn, J., Cho, H., Hong, S.-H., Kim, H. J. and Lee, S. H. 2022. Multi-residue analytical method for detecting pesticides, veterinary drugs, and mycotoxins in feed using liquid- and gas chromatography coupled with mass spectrometry. *Journal of Chromatography A*, 1676: 463257-463265.

Naidoo, L., Kanchi, S., Drexel, R., Meier, F. and Bisetty, K. 2021. Measurement of TiO_2 Nanoscale Ingredients in Sunscreens by Multidetector AF4, TEM, and spICP-MS Supported by Computational Modeling. *ACS Applied Nano Materials*, 4 (5): 4665-4675.

Naidoo, L., Suvardhan, K., Sabela, M. I. and Bisetty, K. 2020. Multivariate optimization of field-flow fractionation of nanoscale synthetic amorphous silica in processed foods supported by computational modelling. *New Journal of Chemistry*, 44 (40): 17542-17551.

Nallusamy, S. and Sujatha, K. 2021. Experimental analysis of nanoparticles with cobalt oxide synthesized by coprecipitation method on electrochemical biosensor using FTIR and TEM. *Materials Today: Proceedings*, 37: 728-732.

Nawrocka, A., Durkalec, M., Michalski, M. and Posyniak, A. 2022. Simple and reliable determination of total arsenic and its species in seafood by ICP-MS and HPLC-ICP-MS. *Food Chemistry*, 379: 132045-132054.

Neuenfeldt, N. H., Silva, L. P., Pessoa, R. S. and O Rocha, L. 2023. Cold plasma technology for controlling toxigenic fungi and mycotoxins in food. *Current Opinion in Food Science*, 52: 101045-101053.

Niazi, S., Khan, I. M., Yue, L., Ye, H., Lai, B., Korma, S. A., Mohsin, A., Rehman, A., Zhang, Y. and Wang, Z. 2022. Nanomaterial-based optical and electrochemical aptasensors: A reinforced approach for selective recognition of zearalenone. *Food Control*, 142: 109252-109265.

Norizan, M. N., Moklis, M. H., Ngah Demon, S. Z., Halim, N. A., Samsuri, A., Mohamad, I. S., Knight, V. F. and Abdullah, N. 2020. Carbon nanotubes: functionalisation and their application in chemical sensors. *RSC Advances*, 10 (71): 43704-43732.

Odeh, F., Nsairat, H., Alshaer, W., Ismail, M. A., Esawi, E., Qaqish, B., Bawab, A. A. and Ismail, S. I. 2020. Aptamers Chemistry: Chemical Modifications and Conjugation Strategies. *Molecules*, 25 (1): 3-53.

Olesik, J. W. 1991. Elemental Analysis Using ICP-OES and ICP/MS. *Analytical Chemistry*, 63 (1): 12-21.

Öncü Kaya, E. M., Korkmaz, O. T., Yeniceli Uğur, D., Şener, E., Tunçel, A. N. and Tunçel, M. 2019. Determination of Ochratoxin-A in the brain microdialysates and plasma of awake, freely moving rats using ultra high performance liquid chromatography fluorescence detection method. *Journal of Chromatography B*, 1125: 121700-121708.

Ong, J. Y., Phang, S.-W., Goh, C. T., Pike, A. and Tan, L. L. 2023. Impedimetric Polyaniline-Based Aptasensor for Aflatoxin B1 Determination in Agricultural Products. *Foods*, 12 (8): 1698-1717.

Otero, F. and Magner, E. 2020. Biosensors—Recent Advances and Future Challenges in Electrode Materials. *Sensors*, 20 (12): 3561-3577.

Oufensou, S., Ul Hassan, Z., Balmas, V., Jaoua, S. and Migheli, Q. 2023. Perfume Guns: Potential of Yeast Volatile Organic Compounds in the Biological Control of Mycotoxin-Producing Fungi. *Toxins*, 15 (1): 45-66.

Pack, E., Stewart, J., Rhoads, M., Knight, J., De Vita, R., Clark-Deener, S. and Schmale, D. G. 2020. Quantification of zearalenone and α-zearalenol in swine liver and reproductive tissues using GC-MS. *Toxicon: X*, 8: 100058-100066.

Palakollu, V. N., Chen, D., Tang, J.-N., Wang, L. and Liu, C. 2022. Recent advancements in metal-organic frameworks composites based electrochemical (bio)sensors. *Microchimica Acta*, 189 (4): 161-190.

Pan, L.-M., Zhao, X., Wei, X., Chen, L.-J., Wang, C. and Yan, X.-P. 2022. Ratiometric Luminescence Aptasensor Based on Dual-Emissive Persistent Luminescent Nanoparticles for Autofluorescence- and Exogenous Interference-Free Determination of Trace Aflatoxin B1 in Food Samples. *Analytical Chemistry*, 94 (16): 6387-6393.

Pan, M., Yin, Z., Liu, K., Du, X., Liu, H. and Wang, S. 2019. Carbon-Based Nanomaterials in Sensors for Food Safety. *Nanomaterials*, 9 (9): 1330-1352.

Parker, K. A., Ribet, S., Kimmel, B. R., dos Reis, R., Mrksich, M. and Dravid, V. P. 2022. Scanning Transmission Electron Microscopy in a Scanning Electron Microscope for the High-Throughput Imaging of Biological Assemblies. *Biomacromolecules*, 23 (8): 3235-3242.

Patel, P., Alidokht, S. A., Sharifi, N., Roy, A., Harrington, K., Stoyanov, P., Chromik, R. R. and Moreau, C. 2022. Microstructural and Tribological Behavior of Thermal Spray CrMnFeCoNi High Entropy Alloy Coatings. *Journal of Thermal Spray Technology*, 31 (4): 1285-1301.

Pathak, A. K. and Dhakate, S. R. 2022. Carbon Nanomaterial-Carbon Fiber Hybrid Composite for Lightweight Structural Composites in the Aerospace Industry: Synthesis, Processing, and Properties. In: Mazlan, N., Sapuan, S. M. and Ilyas, R. A. eds. *Advanced Composites in Aerospace Engineering Applications*. Cham: Springer International Publishing, 445-470. Available: https://doi.org/10.1007/978-3-030-88192-4_23 (Accessed 11/11/2023).

Patil, S. S. and Rathod, V. K. 2022. Combined effect of enzyme co-immobilized magnetic nanoparticles (MNPs) and ultrasound for effective extraction and purification of curcuminoids from Curcuma longa. *Industrial Crops and Products*, 177: 114385-114396.

Paul, D. R., Sharma, R., Rao, V. S., Panchal, P., Gautam, S., Sharma, A. and Nehra, S. P. 2023. Mg/Li@GCN as highly active visible light responding 2D photocatalyst for wastewater remediation application. *Environmental Science and Pollution Research*, 30 (44): 98540-98547.

Peng, G., Li, X., Cui, F., Qiu, Q., Chen, X. and Huang, H. 2018. Aflatoxin B1 Electrochemical Aptasensor Based on Tetrahedral DNA Nanostructures Functionalized Three Dimensionally Ordered Macroporous MoS_2–AuNPs Film. *ACS Applied Materials & Interfaces*, 10 (21): 17551-17559.

Pezeshkpur, M., Tadayon, F. and Sohrabi, M. R. 2023. A Molecularly Imprinted Polymer Based on Fe_3O_4@Au Nanoparticles for Detection of Aflatoxin B1 in Food Samples. *ChemistrySelect*, 8 (15): 1-12.

Podzimek, S. 2011. Light Scattering. In: *Light Scattering, Size Exclusion Chromatography and Asymmetric Flow Field Flow Fractionation*. 37-98. Available: https://onlinelibrary.wiley.com/doi/abs/10.1002/9780470877975.ch2 (Accessed 20/11/2023).

Postnova. 2017. *NovaFFF AF2000: Software Manual* Landsberg, Germany: Postnova Analytics GmbH.

Pradhan, S. and Ananthanarayan, L. 2020. Standardization and validation of a high-performance thin-layer chromatography method for the quantification of aflatoxin B1 and its application in surveillance of contamination level in marketed food commodities from the Mumbai region. *JPC – Journal of Planar Chromatography – Modern TLC*, 33 (6): 617-630.

Qian, L., Durairaj, S., Prins, S. and Chen, A. 2021. Nanomaterial-based electrochemical sensors and biosensors for the detection of pharmaceutical compounds. *Biosensors and Bioelectronics*, 175: 112836-112857.

Qian, S., Chang, D., He, S. and Li, Y. 2022a. Aptamers from random sequence space: Accomplishments, gaps and future considerations. *Analytica Chimica Acta*, 1196: 339511-339534.

Qian, W., Song, T., Ye, M., Huang, X., Li, Y. and Hao, B. 2022b. FITC/PEG Functionalized Nanographene Oxide/Gold Nanocomposites Enable Efficient Response to Dopamine. *Advanced Materials Interfaces*, 9 (33): 2201611-2201618.

Qiao, X., Ma, X., Ma, X., Yue, T. and Sheng, Q. 2021. A label-free aptasensor for ochratoxin a detection with signal amplification strategies on ultrathin micron-sized 2D MOF sheets. *Sensors and Actuators B: Chemical*, 334: 129682-129691.

Qu, H., Smith, W. C., Feng, X., Wang, J., Pinto, J., Xu, X. and Faustino, P. J. 2023. Asymmetrical Flow Field Flow Fractionation for Molar Mass Characterization of Polyethylene Oxide in Abuse-Deterrent Formulations. *Journal of Chromatography A*, 1705: 464186-464193.

Qu, S., Yang, H., Ren, D., Kan, S., Zou, G., Li, D. and Li, M. 1999. Magnetite Nanoparticles Prepared by Precipitation from Partially Reduced Ferric Chloride Aqueous Solutions. *Journal of Colloid and Interface Science*, 215 (1): 190-192.

Rahim, A. M. A. and Mahmoud, E. M. M. 2022. A Novel Magnetic Polyethylene Glycol Nanocomposite based on Graphite Reinforcement Carbon Paste Electrode for Voltammetric Determination of Perindopril L-arginine. *Journal of Analytical Chemistry*, 77 (7): 914-925.

Rahimizadeh, K., Zahra, Q. u. a., Chen, S., Le, B. T., Ullah, I. and Veedu, R. N. 2023. Nanoparticles-assisted aptamer biosensing for the detection of environmental pathogens. *Environmental Research*, 238: 117123-117141.

Rahman, H. A., Rafi, M., Putra, B. R. and Wahyuni, W. T. 2023. Electrochemical Sensors Based on a Composite of Electrochemically Reduced Graphene Oxide and PEDOT:PSS for Hydrazine Detection. *ACS Omega*, 8 (3): 3258-3269.

Ramanavicius, S., Samukaite-Bubniene, U., Ratautaite, V., Bechelany, M. and Ramanavicius, A. 2022. Electrochemical molecularly imprinted polymer based sensors for pharmaceutical and biomedical applications (review). *Journal of Pharmaceutical and Biomedical Analysis*, 215: 114739-114750.

Ramkumar, R., Dhakal, G., Shim, J.-J. and Kim, W. K. 2022. Differential pulse voltammetric sensor for tetracycline using manganese tungstate nanowafers and functionalized carbon nanofiber modified electrode. *Korean Journal of Chemical Engineering*, 39 (8): 2192-2200.

Rao, M. S. and Olson, A. J. 1999. Modelling of Factor Xa-inhibitor complexes: a computational flexible docking approach. *Proteins: Structure, Function, and Bioinformatics*, 34 (2): 173-183.

Raposo, F. and Barceló, D. 2021. Assessment of goodness-of-fit for the main analytical calibration models: Guidelines and case studies. *TrAC Trends in Analytical Chemistry*, 143: 116373-116384.

Rappe, A. K., Casewit, C. J., Colwell, K. S., Goddard, W. A., III and Skiff, W. M. 1992. UFF, a full periodic table force field for molecular mechanics and molecular dynamics simulations. *Journal of the American Chemical Society*, 114 (25): 10024-10035.

Ratautaite, V., Brazys, E., Ramanaviciene, A. and Ramanavicius, A. 2022. Electrochemical sensors based on l-tryptophan molecularly imprinted polypyrrole and polyaniline. *Journal of Electroanalytical Chemistry*, 917: 116389-116398.

Rayappa, M. K., Viswanathan, P. A., Rattu, G. and Krishna, P. M. 2021. Nanomaterials Enabled and Bio/Chemical Analytical Sensors for Acrylamide Detection in Thermally Processed Foods: Advances and Outlook. *Journal of Agricultural and Food Chemistry*, 69 (16): 4578-4603.

Rezvani Jalal, N., Madrakian, T., Afkhami, A. and Ahmadi, M. 2022. Ni/Co Bimetallic Metal–Organic Frameworks on Nitrogen-Doped Graphene Oxide Nanoribbons for Electrochemical Sensing of Doxorubicin. *ACS Applied Nano Materials*, 5 (8): 11045-11058.

Rezvani Jalal, N., Madrakian, T., Afkhami, A. and Ghoorchian, A. 2020. In Situ Growth of Metal–Organic Framework HKUST-1 on Graphene Oxide Nanoribbons with High Electrochemical Sensing Performance in Imatinib Determination. *ACS Applied Materials & Interfaces*, 12 (4): 4859-4869.

Rogowska, A., Pomastowski, P., Szultka-Młyńska, M., Walczak-Skierska, J., Rafińska, K., Rafiński, Z. and Buszewski, B. 2022. Investigation of the mechanism of zearalenone metabolization in different systems: Electrochemical and theoretical approaches. *Toxicon*, 210: 19-24.

Roohi, H. and Pouryahya, T. 2023. TD-DFT study of the excited state intramolecular proton transfer (ESIPT) mechanism and photophysical properties in coumarin–benzothiazole derivatives: substitution and solvent effects. *Molecular Systems Design & Engineering*, 8 (5): 647-665.

Ruffolo, S. A., Barca, D., Alvarez de Buergo, M. and La Russa, M. F. 2023. ICP-MS – Fundamentals and Application to Forensic Science. In: Mercurio, M., Langella, A., Di Maggio, R. M. and Cappelletti, P. eds. *Mineralogical Analysis Applied to Forensics: A Guidance on Mineralogical Techniques and Their Application to the Forensic Field*. Cham: Springer International Publishing, 171-192. Available: https://doi.org/10.1007/978-3-031-08834-6_6 (Accessed 29/10/2023).

Sabbagh, B. A., Kumar, P. V., Chew, Y. L., Chin, J. H. and Akowuah, G. A. 2022. Determination of metformin in fixed-dose combination tablets by ATR-FTIR spectroscopy. *Chemical Data Collections*, 39: 100868-100874.

Saini, S. S. and Abdel-Rehim, M. 2020. Integrated extraction approach for trace analysis of aflatoxin B1 in domestic water tanks using HPLC. *SEPARATION SCIENCE PLUS*, 3 (5): 167-174.

Sajid, M. 2022. Nanomaterials: types, properties, recent advances, and toxicity concerns. *Current Opinion in Environmental Science & Health*, 25: 100319-100330.

Saleh, T. A. 2021. Protocols for synthesis of nanomaterials, polymers, and green materials as adsorbents for water treatment technologies. *Environmental Technology & Innovation*, 24: 101821-101838.

Salisu, B., Anua, S. M., Ishak, W. R. W. and Mazlan, N. 2021. Development and validation of quantitative thin layer chromatographic technique for determination of total aflatoxins in poultry feed and food grains without sample clean-up. *Journal of Advanced Veterinary and Animal Research*, 8 (4): 656-670.

Sarkar, T., Rawat, K., Bohidar, H. B. and Solanki, P. R. 2016. Electrochemical immunosensor based on PEG capped iron oxide nanoparticles. *Journal of Electroanalytical Chemistry*, 783: 208-216.

Sel, K., Demirci, S., Meydan, E., Yildiz, S., Ozturk, O. F., Al-Lohedan, H. and Sahiner, N. 2015. Benign Preparation of Metal–Organic Frameworks of Trimesic Acid and Cu, Co or Ni for Potential Sensor Applications. *Journal of Electronic Materials*, 44 (1): 136-143.

Sen, P., Suresh, K., Vinoth Kumar, R., Kumar, M. and Pugazhenthi, G. 2016. A simple solvent blending coupled sonication technique for synthesis of polystyrene (PS)/multi-walled carbon nanotube (MWCNT) nanocomposites: Effect of modified MWCNT content. *Journal of Science: Advanced Materials and Devices*, 1 (3): 311-323.

Senthil Kumar, P., Sreeja, B. S., Krishna Kumar, K. and Padmalaya, G. 2022. Static and dynamic analysis of sulfamethoxazole using GO/ZnO modified glassy carbon electrode by differential pulse voltammetry and amperometry techniques. *Chemosphere*, 302: 134926-134937.

Shahcheraghi, N., Golchin, H., Sadri, Z., Tabari, Y., Borhanifar, F. and Makani, S. 2022. Nano-biotechnology, an applicable approach for sustainable future. *3 Biotech*, 12 (3): 65-88.

Shakiba, S., Shariati, S., Wu, H., Astete, C. E., Cueto, R., Fini, E. H., Rodrigues, D. F., Sabliov, C. M. and Louie, S. M. 2022. Distinguishing nanoparticle drug release mechanisms by asymmetric flow field–flow fractionation. *Journal of Controlled Release*, 352: 485-496.

Shalali, F., Cheraghi, S. and Taher, M. A. 2022. A sensitive electrochemical sensor amplified with ionic liquid and N-CQD/Fe_3O_4 nanoparticles for detection of raloxifene in the presence of tamoxifen as two essentials anticancer drugs. *Materials Chemistry and Physics*, 278: 125658-125665.

Shang, C., Li, Y., Zhang, Q., Tang, S., Tang, X., Ren, H., Hu, P., Lu, S., Li, P. and Zhou, Y. 2022. Alkaline phosphatase-triggered dual-signal immunoassay for colorimetric and electrochemical detection of zearalenone in cornmeal. *Sensors and Actuators B: Chemical*, 358: 131525-131532.

Shinoda, Y., Takase, S. and Shimizu, Y. 2023. Electrochemical Sulfite-Ion Sensor Using Sm_2CuO_4-Based Layered Perovskite-Type Oxide Thick Film. *IEEJ Transactions on Electrical and Electronic Engineering*, 18 (2): 300-302.

Singh, J. and Mehta, A. 2020. Rapid and sensitive detection of mycotoxins by advanced and emerging analytical methods: A review. *Food Science & Nutrition*, 8 (5): 2183-2204.

Singhal, A. and Khan, R. 2023. Plastic antibodies integrated with graphene quantum dots for electrochemical sensing of bisphenol-A in real samples. *Materials Letters*, 350: 134880-134883.

Singhal, A., Sadique, M. A., Kumar, N., Yadav, S., Ranjan, P., Parihar, A., Khan, R. and Kaushik, A. K. 2022. Multifunctional carbon nanomaterials decorated molecularly imprinted hybrid polymers for efficient electrochemical antibiotics sensing. *Journal of Environmental Chemical Engineering*, 10 (3): 107703-107721.

Sivagami, M. and Asharani, I. V. 2022. Phyto-mediated Ni/NiO NPs and their catalytic applications-a short review. *Inorganic Chemistry Communications*, 145: 110054-110068.

Socas-Rodríguez, B., Herrera-Herrera, A. V., Asensio-Ramos, M. and Rodríguez-Delgado, M. Á. 2020. Recent Applications of Magnetic Nanoparticles in Food Analysis. *Processes*, 8 (9): 1140-1173.

Sohrabi, H., Majidi, M. R., Arbabzadeh, O., Khaaki, P., Pourmohammad, S., Khataee, A. and Orooji, Y. 2022a. Recent advances in the highly sensitive determination of zearalenone residues in water and environmental resources with electrochemical biosensors. *Environmental Research*, 204: 112082-112100.

Sohrabi, H., Salahshour Sani, P., Orooji, Y., Majidi, M. R., Yoon, Y. and Khataee, A. 2022b. MOF-based sensor platforms for rapid detection of pesticides to maintain food quality and safety. *Food and Chemical Toxicology*, 165: 113176-113192.

Sun, L., Yang, M., Guo, H., Zhang, T., Wu, N., Wang, M., Yang, F., Zhang, J. and Yang, W. 2022a. COOH-MWCNT connected COF and chemical activated CTF as a novel electrochemical sensing platform for simultaneous detection of acetaminophen and p-

aminophenol. *Colloids and Surfaces A: Physicochemical and Engineering Aspects*, 647: 129092-129100.

Sun, S., Liu, H., Hu, Y., Wang, Y., Zhao, M., Yuan, Y., Han, Y., Jing, Y., Cui, J., Ren, X., Chen, X. and Su, J. 2023a. Selection and identification of a novel ssDNA aptamer targeting human skeletal muscle. *Bioactive Materials*, 20: 166-178.

Sun, S., Wang, B., Qing, M., Tian, D., Jiang, L. and Zhu, L. 2023b. Electrochemical Dopamine Detection Using Electrochemically Reduced Graphene Oxide/Silver/Metal Organic Framework Composites. *ChemistrySelect*, 8 (17): 1-9.

Sun, Y., Lv, Y., Qi, S., Zhang, Y. and Wang, Z. 2022b. Sensitive colorimetric aptasensor based on stimuli-responsive metal-organic framework nano-container and trivalent DNAzyme for zearalenone determination in food samples. *Food Chemistry*, 371: 131145-131153.

Swiech, O., Majdecki, M. and Bilewicz, R. 2023. PEGylated Network Nanostructured by Gold Nanoparticles for Electrochemical Sensing of Aromatic Redox and Nonredox Analytes. *ACS Applied Polymer Materials*, 5 (1): 214-222.

Teixeira, T. R., Hoeltz, M., Einloft, T. C., Dottori, H. A., Manfroi, V. and Noll, I. B. 2011. Determination of ochratoxin A in wine from the southern region of Brazil by thin layer chromatography with a charge-coupled detector. *Food Additives & Contaminants: Part B*, 4 (4): 289-293.

Thomas, D., Rasheed, Z., Jagan, J. S. and Kumar, K. G. 2015. Study of kinetic parameters and development of a voltammetric sensor for the determination of butylated hydroxyanisole (BHA) in oil samples. *Journal of Food Science and Technology*, 52 (10): 6719-6726.

Tian, M., Feng, Y., He, X., Zhang, D., Wang, W. and Liu, D. 2022. Mycotoxins in livestock feed in China - Current status and future challenges. *Toxicon*, 214: 112-120.

Tong, X., Ga, L., Bi, L.-g. and Ai, J. 2023. Wearable Electrochemical Sensors Based on Nanomaterials for Healthcare Applications. *Electroanalysis*, 35 (2): 1-33.

Trott, O. and Olson, A. J. 2010. AutoDock Vina: Improving the speed and accuracy of docking with a new scoring function, efficient optimization, and multithreading. *Journal of Computational Chemistry*, 31 (2): 455-461.

Uğur, A., Gencer Imer, A. and Gülcan, M. 2022. Enhancement in the photovoltaic efficiency of dye-sensitized solar cell by doping TiO_2 with MIL-101 MOF structure. *Materials Science in Semiconductor Processing*, 150: 106951-106959.

Uwaya, G. E. and Bisetty, K. 2023. Integration of multiwalled carbon nanotubes with cobalt oxide for smart electrochemical sensing of epicatechin in foods. *Carbon Trends*, 10: 100240-100255.

Vallabani, N. V. S. and Singh, S. 2018. Recent advances and future prospects of iron oxide nanoparticles in biomedicine and diagnostics. *3 Biotech*, 8 (6): 279-301.

Ventouri, I. K., Chang, W., Meier, F., Drexel, R., Somsen, G. W., Schoenmakers, P. J., de Spiegeleer, B., Haselberg, R. and Astefanei, A. 2023. Characterizing Non-covalent Protein Complexes Using Asymmetrical Flow Field-Flow Fractionation On-Line Coupled to Native Mass Spectrometry. *Analytical Chemistry*, 95 (19): 7487-7494.

Verma, S., Kujur, S., Sharma, R. and Pathak, D. D. 2022. Cucurbit[6]uril-Supported Fe_3O_4 Magnetic Nanoparticles Catalyzed Green and Sustainable Synthesis of 2-Substituted Benzimidazoles via Acceptorless Dehydrogenative Coupling. *ACS Omega*, 7 (11): 9754-9764.

Vijitvarasan, P., Cheunkar, S. and Oaew, S. 2022. A point-of-use lateral flow aptasensor for naked-eye detection of aflatoxin B1. *Food Control*, 134: 108767-108774.

Voss, L., Hsiao, I. L., Ebisch, M., Vidmar, J., Dreiack, N., Böhmert, L., Stock, V., Braeuning, A., Loeschner, K., Laux, P., Thünemann, A. F., Lampen, A. and Sieg, H. 2020. The presence of iron oxide nanoparticles in the food pigment E172. *Food Chemistry*, 327: 127000-127008.

Vydrina, I., Malkov, A., Vashukova, K., Tyshkunova, I., Mayer, L., Faleva, A., Shestakov, S., Novozhilov, E. and Chukhchin, D. 2023. A new method for determination of lignocellulose crystallinity from XRD data using NMR calibration. *Carbohydrate Polymer Technologies and Applications*, 5: 100305-100314.

Wachholz Junior, D., Deroco, P. B. and Kubota, L. T. 2022. A copper-based metal-organic framework/reduced graphene oxide-modified electrode for electrochemical detection of paraquat. *Microchimica Acta*, 189 (8): 278-289.

Wahlund, K. G. and Giddings, J. C. 1987. Properties of an asymmetrical flow field-flow fractionation channel having one permeable wall. *Analytical Chemistry*, 59 (9): 1332-1339.

Wang, C., Zhang, H., Jiang, X. and Zhou, B. 2019. Electrochemical Determination of Aflatoxin B1 (AFB1) Using a Copper-Based Metal-Organic Framework (Cu-MOF) and Gold Nanoparticles (AuNPs) with Exonuclease III (Exo III) Assisted Recycling by Differential Pulse Voltammetry (DPV). *Analytical Letters*, 52 (16): 2439-2453.

Wang, C. and Zhao, Q. 2020. A reagentless electrochemical sensor for aflatoxin B1 with sensitive signal-on responses using aptamer with methylene blue label at specific internal thymine. *Biosensors and Bioelectronics*, 167: 112478-112483.

Wang, H., Chen, L., Li, M., She, Y., Zhu, C. and Yan, M. 2022a. An Alkyne-Mediated SERS Aptasensor for Anti-Interference Ochratoxin A Detection in Real Samples. *Foods*, 11 (21): 3407-3417.

Wang, H., Zhao, B., Ye, Y., Qi, X., Zhang, Y., Xia, X., Wang, X. and Zhou, N. 2022b. A fluorescence and surface-enhanced Raman scattering dual-mode aptasensor for rapid and sensitive detection of ochratoxin A. *Biosensors and Bioelectronics*, 207: 114164-114172.

Wang, L., Hua, X., Shi, J., Jing, N., Ji, T., Lv, B., Liu, L. and Chen, Y. 2022c. Ochratoxin A: Occurrence and recent advances in detoxification. *Toxicon*, 210: 11-18.

Wang, L., Huang, Q., Wu, J., Wu, W., Jiang, J., Yan, H., Huang, J., Sun, Y. and Deng, Y. 2022d. The metabolism and biotransformation of AFB1: Key enzymes and pathways. *Biochemical Pharmacology*, 199: 115005-115015.

Wang, L., Lin, H., Zhang, J. and Wang, J. 2022e. Phage long tail fiber protein-immobilized magnetic nanoparticles for rapid and ultrasensitive detection of Salmonella. *Talanta*, 248: 123627-123635.

Wang, M., Duan, M., Yu, F., Fu, X., Gu, M., Chi, K., Li, M., Xia, X., Hu, R., Yang, Y. and Meng, S. 2021. Development of Aflatoxin B1 Aptamer Sensor Based on Iron Porphyrin Organic Porous Material. *Food Analytical Methods*, 14 (3): 537-544.

Wang, M., Guo, H., Wu, N., Zhang, J., Zhang, T., Liu, B., Pan, Z., Peng, L. and Yang, W. 2022f. A novel triazine-based covalent organic framework combined with AuNPs and reduced graphene oxide as an electrochemical sensing platform for the simultaneous detection of uric acid, dopamine and ascorbic acid. *Colloids and Surfaces A: Physicochemical and Engineering Aspects*, 634: 127928-127938.

Wang, S., Niu, R., Yang, Y., Zhou, X., Luo, S., Zhang, C. and Wang, Y. 2020. Aptamer-functionalized chitosan magnetic nanoparticles as a novel adsorbent for selective extraction of ochratoxin A. *International Journal of Biological Macromolecules*, 153: 583-590.

Wang, Y., Liu, X., Ma, S., He, X., Guo, C., Liang, Z., Hu, Y., Wei, Y., Lian, X. and Huang, D. 2023a. Progress in cancer therapy with functionalized Fe_3O_4 nanomaterials. *Frontiers of Materials Science*, 17 (3): 230658-230671.

Wang, Y., Yu, F., Liu, Q., Wang, C., Zhu, G., Bai, L., Shi, S., Zhao, Y., Jiang, Z. and Zhang, W. 2023b. A novel and sensitive dual signaling ratiometric electrochemical aptasensor based on nanoporous gold for determination of Ochratoxin A. *Food Chemistry*, 432: 137192-137200.

Wang, Z., Liu, Y., Li, F., Dubovyk, V., Guo, M., Zhu, G., Ran, Q. and Zhao, H. 2022g. Electrochemical sensing platform based on graphitized and carboxylated multi-walled carbon nanotubes decorated with cerium oxide nanoparticles for sensitive detection of methyl parathion. *Journal of Materials Research and Technology*, 19: 3738-3748.

Wei, B., Xu, J., Pang, J., Huang, Z., Wu, J., Cai, Z., Yan, M. and Sun, C. 2022. Prediction of electrochemical impedance spectroscopy of high-entropy alloys corrosion by using gradient boosting decision tree. *Materials Today Communications*, 32: 104047-104052.

Wei, Q., Huang, C., Lu, P., Zhang, X. and Chen, Y. 2023. Combining magnetic MOFs as a highly adsorbent with homogeneous chemiluminescent immunosensor for rapid and ultrasensitive determination of Ochratoxin A. *Journal of Hazardous Materials*, 441: 129960-129972.

Wei, Y., Han, B., Hu, X., Lin, Y., Wang, X. and Deng, X. 2012. Synthesis of Fe_3O_4 Nanoparticles and their Magnetic Properties. *Procedia Engineering*, 27: 632-637.

Wilschefski, S. C. and Baxter, M. R. 2019. Inductively Coupled Plasma Mass Spectrometry: Introduction to Analytical Aspects. *The Clinical Biochemist Reviews*, 40 (3): 115-133.

Wu, R., Guo, J., Wang, M., Liu, H., Ding, L., Yang, R., Liu, L.-e. and Liu, Z. 2023. Fluorescent Sensor Based on Magnetic Separation and Strand Displacement Amplification for the Sensitive Detection of Ochratoxin A. *ACS Omega*, 8 (17): 15741-15750.

Wu, Z., Sun, D.-W., Pu, H., Wei, Q. and Lin, X. 2022. $Ti_3C_2T_x$ MXenes loaded with Au nanoparticle dimers as a surface-enhanced Raman scattering aptasensor for AFB1 detection. *Food Chemistry*, 372: 131293-131302.

Wyatt, P. J. 2014. Measurement of Special Nanoparticle Structures by Light Scattering. *Analytical Chemistry*, 86 (15): 7171-7183.

Xing, L., Cao, X., Dou, Z., Wang, S., Zhang, W., Sun, C. and Men, Z. 2022. Solvent polarizability modulated the electronic state of conjugated long-chain polyene molecules by DFT. *Journal of Molecular Liquids*, 356: 119047-119052.

Yadav, N., Yadav, S. S., Chhillar, A. K. and Rana, J. S. 2021. An overview of nanomaterial based biosensors for detection of Aflatoxin B1 toxicity in foods. *Food and Chemical Toxicology*, 152: 112201-112224.

Yan, H., He, B., Ren, W., Suo, Z., Xu, Y., Xie, L., Li, L., Yang, J. and Liu, R. 2022a. A label-free electrochemical immunosensing platform based on PEI-rGO/Pt@Au NRs for rapid and sensitive detection of zearalenone. *Bioelectrochemistry*, 143: 107955-107964.

Yan, H., He, B., Zhao, R., Ren, W., Suo, Z., Xu, Y., Zhang, Y., Bai, C., Yan, H. and Liu, R. 2022b. Electrochemical aptasensor based on Ce_3NbO_7/CeO_2@Au hollow nanospheres by using Nb.BbvCI-triggered and bipedal DNA walker amplification strategy for zearalenone detection. *Journal of Hazardous Materials*, 438: 129491-129503.

Yang, Y., Ren, M.-Y., Xu, X.-G., Han, Y., Zhao, X., Li, C.-H. and Zhao, Z.-L. 2022. Recent advances in simultaneous detection strategies for multi-mycotoxins in foods. *Critical Reviews in Food Science and Nutrition*: 1-29.

Yao, X., Yang, Q., Wang, Y., Bi, C., Du, H. and Wu, W. 2022. Dual-Enzyme-Based Signal-Amplified Aptasensor for Zearalenone Detection by Using CRISPR-Cas12a and Nt.AlwI. *Foods*, 11 (3): 487-499.

Yi, Z., Ren, Y., Li, Y., Chen, B., Li, Y., Long, F. and Zhu, A. 2023. Highly intensive and long-lasting chemiluminescence "Three-in-One" Hemin/Fe_3O_4@MoS_2 hybrid nanozyme powered lab-on-fiber device for Ochratoxin A immunoassay. *Sensors and Actuators B: Chemical*, 392: 134056-134064.

Yilmaz, M., Al-Musawi, T. J., Saloot, M. k., Khatibi, A. D., Baniasadi, M. and Balarak, D. 2022. Synthesis of activated carbon from Lemna minor plant and magnetized with iron (III) oxide magnetic nanoparticles and its application in removal of Ciprofloxacin. *Biomass Conversion and Biorefinery*: 1-14.

Yoshinari, T., Sugita-Konishi, Y., Sato, E., Takeuchi, H., Taniguchi, M., Fukumitsu, T., Shimoyama, A., Nakamura, A., Murayama, S., Owaki, S., Miyake, S. and Hara-Kudo, Y. 2023. Survey and risk assessment of aflatoxins and sterigmatocystin in Japanese staple food items

and the evaluation of an in-house ELISA technique for rapid screening. *Food Control*, 157: 110154-110160.

Zachman, M. J., Williams, A. N., Kourkoutis, L. F. and Cullen, D. A. 2023. Cryogenic FIB and (S)TEM for Energy Storage and Conversion Materials Research. *Microscopy and Microanalysis*, 29 (Supplement_1): 1705-1705.

Zeng, Y., Hu, C.-L., Xu, W.-J., Zeng, T.-W., Zhu, Z.-X., Chen, X.-X., Liu, D.-X., Chen, Y.-J., Zhang, Y.-B., Zhang, W.-X. and Chen, X.-M. 2022. An Exceptional Thermally Induced Four-State Nonlinear Optical Switch Arising from Stepwise Molecular Dynamic Changes in a New Hybrid Salt. *Angewandte Chemie International Edition*, 61 (2): 1-8.

Zhan, H., Yang, S., Li, C., Liu, R., Chen, W., Wang, X., Zhao, Y. and Xu, K. 2023. A highly sensitive competitive aptasensor for AFB1 detection based on an exonuclease-assisted target recycling amplification strategy. *Analytical Methods*, 15 (1): 70-78.

Zhang, J., Xu, X. and Qiang, Y. 2020. Ultrasensitive electrochemical aptasensor for ochratoxin A detection using AgPt bimetallic nanoparticles decorated iron-porphyrinic metal-organic framework for signal amplification. *Sensors and Actuators B: Chemical*, 312: 127964-127971.

Zhang, L., Song, X., Qi, Q. and Liu, W. 2022a. Interaction of DPPC liposomes with cholesterol and food protein during in vitro digestion using Dynamic Light Scattering and FTIR spectroscopy analysis. *Food Chemistry*, 375: 131893-131902.

Zhang, S. and Vrient, A. 2020. Chapter 8 - Rapid detection of plant viruses and viroids. In: Awasthi, L. P. ed. *Applied Plant Virology*. Academic Press, 101-109. Available: https://www.sciencedirect.com/science/article/pii/B9780128186541000086 (Accessed 21/11/2023).

Zhang, X., Kamali, M., Uleners, T., Symus, J., Zhang, S., Liu, Z., Costa, M. E. V., Appels, L., Cabooter, D. and Dewil, R. 2022b. UV/TiO_2/periodate system for the degradation of organic pollutants – Kinetics, mechanisms and toxicity study. *Chemical Engineering Journal*, 449: 137680-137695.

Zhang, X., Xu, J., Zhong, J., Zhong, L., Mai, Z., Sun, D. and Zhai, H. 2023. A novel fluorescence sensor for sensitive detection of zearalenone using a polyvinylpyrrolidone-modified Zr(IV)-based metal-organic framework. *Sensors and Actuators B: Chemical*, 395: 134516-134526.

Zhao, H., Ren, S., Wei, Z. and Lou, X. 2022a. Evanescent Wave Optical-Fiber Aptasensor for Rapid Detection of Zearalenone in Corn with Unprecedented Sensitivity. *Biosensors*, 12 (7): 438-450.

Zhao, P., Huang, L., Wang, H., Wang, C., Chen, J., Yang, P., Ni, M., Chen, C., Li, C., Xie, Y. and Fei, J. 2022b. An ultrasensitive high-performance baicalin sensor based on C_3N_4-SWCNTs/reduced graphene oxide/cyclodextrin metal-organic framework nanocomposite. *Sensors and Actuators B: Chemical*, 350: 130853-130865.

Zheng, Y.-h., Cheng, Y., Bao, F. and Wang, Y.-s. 2006. Synthesis and magnetic properties of Fe_3O_4 nanoparticles. *Materials Research Bulletin*, 41 (3): 525-529.

Zhou, J., Zhao, L., Huang, S., Liu, Q., Ao, X., Lei, Y., Ji, C. and Ma, Q. 2022. Zearalenone toxicosis on reproduction as estrogen receptor selective modulator and alleviation of zearalenone biodegradative agent in pregnant sows. *Journal of Animal Science and Biotechnology*, 13 (1): 36-46.

Zimm, B. H. 1948. Apparatus and Methods for Measurement and Interpretation of the Angular Variation of Light Scattering; Preliminary Results on Polystyrene Solutions. *The Journal of Chemical Physics*, 16 (12): 1099-1116.

APPENDICES

Appendix 1. Operating conditions of the spICP-MS system for Fe_3O_4 NP analysis.

Instrument settings		
ICP-MS sample inlet flow	0.32	mL min^{-1}
ICP-MS dwell time	50	µs
ICP-MS scan time	60	s
Profile	Standard	
RPq	0.50	
Properties of target particle		
Elemental composition of target particle	Fe_3O_4	
Mass fraction	72	%
Ionization efficiency	100	%
Particle density	5.20	g cm^{-3}
Calibration data		
Transport efficiency	4.19	

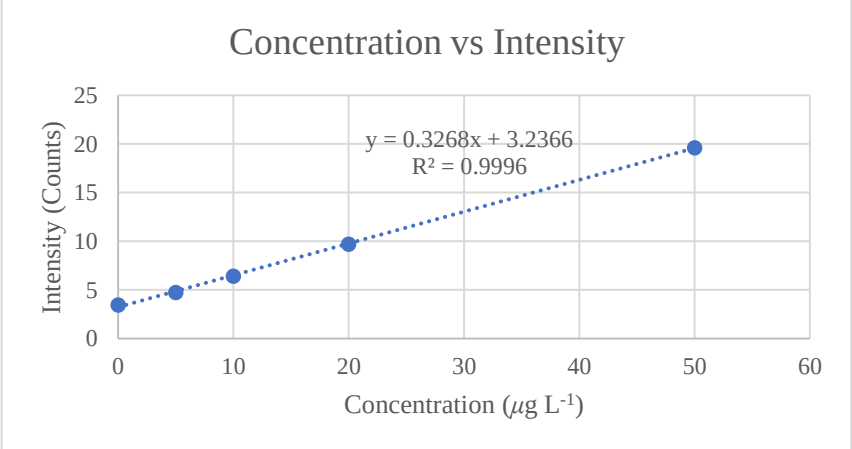

Appendix 2. Concentration vs intensity calibration plot using 5 μg L^{-1}, 10 μg L^{-1}, 20 μg L^{-1} and 50 μg L^{-1} Fe standards for spICP-MS.

Appendix 3. Binding affinities of various AFB1-aptamer interaction configurations. Structure 1 (**Appendix 4**) was selected for subsequent analysis.

Structure	Binding affinity (kcal mol^{-1})
1	-10.1
2	-10.0
3	-9.5
4	-9.3
5	-9.3
6	-9.2
7	-9.1
8	-9.1
9	-9.1

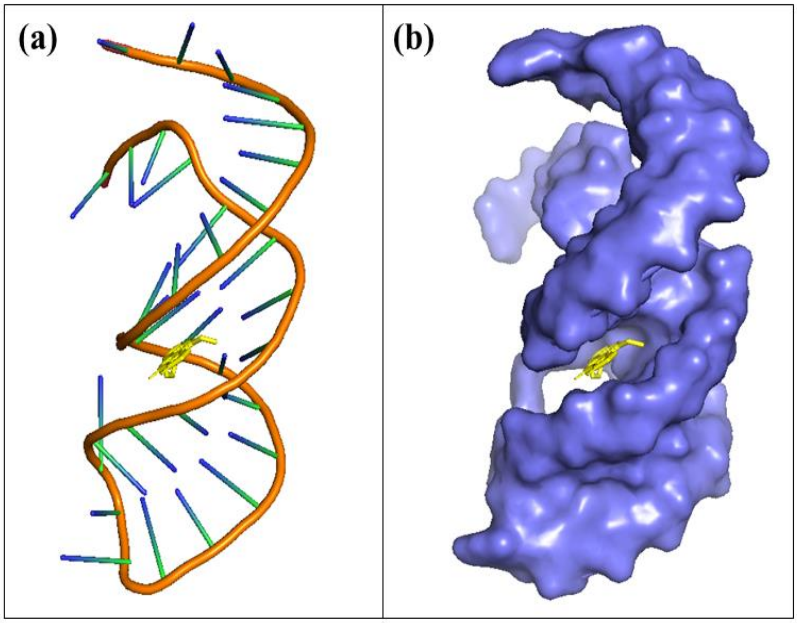

Appendix 4. (a) Selected molecular docking depiction of the AFB1-aptamer interaction (AFB1 in yellow) **(b)** 3D surface map of the simulation.

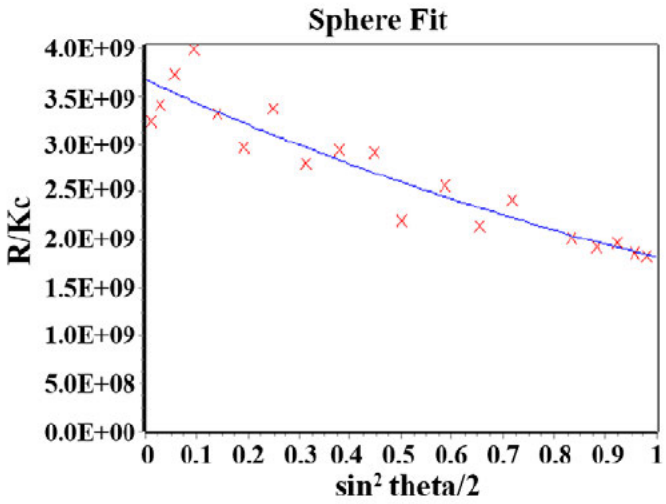

Appendix 5. Sphere fit factor plot for AF4-MALS fractogram of PEG-Fe_3O_4 NP suspension (MALS 12° to 164°).

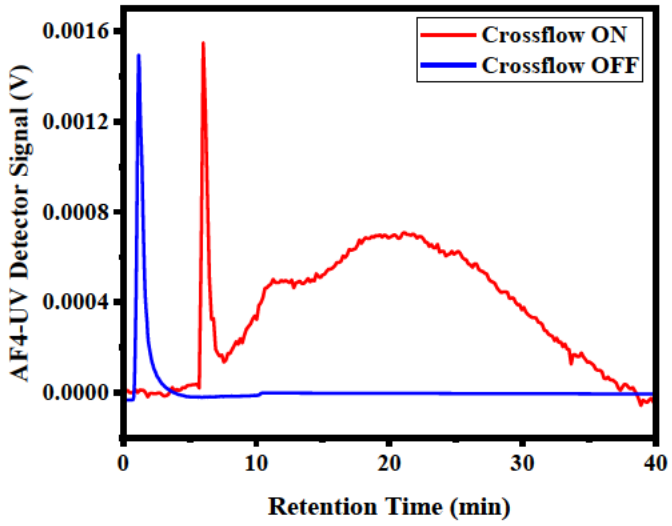

Appendix 6. AF4-UV fractogram of PEG-Fe_3O_4 NP suspension at λ = 405 nm in the presence (red line) and absence (blue line) of a crossflow field.